UNIVERSITY OF CINCINNATI

Date: <u>30 August, 2006</u>

I, Jeffery T. Stricker,

hereby submit this work as part of the requirements for the degree of:

Doctorate of Philosophy (Ph.D.)

in:

Physical Chemistry

It is entitled:

Organic Electronic Devices Using Crosslinked Polyelectrolyte

Multilayers as an Ultra-thin Dielectric Material

This work and its defense approved by:

Chair: Anna D. Gudmundsdóttir
   Tom L. Beck
   James E. Mark
   Michael F. Durstock

Organic Electronic Devices Using Crosslinked Polyelectrolyte Multilayers as an Ultra-thin Dielectric Material

By Jeffery T. Stricker

B.S. Materials Science
United States Air Force Academy (1996)

M.S. Materials Science and Engineering
University of Minnesota (1998)

Submitted to the Department of Chemistry
of the McMicken College of Arts and Sciences
in partial fulfillment of the requirements for the degree of

Doctor of Philosophy
in Physical Chemistry

at the

University of Cincinnati

September 2006

Committee Chair: Professor Anna D. Gudmundsdóttir

Report Documentation Page

1. REPORT DATE	2. REPORT TYPE	3. DATES COVERED
01 SEP 2006	**N/A**	**-**

4. TITLE AND SUBTITLE	5a. CONTRACT NUMBER
Organic Electronic Devices Using Crosslinked Polyelectrolyte Multilayers as an Ultra-thin Dielectric Material	5b. GRANT NUMBER
	5c. PROGRAM ELEMENT NUMBER
6. AUTHOR(S)	5d. PROJECT NUMBER
	5e. TASK NUMBER
	5f. WORK UNIT NUMBER

7. PERFORMING ORGANIZATION NAME(S) AND ADDRESS(ES)	8. PERFORMING ORGANIZATION REPORT NUMBER
University of Cincinnati	

9. SPONSORING/MONITORING AGENCY NAME(S) AND ADDRESS(ES)	10. SPONSOR/MONITOR'S ACRONYM(S)
	11. SPONSOR/MONITOR'S REPORT NUMBER(S)

12. DISTRIBUTION/AVAILABILITY STATEMENT
Approved for public release, distribution unlimited

13. SUPPLEMENTARY NOTES
The original document contains color images.

14. ABSTRACT

15. SUBJECT TERMS

16. SECURITY CLASSIFICATION OF:			17. LIMITATION OF ABSTRACT	18. NUMBER OF PAGES	19a. NAME OF RESPONSIBLE PERSON
a. REPORT	b. ABSTRACT	c. THIS PAGE	**UU**	**150**	
unclassified	**unclassified**	**unclassified**			

THIS PAGE INTENTIONALLY BLANK

ABSTRACT

The purpose of this study is to use the layer-by-layer assembly (LbL) method to investigate the incorporation of ultra-thin insulating films into organic electronic device architectures and to improve the understanding of structure-property relationships as applied to how nanoscale architecture affects device performance. Initially, reflective Fourier transform infrared (FT-IR) spectroscopy is used to quantify the degree of cross-linking in poly(allylamine hydrochloride)/poly(acrylic acid) (PAH/PAA) polyelectrolyte multilayers with a change in their intrinsic ionic interaction (solution pH) and an increase in post-deposition heat-treatment temperature. The breakdown strength of these dielectric films is then analyzed as a function of their degree of cross-linking, layer morphology, and film thickness to determine their applicability for use in metallized polymer film capacitors. Similar efforts are then directed toward the incorporation of these dielectric layers into both semi-conducting and doped organic thin film transistors (TFTs). While a field effect is observed when using a semi-conducting active layer, an electrochemical effect involving water is responsible for a change in the conductivity of the active layer in doped organic TFTs (PEDOT:PSS secondary doped with ethylene glycol). Similar observations are also apparent when using a standard (less conductive) active layer, whether it is deposited by spin-coating or with LbL assembly, but their response upon exposure to different environments is unique.

Acknowledgements

Table of Contents

Chapter 2: Quantitative Analysis of Amide Crosslinking in Heat Treated Polyelectrolyte Multilayer Films

Chapter 3: Breakdown Strength of Crosslinked Layer-by-Layer Assembled Films

List of Figures and Tables

Figure 5-3. Depletion rate (▲) and $I_{on/off}$ ratio (□) as a function of the number of PAH/PAA bilayers deposited as the gate dielectric at a pH of 6.5. Devices were tested at $V_{DS} = 0.1$ V under ambient conditions with the application of a 2.0 V gate bias.

Figure 5-4. a) $I_{DS} - V_{DS}$ characteristics (at $V_{DS} = 0.1$ V) of a device tested under a humidified N_2 environment with a gate dielectric layer comprised of 40 PAH/PAA bilayers deposited at a pH of 6 – 6.5 (thickness = 130 Å). b) $I_{DS} - V_G$ characteristics (at $V_{DS} = 0.1$ V) for this device tested under dry N_2 (♦), ambient (■), and humidified N_2 (▲) conditions.

Figure 5-5. Depletion rate (▲) and $I_{on/off}$ ratio (□) (measured at 3 – 5 seconds and 260 seconds after application of the gate bias, respectively) for a device tested under a range of relative humidities at a gate bias of 1.25 V and having a gate dielectric comprised of 10 PAH/PAA bilayers deposited at a pH of 6 – 6.5 (thickness = 30 Å).

Figure 5-6. Time-dependent performance characteristics (at $V_{DS} = 0.1$ V) of a TFT device with a gate dielectric comprised of 10 PAH/PAA bilayers deposited at a pH of 6 – 6.5 (thickness = 30 Å). Testing was initially done under humidified N_2 conditions and switched to ambient conditions after 45 minutes.

Figure 5-7. Absorption spectra obtained *in-situ* during operation of a device with an ITO gate electrode and a gate dielectric comprised of 40 PAH/PAA bilayers deposited at a pH of 6 – 6.5 (thickness = 130 Å). Spectra were obtained under humidified N_2 conditions before (thick grey line) and after (thick black line) a gate bias of 4.0 V was applied. During recovery, spectra (taken at 280 s intervals) were obtained first under humidified N_2 conditions (thin solid lines) and subsequently under ambient conditions (thin dashed lines).

Figure 6-1. Time-dependent performance characteristics (at $V_{DS} = 0.1$ V) under different test conditions of a TFT device with PEDOT:PSS as the active layer and 20 PAH/PAA bilayers as the gate dielectric (deposited at a pH of 6 – 6.5 with a total thickness ~ 60 Å).

Figure 6-2. Time-dependent performance characteristics (at $V_{DS} = 0.2$ V) of a TFT device with PEDOT:PSS as the active layer and 40 PAH/PAA bilayers as the gate dielectric layer (deposited at a pH of 6 – 6.5 with a total thickness ~ 130 Å). The device was tested under humidified N_2 conditions (RH ~ 75%).

Figure 6-3. Time-dependent performance characteristics (at $V_{DS} = 0.2$ V) of the same device described in Figure 2, but tested under humidified N_2 at 30% RH.

Figure 6-4. Time-dependent performance characteristics (at $V_{DS} = 0.2$ V) of a TFT device with PEDOT:PSS as the active layer and 40 PAH/PAA bilayers as the gate dielectric layer (deposited at a pH of 6 – 6.5 with a total thickness ~ 130 Å). The device was initially exposed to humidified N_2 (RH ~ 75%) and then purged with dry N_2 immediately before the gate bias was ramped up to 2.5 V. The labels A through C indicate the time at which the Raman spectra shown in Figure 5 were obtained.

Figure 6-5. Raman spectra obtained *in-situ* during operation for the device described in Figures 4 and 6. Labels A through P correspond to the times indicated in Figures 4 and 6.

Figure 6-6. Time-dependent performance characteristics of the same device discussed in Figure 4, but tested under humidified N_2 conditions. Labels D through P correspond to the time at which the Raman spectra shown in Figure 5 were obtained.

Chapter 1

Introduction and Background

1.1 General Introduction

The application of organic polymers in electronic devices such as light emitting diodes, capacitors, photovoltaics, and transistors has accelerated since the discovery that doping conjugated polymers induces electrical conductivity.[1] The electronic conductivity of these intrinsically conducting polymers can span many orders of magnitude from insulator to semiconductor and even to synthetic metal.[2,3,4] These conjugated polymers may not exceed the performance of conventional metallic or crystalline electronic devices in every application, but the unique properties of these macromolecules offer more design versatility. The incorporation of polymeric materials into electronic devices allows for the inclusion of flexibility, low density, high strength, and large scale deposition into the design of electronic devices at a low cost.

One method that can be used for the incorporation of polymeric materials into device architectures is the layer-by-layer (LbL) assembly of polyelectrolyte multilayers (PEMs). This deposition technique has received notable interest in research areas involving separation membranes,[5] microcapsules,[6] tribological behavior,[7] biomaterials,[8] and electroactive devices. LbL assembly usually entails sequential adsorption of oppositely charged monolayers of polyelectrolytes onto a substrate via electrostatics,[9] but has also been demonstrated using other interactions such has hydrogen bonding and stereocomplex formation. A thorough review of the progress in this field of study has been compiled by Decher and Schlenoff.[10] LbL assembly is an established method to deposit ultra-thin, pinhole-free polymer films uniformly onto large surfaces with varying topological features. This deposition technique also allows for design

control of multilayer architecture by varying the type and number of polyelectrolytes being deposited, the layer morphologies with different deposition conditions, and the total film thickness through the number of bilayers deposited.

The LbL method is used herein to investigate the applicability of these films as insulating layers in organic electronic devices and then to characterize the effect these films have on device performance. The insulating multilayer films were fabricated using the polyelectrolytes, poly(allylamine hydrochloride) and poly(acrylic acid) (PAH/PAA). A background of the layer-by-layer technique, as well as the properties of PAH/PAA multilayer films, will be discussed first. This discussion will provide a better understanding of the mechanism responsible for this technique and the factors that may influence the incorporation of these films into organic electronics. The background also extends into the electronic properties of polymers, such as conductive characteristics and breakdown strengths, and the current progresses made in the development of thin film capacitors and organic thin film transistors (OTFTs). The breakdown characteristics of these films will then be investigated as a function of cross-link density, thickness, and morphology. These films are then incorporated into different device architectures, of which the performance characteristics are obtained.

1.2 Layer-by-layer Assembly of Polyelectrolyte Multilayers

The development and understanding of organic electronic materials is currently finding applicability in the commercial sector and will continue to do so with further advances in low-cost processing techniques,[11] such as ink-jet printing[12] and soft-lithography.[13] The LbL electrostatic assembly technique is another deposition method that has gained significant attention due to its simplicity, design versatility, and applicability with other techniques. Like

other solution-based techniques, the process can be performed under ambient conditions and can be operated using common laboratory skills and equipment. Although initial efforts were demonstrated on numerous polyelectrolyte species,[14] efforts have also been successful with the incorporation of inorganic species, biological materials, multivalent ions, and nanoparticles.[15] The capability to incorporate these films into novel device architectures has also been demonstrated with their deposition into 2-dimensional patterns using stamping techniques, and their formation into 3-dimensional microspheres and nanotubes using templating techniques.[15]

1.2.1 Method of Fabrication

The layer-by-layer process commonly entails the alternating adsorption of oppositely charged polyelectrolytes onto a substrate using the dipping sequence outlined in Figure 1-1. A substrate is first dipped into either a dilute polycation solution or a dilute polyanion solution, depending on the substrate, and then dipped into its respective counterpart (either polyanion or polycation solution) with multiple rinse steps in de-ionized water after each step to remove any residual counterions and excess polymer. This sequence results in the formation of a bilayer on the substrate, which can be repeated for an unlimited number of cycles to deposit reproducible layers until a desired thickness is obtained. The LbL process has also been demonstrated using closed-cell flush,[16] spin-coating,[17] and spray[18] techniques, but will not be applied in this study.
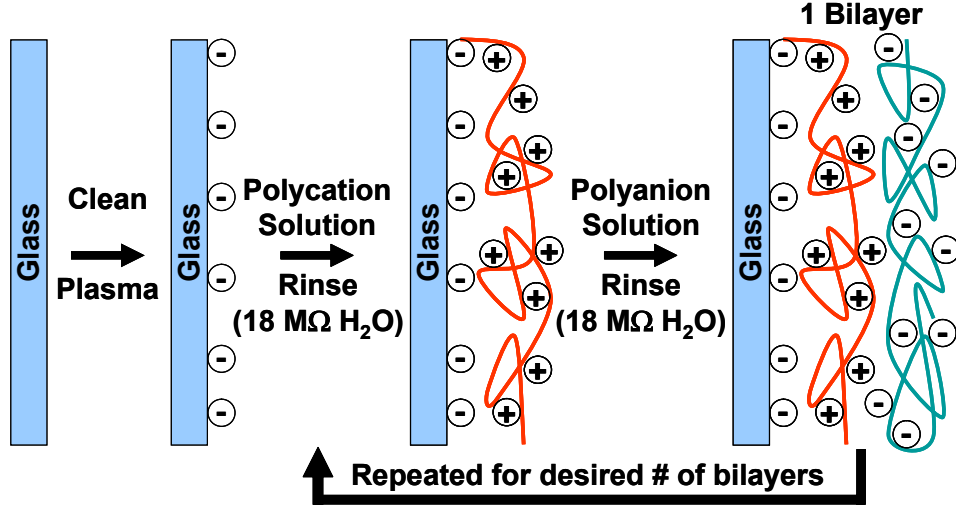
Figure 1-1. Schematic illustration of the layer-by-layer deposition process of polyelectrolyte multilayer films.

1.2.2 LbL Deposition Mechanism

The driving force for the deposition process of polyelectrolytes is electrostatic in nature and has been investigated thoroughly, both experimentally and theoretically. The irreversible deposition of a polyelectrolyte onto a substrate, regardless of its net surface charge,[19] and the charge reversal that occurs post-deposition,[20] have created an interest to increase the theoretical understanding of this deposition mechanism.

$$t = 2l_{cp}\left(\frac{\phi-1}{\phi}\right)(f^+ n_{odd} + f^- n_{even}) \qquad (1.1)$$

Recently, Schlenoff and Dubas presented the model in Equation 1.1 to describe the build-up (thickness) of these multilayers with intrinsic and extrinsic charge compensation when using strong polyelectrolytes.[21] This model describes the process with a charge compensation factor (ϕ) between the polyelectrolytes and a charge penetration length (l_{cp}) into the film from the solution interface. n_{odd} and n_{even} are the number of polycation and polyanion layers and f^+ and f^- account for the volume fraction of these segments. For continued growth of the multilayers, a ϕ > 1 is required for sequential deposition of oppositely charged species. The penetration length of

18

this charge overcompensation is a characteristic of the degree of extrinsic interactions ($\phi - 1$) with small counterions, and decreases exponentially into the film from the solution interface. These extrinsic interactions are then converted into irreversible intrinsic charge compensation interactions with oppositely charged polyelectrolytes upon exposure to the next adsorbing polymer.[17]

1.2.3 General Features of PEMs

1.2.3.1 Structural characteristics

Although the stepwise growth in thickness with an increase in the number of bilayers for these LbL assembled films would imply a discrete layered structure, the l_{cp} is significant enough that the internal structure of these materials are homogeneous. The interpenetration of the polyelectrolytes has been shown with neutron reflectometery and deuterium labeled polyanions to extend over several adjacent layers.[22] This degree of overlap depends upon the conformational stability of the polyelectrolyte[9] and its interactions with other species present in the deposition process, such as the solvent, buffer, substrate, or corresponding polyelectrolyte.[17]

While the bulk structure of these films is mainly homogeneous, the external interfacial regions deviate slightly from this characterization. Internally, the films consist primarily of stoichiometric polyionic interactions with a minimal concentration of small inorganic ions.[23,24,25] At the solution (or air) interface, the deposition of an additional polyelectrolyte monolayer induces a charge reversal at the surface that limits further polyelectrolyte deposition, and therefore causes the inclusion of small ions for extrinsic charge compensation. At the substrate interface, the growth characteristics are also observed to deviate from the bulk, dependent upon the substrate material. The bilayer thickness is often observed to increase with initial film

growth but quickly stabilizes after about 5 – 10 bilayers. This characteristic has been attributed to the initial charge density and surface roughness of the substrate.[26]

1.2.3.2 Factors influencing multilayer growth

The factors contributing to the layer-by-layer growth of PEMs are considered to be thermodynamically controlled since they do not appear to be kinetically hindered. Each sequential deposition of a polyelectrolyte monolayer has been shown in-situ, using a quartz crystal microbalance and with measurement of the zeta potential, to be completed on the timescale of a few minutes.[27] The resulting bilayer thickness is dependent on the interactions within the polyelectrolyte, and its interactions with the solvent, any salt present within the solution, and the exposed substrate surface. A solution with higher ionic strength, dependent upon the salt-type or its concentration, introduces a screening effect between these interactions, thereby altering their effects. The bilayer thickness has been shown to increase with higher ionic strength, both during deposition and with post-deposition exposure.[28] The film becomes unstable due to more favorable polymer-solution interactions and less favorable polymer-substrate or polymer-polymer interactions. This screening effect also reduces the repulsive electrostatic interactions within the adsorbing polyelectrolyte, thereby allowing a more random coil configuration with a higher degree of configurational entropy. At lower ionic strength or with significant surface binding interactions, the adsorption of the polymer will be more favorable due to a lower free energy of adsorption, but at the expense of the configurational entropy.

1.2.4 LbL Deposition of Weak Polyelectrolytes

The change in linear charge density of the polyelectrolyte components has a dramatic influence on the structure of the layers within PEMs. These characteristics have been studied thoroughly with the investigations of Rubner and co-workers on the LbL deposition of films using weak polyelectrolytes.[29,30,31,32] Their work demonstrated the ability to control the bilayer thickness of PAH/PAA multilayer films by deprotonating PAA with varying the pH from 2 to 6.5.[31] It was also shown that PAH induces a higher degree of ionization of PAA in PEM films than what occurs in pure solution cast films.[32] Sharp transitions were observed in the bilayer thickness as the pH of the dipping solutions was adjusted. Within a pH range of 2 to 4.5, the thickness of PAA decreases with an increase in pH due to an increased degree of ionization and therefore a higher degree of intra-segment repulsion. The PAH thickness contribution increases due to a higher degree of surface charge density from the pre-adsorbed PAA. An additional increase in pH then induces a sudden increase in bilayer thickness (~ 120 Å/bilayer) until another transition at a pH of 6 to extremely thin layers (~ 3-6 Å/bilayer). These characteristics are due to transformations from an entropy-driven random coil configuration to an enthalpy-driven extended polymer configuration as a high degree of stoichiometric interactions occurs between PAH and PAA. The transition back to thicker bilayers above a pH of 7 correlates with similar trends as the linear charge density of PAH decreases above a pH of 6.5.

$$f_B = \frac{10^{pK_B - pH}}{1 + 10^{pK_B - pH}} \qquad f_A = \frac{1}{1 + 10^{pK_A - pH}} \qquad (1.2)$$

$$F_{ad} = F_{conf} + F_{stick} + F_{rep} \qquad (1.3)$$

A theoretical model recently presented by Park *et al.* assumes a flat surface of variable charge between monolayers, and is used to describe the polymer morphology within these PEMs

as a function of pH.[30] The ionization fraction of each polyelectrolyte (f_A and f_B) is used to estimate the charge density of sites attaching the adsorbing polymer to the substrate surface (Equation 1.2). The charge density and the size of these anchored segments are then used to calculate the adsorption free energy for each monolayer. As shown in Equation 1.3, the free energy of adsorption (F_{ad}) accounts for the conformational entropy (F_{conf}) of the adsorbing polymer, the adsorption enthalpy of its interaction with the surface (F_{stick}), and its segment-segment repulsion (F_{rep}) with contributions from excluded volume and electrostatic effects. This cumulative model provides an accurate description of the initial exponential growth and its transition into a linear-type growth with an increasing number of bilayers. An iterative model was also applied with a representative bilayer from the linear part of the cumulative model to account for effects caused by a change in linear charge density (pH) and molecular weight of each polymer.

1.2.5 Heat-induced Crosslinking Within PEMs

The heat-treatment of select polyelectrolyte multilayer films has been demonstrated to induce the formation of covalent-type cross-links within their structure, which can improve the stability,[33] impermeability,[34] and resistivity[23] of these materials. This technique has been applicable in the micropatterning of polymer thin films,[35] in the fabrication of ion-selective membranes by templating with multivalent cations,[36] and in the formation of hollow microcapsules.[37] In particular, Harris *et al.* used IR techniques to show that amide linkages could be formed from the ionic interactions between PAH and PAA with heat-treatment (demonstrated in Figure 1-2).[33,38] The reflective IR spectra of a PAH/PAA multilayer, before and after heat-treatment, is shown in Figure 1-3. Before heat-treatment, the peaks due to the

COO$^-$ (1570 cm^{-1}) and COOH (1710 cm^{-1}) groups are present. Upon heat treatment, the conversion of the carboxylate groups to amide linkages is apparent with the absence of the carboxylate peak and the emergence of the amide I (C=O) peak (1670 cm^{-1}). The initial presence of the NH$_3^+$ peak and the introduction of the amide N-H peak after heat-treatment also indicate the formation of amide cross-links within these films.
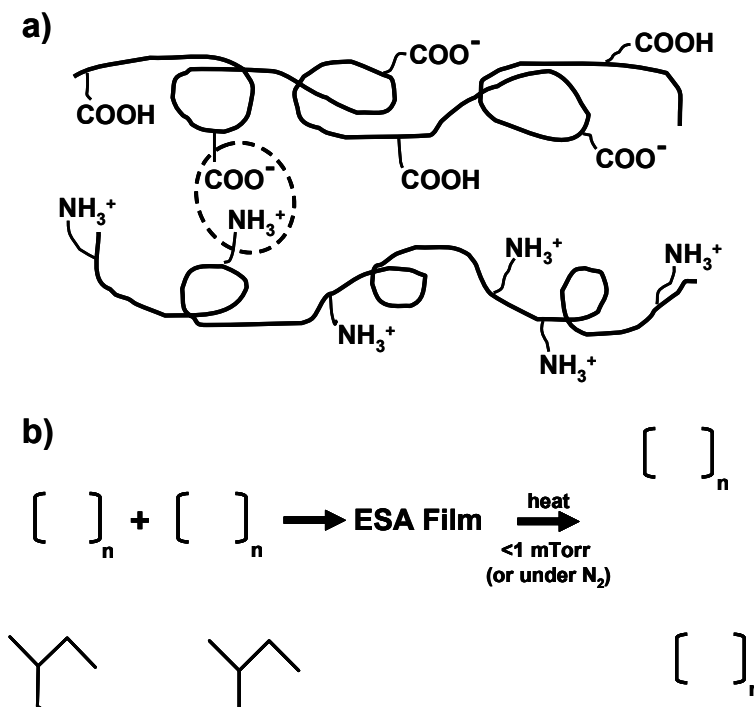
Figure 1-2. a) Illustration demonstrating the ionic interaction between PAH and PAA. b) Heat-induced cross-linking mechanism converting the ionic interaction into an amide covalent bond.
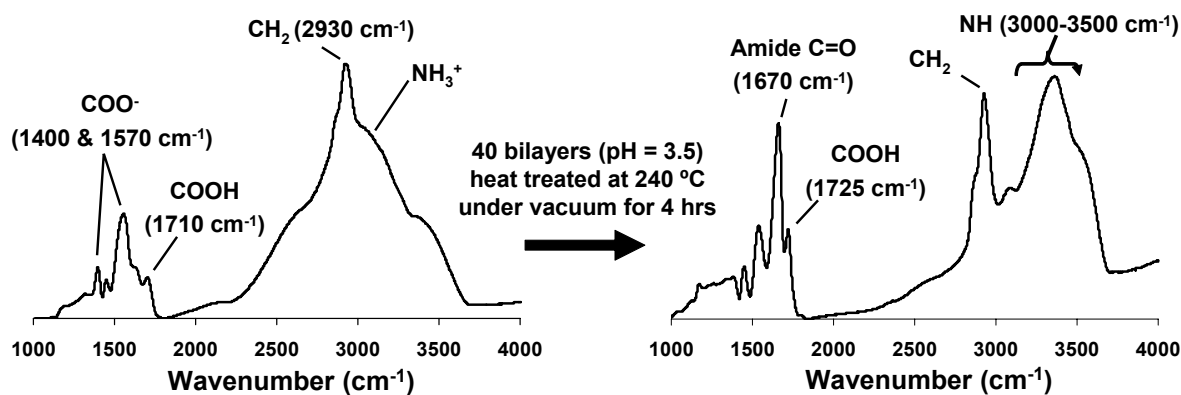
Figure 1-3. The reflective IR absorbance spectra, before and after heat-treatment, of 40 PAH/PAA bilayers deposited onto an aluminum substrate.

1.3 Electronic Properties of Polymeric Materials

Characterizing the electronic properties of polymers is a daunting task when considering the almost immeasurable conductance of highly insulating species at the low end of the spectrum (resistivity (ρ) ~ $10^{12} - 10^{17}$ Ω·cm)[39] and the strong structural dependence of charge carriers in doped conjugated materials (conductivity (σ) ~ 10^5 S/cm)[2] at the high end. The location of a polymer along this spectrum is determined by its conductivity, which is simply the inverse of resistivity. When a voltage (Volts, V) is applied across two points within the material, an electric field ($E = V/\Delta x$) is created in accordance to the difference in electrostatic potential between these two points (determined by the accumulation of charges at each point and their distance apart (Δx)). Typically at low electric fields, the rate of charge movement, described as current (I; amperes, A), increases linearly with voltage, as described with Ohm's law ($V = IR$). The resistance (R; ohms, Ω) measurement and the dimensions of the material (Δx, length; cm and A, area; cm^2) can then be used to determine the current density (J) and σ (and ρ) per Equation 1.4). The conductivity describes the ability (and ρ describes the inability) of charge to move through a material in response to an applied field and is dependent upon the total concentration of charge carriers (n; m^{-3}), the magnitude of charge (e; coulombs, C) for each carrier type, and their respective mobility (μ; m^2/V·s), which is the drift velocity of the carrier per applied field.

$$\frac{I}{A} = J = \frac{E \cdot \Delta x}{RA} = E\left(\frac{1}{\rho}\right) = \sigma E \quad where \ \sigma = \Sigma ne\mu \tag{1.4}$$

1.3.1 Energy Band Theory Applied to Polymers

Since atomic interactions are primarily electronic in nature, band theory is often applied to describe the type and number of charge carriers responsible for the conductive properties of

crystalline materials.[40]   The theory uses principles, derived from quantum mechanics, to demonstrate the splitting of atomic valence energy levels into bonding and antibonding molecular energy states as atoms approach one another. As an extended periodic network is formed, the electronic states become delocalized within energy bands defined by the resonance between the lattice periodicity and the wave-like properties of the charge carrier. The energy level diagram in Figure 1-4 demonstrates the filled band structure at temperature = 0 K, where the states are fully occupied in the valence band and completely unoccupied in the conduction band.   The energies between the bands define the band gap (E_g) since they are forbidden, which is often used to characterize materials either as conducting ($E_g \sim 0$ eV), semi-conducting (0.2 eV $< E_g < 2.0$ eV), or insulating ($E_g > 2.0$ eV). The Fermi level (E_F) found within the band gap is a thermodynamic parameter describing the chemical potential of the electrons and has a 50% probability of being occupied at a given temperature. Due to the small band gap of semi-conducting materials, their conductivity is temperature-dependent with the thermal excitation of electrons into the conduction band and the corresponding formation of vacancies (i.e. holes) in the conduction band.   This increase in concentration of free charge carriers at a given temperature can be determined by integrating the product of the density of states and the probability of occupancy over a defined energy range (Fermi-Dirac distribution).
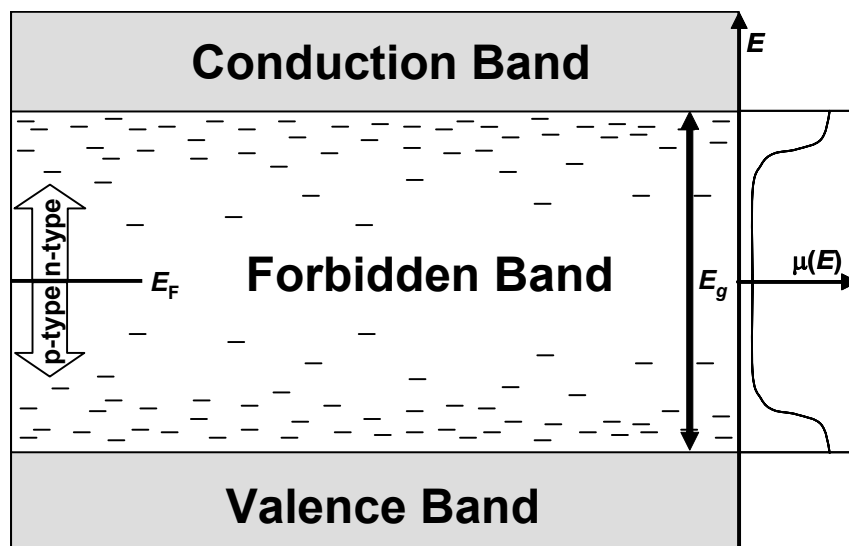
Figure 1-4. An energy band diagram illustrating the allowed energies for valence and conducting electrons. The dashes within the band gap (E_g) represent localized electron energy states, or traps, that are created by defects within the material. The high density of traps at the band gap edges result in a higher electron mobility. The Fermi level is in the middle of the forbidden band for a completely full valence band and empty conduction band, but shifts up and down with the respective introduction or subtraction of electrons.

The energy band theory can also be applied to polymeric materials to provide a qualitative understanding of the interactions along the backbone.[39,41] In theory, as a large group of $sp^2 p_z$ carbons (each with a free radical) come into close proximity to one another, they form a long 1-D macromolecule with a partially filled energy band. As a result, the free radicals are delocalized along the polymer chain, thus causing anisotropic conductance. In reality, a lower energy state is possible with a lattice transformation, commonly referred to as Peierl's distortion.[42] Conjugation of the backbone results from the π-electron hybridization with every other pair of carbons. This effect has been observed with the formation of alternating bond lengths along the backbone.[43] The localization of the π-electrons while forming the shorter double bonds results in a band gap between the valence and conduction band. These bands are commonly referred to as the highest occupied molecular orbital (HOMO) and lowest unoccupied molecular orbital (LUMO), respectively. The band gap for saturated hydrocarbons is much higher (~ 8 eV)[44] due to an even

larger degree of localization of the electrons around the carbons as only single bonds are formed through sp[3] hybridization.

The energy band level characteristics for polymers can then be used to describe their electronic properties. The small band gap (~ 1 - 2 eV) of conjugated materials explains why they often display semi-conducting trends such as thermally-enhanced conduction, photo-induced excitation, and the introduction of charge carriers into states within the band gap through doping. Although these materials have similarities with traditional inorganic semi-conducting materials, their conductive properties tend to be more structurally dependent. The $\pi \rightarrow \pi^*$ excitations for conjugated polymers are highly dependent upon changes in polymer configuration, which has a large effect on the charge carrier mobility.[45]

Contrasting conjugated polymers, saturated hydrocarbons are highly insulating since their large band gap makes it improbable for the creation of charge carriers through thermal excitation alone. Despite this improbability, leakage currents are observed and the conductivity increases at high electric fields.[46] These notable trends are commonly explained as being due to the formation of a mobility gap with localized energy states within the band gap, as shown in Figure 1-4.[47] A high concentration of localized states is present at both edges of the band gap due to traps caused by defects present within the material (i.e. impurities, "loops," "tails," or voids). The charge carrier mobility is then dependent upon the activation energy required to "hop" between these states or the degree of quantum tunneling, which is the tail-end probability of occurring in more than one state.

It should be noted that the characteristics described until now are mainly due to intra-segment interactions and that difficulties arise when accounting for the lower density and longer distance of interactions between polymer chains. Therefore, the charge carrier mobility within

these materials is highly dependent upon these external segment-segment interactions. This trend has been observed in conjugated materials, which will be discussed below with respect to organic TFTs.

1.3.2 Electrical Degradation and Breakdown of Insulating Polymers

Despite the long history of using synthetic polymers as insulating materials, an established understanding of their true dielectric strength continues to evade theoretical and experimental characterization. The source of this difficulty originates from factors such as their disordered structure, variations in testing conditions, and a myriad of possible breakdown mechanisms that may occur before the true intrinsic breakdown. Experimentally, a combination of these effects, and others, leads to a large statistical variation in breakdown measurements of polymers, even though they are tested repeatedly under identical conditions.[48] Gaining a theoretical understanding of these materials is also challenging due to the uncertainty in energy states within their mobility gaps and the transition from their ohmic behavior at low fields to their exponential increase in conductivity with voltages at high fields.[46] Several models involving either space charge limiting effects, hopping and tunneling mechanisms (between trap states at the edge of the mobility gap), or charge injections from either the electrode or donor/acceptor impurities have been presented to describe this phenomenon,[46] but both topics continue to be a source of debate.[49,50]

Von Hippel is often credited with initiating the development of electronic breakdown models with his description of electron-phonon interactions between the lattice and a single electron in the conduction band.[51] This model defines the highest obtainable electric field strength (E_c) without expansion of the free electron energy ($W = J \cdot E$) beyond what can be

28

dissipated by lattice vibrations. Since this model was more applicable to crystalline materials, Fröhlich expanded it to disordered (i.e. amorphous) materials by accounting for electron-electron interactions within both the conduction band and trap states.[52] This adapted model showed that the dielectric strength of amorphous polymers tended to decrease at higher temperatures because of excessive electron excitations into the conduction band.

Recently, Wu and Dissado presented a percolation model describing the intrinsic electrical breakdown as a function of the density and energy barrier of traps present within insulating polymers.[50] As shown in Equation 1.5, the field strength required to overcome the trap barrier was a function of the dielectric permittivity (ε), the bond orientation to the applied field ($\cos\theta$), and a percolation path through the material with a defined maximum trap barrier height (φ_c). Using typical trap depths for polymers (0.6 – 1.2 eV),[53] the application of this model predicted a breakdown strength of 2.1 MV/cm, which is typical for polymers. This model was also able to account for ageing effects, formation of percolation paths at weak points (cavities and high localized fields), and initial increases, then decreases, in dielectric strength with higher concentrations of additives or co-monomers.

$$E \cdot \cos\theta = \frac{\pi\varepsilon\varphi_c^2}{e^3} \qquad\qquad (1.5)$$

The models mentioned above provide a good understanding of the intrinsic properties that determine the maximum fields that can be obtained within polymers, but do not address the actual breakdown mechanism. There have been several reviews describing the possible mechanisms responsible for the physical damage that occurs when large surges in currents are obtained at high field strengths.[54] The mechanisms described include thermal runaway of the current with Joule heating, avalanche effects due to the cascading of impact ionization, an

electromechanical decrease in dielectric thickness with a high electrostatic attraction between the electrodes, and destructive discharge events caused by higher localized field strengths at voids, since they possess a lower dielectric constant. The discharge mechanism has been shown to depend upon the size of intrinsic holes present within the polymer, which if large enough, enable a sufficient free path for electron acceleration (free volume theory).[55] Additionally, limited studies have shown that the breakdown strength of polymers increases with chemical cross-link density[56] and a decrease in film thickness,[57] both of which are of interest in this study.

1.3.3 Intrinsically Conducting Polymers

The groundbreaking studies of MacDiarmid, Shirakawa, Heeger, and their co-workers on the intrinsic conductive properties of polymers have opened up a new dimension of design capabilities for fabricating electronic devices. Their work, as well as that of others, established the ability to modify the electronic properties of conjugated polymers by using molecular design to change the band gap or by using doping mechanisms to induce band gap states. Although chemical doping is capable of introducing charge carriers through redox or acid-base reactions, electrochemical doping is more applicable as it enables better control of the doping level.[58] This doping involves the introduction of either positive (p-type) or negative (n-type) charges along the backbone and are each delocalized over several repeat units and associated with a counterion. Other methods of doping have also been observed that are not associated with counterions. Such examples include the photoinduced formation of excitons, as observed in photovoltaics,[59] or the formation of charge carriers with a field effect, as will be discussed below with TFTs.

The band gap states formed upon charge injection into the conjugated polymers are dependent upon localization due to structural relaxation of the backbone.[45] The simplest case of

this charge carrier-lattice interaction is observed with the formation of a neutral conjugational

defect in polyacetylene, as demonstrated in Figure 1-5. This defect results in the formation of a

free radical on a carbon atom in the backbone and is delocalized over several repeat units

because of the conjugation resonance. This potential charge carrier is termed a soliton since it is

still partially conjugated. A single band gap state results from the soliton due to the degeneracy

of the identical resonance structures of the conjugated backbone. A soliton may also be induced

upon separation of a pair of electrons or with the addition or subtraction of an electron.
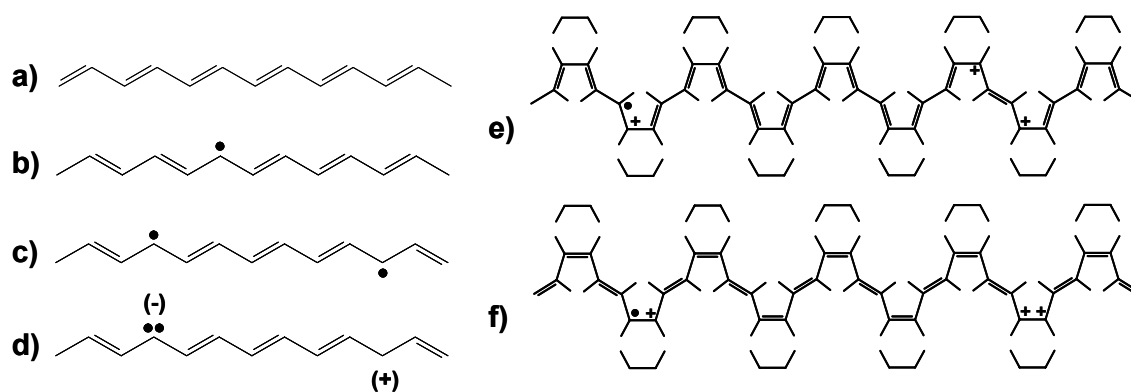
Figure 1-5. a) The bond conjugation for a pristine state of polyacetylene. b) The neutral conjugational defect in the polymer results in a soliton. c) A bond conjugation with a soliton and an anti-soliton that will cancel upon approaching each other. d) A negatively, and positively, charged soliton are present in the conjugated polymer upon addition, and removal, of an electron. e) The benzenoid bond configuration of PEDOT with a polaron (left) and bipolaron (right) charge carrier. f) The quinoid bond configuration of PEDOT with a polaron (left) and bipolaron (right) charge carrier. Although not shown in these figures, the charge carriers will be delocalized over several repeat units.

In the case of conjugated polymers with aromatic groups present in the backbone, two band

gap states are formed. This split in the mid-gap state is due to the non-degenerate relaxation

states of the quinoid and benzoid conjugation of the backbone.[41] The structure of poly(3,4-

ethylene dioxythiophene) (PEDOT), which is used in this study, is illustrated in Figure 1-5 with

both bond configurations. Doping of these compounds leads to the formation of polarons and

bipolarons, which are single and paired charge carriers in the backbone.[45] PEDOT is often

electrochemically synthesized in the presence of poly(styrene sulfonate) (PSS), which acts as a counterion to both stabilize the doped state and enable its dispersion into an aqueous solution. Spin-coated films of PEDOT:PSS are initially observed with a mixture of both bond configurations, but upon exposure to a compound with two or more polar groups experiences a secondary doping occurs.[60] Recently, it has been proposed that the compound enables PEDOT to transform into predominantly a quinoid bond configuration.[61] This bonding tendency induces an expanded coil polymer configuration that is more favorable for the formation of bipolarons due to a higher degree of delocalization.

A more thorough understanding of the electrochemical properties of PEDOT and its derivatives will improve the ability to tailor these materials for specific device applications. The stability of these highly conductive polymers (1-300 S/cm) is due to the electron-donating oxygen groups and resultant low oxidation potential of 0.2 V for the first electron transfer and 0.9 V for the second electron transfer.[62] The electrochemical doping of this material has also been described with a three-step redox process involving the formation of charge carries initially as polarons, then as bipolarons, and finally with a phase transformation to the metallic state.[63] Furthermore, the level of doping within PEDOT can be repetitively adjusted with redox chemistry due to the low middle potential ($E_{1/2} = 0.2$ V) of the anodic and cathodic potentials for this material.[63,64]

1.4 Electronic Applications of Polymers

1.4.1 Metallized Polymer Film Capacitors
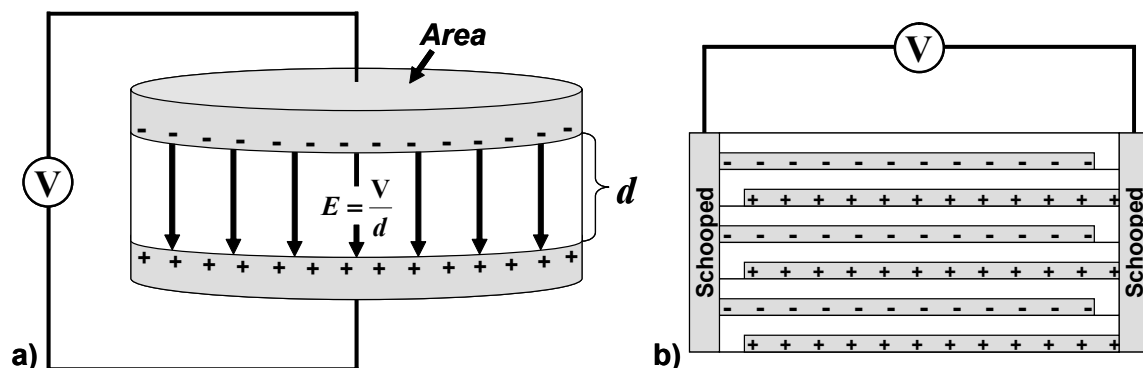
Figure 1-6. a) A schematic illustration of a simple parallel plate capacitor with an insulating layer separating two electrodes. b) The same concept is applied for a multilayered capacitor with the stacking of conducting and insulating layers. The schooped edges provide the means to make ohmic contacts to two different sets of alternating conducting layers.

The study of breakdown strength for polymers at the low end of the conductivity spectrum is directly applicable for high-voltage, pulsed-power capacitor applications. The concept of this application entails the storage of electrostatic energy by applying a high voltage between two electrodes that are separated by an insulating medium. The resulting field across the insulating medium leads to a capacitance effect with the accumulation of charge (Q) at both electrode interfaces, as illustrated in the schematic diagram of the device architecture in Figure 1-6a. The capacitance (*C*) of the device (Equation 1.6), in units of Farads (Coulomb/Volt), is a measure of this charge build-up and is dependent upon the interfacial area (*A*) of the electrodes, the permittivity of free space (ε_0), the thickness of the insulating region (*d*), and the dielectric constant of the material (ε), if present. The real part of the dielectric constant describes the polarizability of the material, which results in the screening of electrostatic interaction and enables a higher build-up of charge. Although a higher ε may increase the stored energy density, it results in a lower discharge rate of the capacitor and has been observed to increase the

dissipation factor (tan δ).[65] This factor is the ratio of the imaginary and real part of the dielectric constant, which describes the amount of energy dissipated relative to the amount stored with applied electric fields. Therefore, due to these limitations and the quadratic dependence of the stored electrostatic energy density on the applied voltage (Equation 1.7), research efforts are generally directed towards obtaining materials with higher breakdown strengths. The incorporation of an ultra-thin insulating layer into these capacitors is also of notable interest because a lower thickness (d), which results in an exponential increase in volumetric energy density (w).

$$C = \frac{Q}{V} = \frac{\varepsilon\varepsilon_0 A}{d} \qquad (1.6)$$

$$w = \frac{1}{2}\varepsilon\varepsilon_0 \left(\frac{V}{d}\right)^2 \qquad (1.7)$$

The fabrication of capacitors typically requires rolling them into cylinders for packaging reasons, but this architecture is not ideal due to induced interfacial stresses and low packing density.[66] As the techniques to deposit thin films mature, the alternating sequence of stacked conducting and insulating layers will likely prove to be a better method to obtain capacitors that are more reliable and have higher energy density capabilities. This multilayered architecture is illustrated in Figure 1-6b with metal schooped (sprayed) on the edges of the device to provide a contact between alternating electrode layers. Since each schooped edge provides a contact to a separate set of alternating electrodes, a parallel arrangement of the individual capacitors is achieved. Therefore, a lower dielectric thickness can be obtained by avoiding high interfacial stresses. When approaching an ultra-low thickness of the insulating layer (inorganic or polymeric), a self-healing clearing effect has been observed.[66,67] This effect is believed to be due

to defects such as voids, asperities, or impurities, but as of yet is not clearly understood. This effect will be discussed further in Chapter 3.

1.4.2 Organic Thin Film Transistors (OTFTs)

In 1986, a field effect in an OTFT was demonstrated for the first time using a conjugated polymer as the semi-conducting active layer.[68] Since that time, substantial progress has been achieved in the development and understanding of these organic devices, which has been addressed in several review articles.[69,70,71,72,73,74] The mobilities ($0.1 - 10$ m^2/V·s) of these conjugated materials are several orders of magnitude less than that of crystalline inorganic materials (i.e. Si, Ge). Therefore, the application of these slow devices will not be of interest in traditional uses, but their design capability, processablity, and flexibility may be beneficial for the development of low cost, large area electronics.[71] It has been stated that in order for these OTFTs to find applicability, a field effect mobility of 1 cm^2/V·s, an $I_{on/off}$ ratio of 10^6, and a maximum operative voltage of 15 V all need to be obtained under ambient conditions to match the speed, sensitivity, and portable applicability of amorphous silicon devices.[72]

1.4.2.1 Semiconducting active layer

The typical architecture of a TFT is demonstrated with the schematic illustration in Figure 1-7a. As shown, a thin insulating film separates the gate electrode and the semiconducting active layer. These layers act like a capacitor in that charge build-up occurs at the insulator interfaces when a voltage (V_G) is applied between the gate and source (ground) electrodes. This capacitance leads to an increased conductance for the first few monolayers of the active layer.[73] A p-type semi-conducting active layer (not related to doping) will experience a higher

conductance with the application of a negative gate bias as the Fermi level is lowered (Figure 1-5) to allow transfer of holes from the metal to states near the valence band. An n-type semi-conducting active layer will experience a higher conductance when a positive gate bias is used to raise the Fermi level (Figure 1-5), thereby enabling the transfer of electrons from the metal to the conduction band.

a)

b)
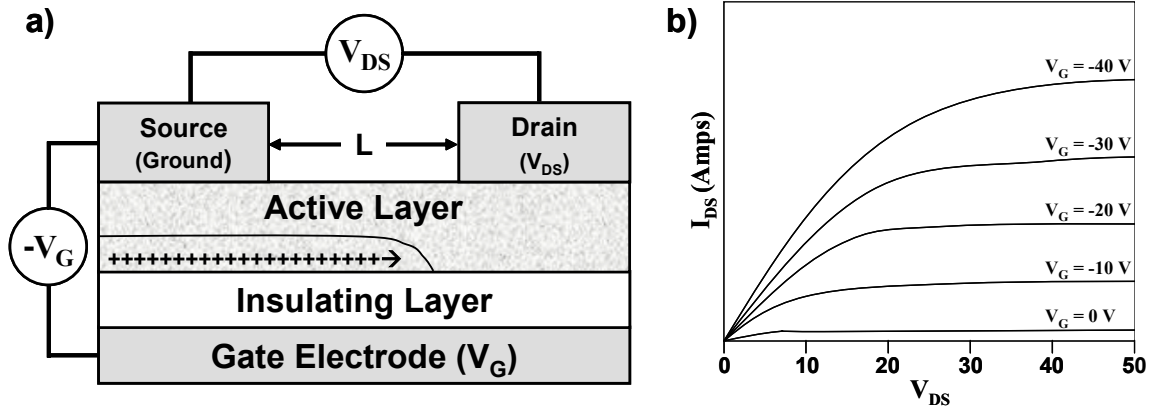
Figure 1-7. a) Schematic illustration of a p-type thin film transistor with the accumulation of charge carriers within the active layer. Upon application of a negative gate bias, a capacitive effect induces the formation of charge carriers at the interface with the insulating layer. b) The hypothetical output characteristics can be observed in the $I_{DS} - V_{DS}$ plot, which demonstrates the linear regime, as V_{DS} is initially increases for each applied gate bias, and the saturated regime where the conducting channel is pinched-off due to a high V_{DS}.

The current (I_{DS}) between the source and drain electrode is dependent on the density and mobility of the charge carriers in the active layer. An increase in the gate bias raises the conductivity of the active layer by inducing a higher charge carrier density at the semiconductor/insulator interface and also in effect improves the mobility as trap states are filled. The accumulation of charge carriers at the interface is dependent upon the magnitude of V_G and the capacitance (C_{ins}) of the dielectric layer, which is a function of its thickness (d) and dielectric constant. As shown with the output characteristics ($I_{DS} - V_{DS}$ plot) in Figure 1-7b, this field effect will in essence increase I_{DS} for an applied V_{DS}. As V_{DS} is increased past V_G, the I_{DS} saturates due to a lower potential drop and corresponding depletion of charge build-up near the

drain electrode. The slope of the linear regime for the transfer characteristics ($I_{DS} - V_G$ plot), obtained at $V_{DS} < V_G$, are often used with Equation 1.8 to calculate the field effect mobility for a semi-conducting channel with a certain width (W) and length (L). Within this regime, the mobility may be dependent on the gate bias due to the presence of trap states. To reduce this dependence, the slope of the $\sqrt{I_{DS}} - V_G$ plot for the saturated regime ($V_{DS} > V_G$) of the $I_{DS} - V_{DS}$ characteristics, is commonly used with Equation 1.9 to calculate the field effect mobility. The threshold voltage (V_T) is the offset at $I_{DS} = 0$ Amps and is related to the degree of trapping and level of doping present in the semiconducting active layer.[75,74]

$$\left.\frac{\partial \mathbf{I_{DS}}}{\partial \mathbf{V_G}}\right|_{V_{DS} \to 0} = \frac{WC_{ins}}{L}\mu_{lin}V_{DS} \qquad (1.8)$$

$$\mathbf{I_{DS}} = \frac{WC_{ins}}{2L}\mu_{sat}(V_G - V_T)^2 \qquad (1.9)$$

Significant progress has been achieved in improving the understanding and performance of these devices based on the semiconductor used in the active layer. The highest mobility values have been obtained using pentacene ($\mu = 6$ cm^2/V·s)[76] and regioregular poly(3-hexylthiophene) ($\mu = 0.2$ cm^2/V·s),[77] in regards to small molecules and polymers, respectively. A higher mobility has been shown to depend on the alignment of these materials into highly ordered, layered structures.[78] The aromatic groups align with an edge on perpendicular arrangement to the substrate, thereby enhancing close molecular packing with favorable $\pi - \pi$ overlap between the backbones. The mobility for these conjugated materials is dependent upon the disorder and doping level present in the active layer, which in effect influences its susceptibility to change with temperature and gate bias. As the disorder increases within these materials, the field effect mobility is highly dependent on temperature and gate bias. This dependence is thought to be due to an activation energy required to promote hopping of charge carriers between localized states

near the band edges.[79] On the contrary, the delocalized band transport is generally applied to account for the mobility of highly ordered materials. A combination of both has also been applied to account for the occasional observance of temperature-independence,[80] but the debate on this matter continues.

Recently, the role of the insulating layer in these devices has received significant attention due to its influence on operating performance. The objective is to lower the maximum operating voltage for portable applications while maintaining both a large $I_{on/off}$ ratio (I_{DS} at "on" and "off" state) and high mobility.   Since the operating voltage depends upon the capacitance of the dielectric, the logical choices are to decrease the thickness of the insulating layer or to increase its dielectric constant. The former option is limited by the formation of pinholes in thin spin-coated films or the use of self-assembled monolayers on select substrates.[81,82] The latter option does lower the operating voltage,[83] but the trap density at the interface also increases. The higher trap density is believed to be a result of higher structural and energy disorder caused by random dipoles at the interface.[84] A lower modulation, a higher degree of hysteresis, and a larger threshold voltage have been observed when using high-k insulating films as the dielectric layer.[85] Therefore, the ideal insulating layer needs to be thin and have a high internal dielectric constant, but have a low dielectric constant and smooth surface at the interface. The LbL method may enable incorporation of an ultra-thin insulating layer with this desired multilayered structure.

1.4.2.2 Doped-organic active layer

Recently, organic TFTs using highly doped conducting polymers, such as poly(3,4-ethylenedioxythiophene):poly(styrene sulfonate) (PEDOT:PSS), as the active layer have been observed to exhibit an unexpected field effect.[86] It was doubtful whether intrinsically conducting

38

organic materials could be applied in this manner because of screening from the large charge carrier density ($\sim 10^{20}$ cm^{-3}). Despite this concern, OTFTs have been successfully made using conducting polymers with the belief that the observed field effect is related to ion motion under the applied field.[87] However, the nature of how this phenomenon effects a change in conductivity is still under consideration. In short, application of a positive gate voltage (V_G) depletes the source-drain current (I_{DS}) and switches the device into the "off" state. While the observed response time of these devices is generally quite low (10-20 minutes with $V_G = 20$-40 V), $I_{on/off}$ ratios of about 10^4 have been achieved under ambient conditions.[88]

A field-induced metal-insulator transition has been suggested by Epstein[88] and co-workers for similar stacked TFTs architectures using PEDOT:PSS as the active layer. Only a limited number of charge carriers are believed to participate in conduction, thereby reducing the screening of the field effect. The active layer is believed to be near the insulator-metal transition in that the conduction is theorized to occur via hopping between "crystalline" regions within an amorphous medium. As a gate bias is applied, the hopping mechanism is then disrupted within the ordered region.

In addition, a variety of electrochemical transistors have been demonstrated using a lateral arrangement of PEDOT:PSS patterns encapsulated in a polyelectrolyte membrane.[89] These types of transistors are typically fabricated by submerging the active layer into an electrolyte solution so its doping level can be electrochemically modified with a gate bias.[90] The device operation mechanism for the stacked doped organic TFTs may also have an electrochemical effect.[91] Establishing the dependence of the device operation on the gate dielectric layer thickness may improve the understanding of the ion motion with an applied gate bias and help determine whether it is related to the electrochemical doping of the active layer.

39

1.5 References

1. Shirakawa, H.; Louis, E. J.; MacDiarmid, A. G.; Chiang, C. K.; Heeger, A. J. *Chem. Commun.* **1977**, *16*, 578.

2. MacDiarmid, A. G. *Synth. Met.* **2002**, *125*, 11.

3. Heeger, A. J. *Current Applied Physics* **2001**, *1*, 247

4. Shirakawa, H. *Reviews of Modern Physics* **2001**, *73*, 713.

5. Balachandra, A. M.; Dai, J.; Bruening, M. L. *Macromolecules* **2002**, *35*, 3171.

6. Schuetz, P.; Caruso, F. *Adv. Funct. Mater.* **2003**, *13*, 929.

7. Pavoor, P. V.; Gearing, B. P.; Bellare, A. ; Cohen, R. E. *Wear* **2004**, *256*, 1196.

8. Hua, A.; Jones, S. A.; Lvov, Y. M. *Cell Biochemistry and Biophysics* **2003**, 39, 23-44.

9. Decher, G. *Science* **1997**, *277*, 1232.

10. *Multilayer Thin Films*; Edited by Decher, G.; Schlenoff, J. B.; WILEY-VCH Verlag GmbH & Co.: Weinheim, 2003.

11. Forrest, S. R. *Nature*, **2004**, *428*, 911.

12. Hebner, T. R.; Wu, C. C.; Marcy, D.; Lu, M. H.; Sturm, J. C. *Appl. Phys. Lett*. **1998**, *72*, 519.

13. Xia, Y.; Whitesides, G. M. *Angew. Chem. Int. Ed*. **1998**, *37*, 550.

14. Knoll, W. *Current Opinion in Colloid and Interface Science* **1996**, *1*, 137.

15. Hammond, P. T. *Adv. Mater*. **2004**, *16*, 1271 and references therein.

16. Xie, A. F.; Granick, S. *Macromolecules* **2002**, *35*, 1805.

17. Dubas, S. T.; Schlenoff, J. B. *Macromolecules*, **1999**, *32*, 8153.

18. Schlenoff, J. B.; Dubas, S. T.; Farhat, T. *Langmuir* **2000**, *16*, 9968.

19. Andelman, D; Joanny, J. F. *Macromolecules* **1991**, *24*, 6040.

20. Decher, G.; Hong, J. D.; Schmitt, J. *Thin Solid Films* **1992**, *210-211*, 831.

21. Schlenoff, J. B.; Dubas, S. T. *Macromolecules* **2001**, *34*, 592.

22. a) Schmitt, J.; Gruenewald, T.; Decher, G.; Pershan, P. S.; Kjaer, K.; Loesche, M. *Macromolecules* **1993**, *26*, 7058. b) Korneev, D.; Lvov, Y.; Decher, G.; Schmitt, J.; Yaradaikin, S. *Physica B* **1995**, *213-214*, 954.

23. Durstock, M. F.; Rubner, M. F. *Langmuir* **2001**, *17*, 7865.

24. Korneev, D.; Lvov, Y.; Decher, G.; Scmitt, J.; Yaradaikin, S. *Physica B* **1995**, *213-214*, 954.

25. Schlenoff, J. B.; Ly, H.; Li, M. *J. Am. Chem. Soc.* **1998**, *120*, 7626.

26. Kurth, D. G.; Volmer, D.; Klitzing, R. V. in *Multilayer Thin Films*; Edited by Decher, G.; Schlenoff, J. B.; WILEY-VCH Verlag GmbH & Co.: Weinheim, 2003, Ch. 14.

27. Decher, G. in *Multilayer Thin Films*; Edited by Decher, G.; Schlenoff, J. B.; WILEY-VCH Verlag GmbH & Co.: Weinheim, 2003, pp 9 - 12.

28. Dubas, S. T.; Schlenoff, J. B. *Langmuir* **2001**, *17*, 7725.

29. Yoo, D.; Shiratori, S. S.; Rubner, M. F. Macromolecules 1998, 32, 4309.

30. Park, S. Y.; Barrett, C. J.; Rubner, M. F.; Mayes, A. M. Macromolecules 2001, 34, 3384.

31. Shiratori, S. S.; Rubner, M. F. *Macromolecules* **2000**, *33*, 4213.

32. Choi, J.; Rubner, M. F. *Macromolecules*, **2005**, *38*, 116.

33. Harris, J. J.; DeRose, P. M.; Bruening, M. L. *J. Am. Chem. Soc.* **1999**, *121*, 1978.

34. Dai, J.; Jensen, A. W.; Mohanty, D. K.; Erndt, J.; Bruening, M. L. *Langmuir* **2001**, *17*, 931.

35. Yang, S. Y.; Rubner, M. F. *J. Am. Chem. Soc.* **2002**, *124*, 2100.

36. Balachandra, A. M.; Dai, J.; Bruening, M. L. *Macromolecules* **2002**, *35*, 3171.

37. Schuetz, P.; Caruso, F. *Adv. Funct. Mater.* **2003**, *13*, 929.

38. Dai, J. D.; Sullivan, D. M.; Bruening, M. L. *Ind. Eng. Chem. Res.* **2000**, *39*, 3528.

39. Dissado, L. A.; Fothergill, J. C. *Electrical Degradation and Breakdown in Polymers*; Edited by Stevens, G. C.; Peter Peregrinus Ltd.: London, 1992, Ch. 2.

40. For a thorough review of the solid state band theory see Kittel, C. *Introduction to Solid State Physics 7th Ed.*; John Wiley & Sons, Inc.: New York, 1996.

41. For a short review, see Roth, S. *One-Dimensional Metals*; VCH Verlagsgesellschaft mbH.: Weinheim, 1995.

42. Peierls, R. E. *Quantum Theory of Solids*; Clarendon: Oxford, **1955**.

43. Yannoni, C. S.; Clarke, T. C. *Phys. Rev. Lett.* **1983**, *51*, 1191.

44. Wintle, H. J. *IEEE Trans. Electr. Insul.* **1977**, *12*, 97.

45. For a review see Heeger, A. J.; Kivelson, S.; Schrieffer, J. R.; Su, W.-P. *Reviews of Modern Physics* **1988**, *60*, 781.

46. For a short review, see Dissado, L. A.; Fothergill, J. C. *Electrical Degradation and Breakdown in Polymers*; Edited by Stevens, G. C.; Peter Peregrinus Ltd.: London, 1992, Ch. 9.

47. Cohen, M. H.; Lekner, J. *Phys. Rev.* **1967**, *158*, 305.

48. For a short review, see Dissado, L. A.; Fothergill, J. C. *Electrical Degradation and Breakdown in Polymers*; Edited by Stevens, G. C.; Peter Peregrinus Ltd.: London, 1992, Ch. 14.

49. Boggs, S.; Kuang, J. *IEEE Electrical Insulation Magazine* **1998**, *14*, 5.

50. Wu, K.; Dissado, L. A.; Okamoto, T. *Appl. Phys. Lett.* **2004**, *85*, 4454.

51. Von Hippel, A. *J. Appl. Phys.* **1937**, *8*, 815.

52. Fröhlich, H. *Proc. Roy. Soc., London* **1937**, *A160*, 230.

53. a) Watson, P. K. *IEEE Trans. Electr. Insul.* **1987**, *22*, 129. b) Mazzanti, G.; Montanari, G. C.; Alison, J. M. *IEEE Trans. Dielectr. Electr. Insul.* **2003**, *10*, 187. c) Dissado, L. A.; Paris, O.; Ditchi, T.; Alquie, C.; Lewiner, J. *Annu. Rep. CEIDP (IEEE Pub. No. 99CH36319)* **1999**, 23.

54. a) Dissado, L. A.; Fothergill, J. C. *Electrical Degradation and Breakdown in Polymers*; Edited by Stevens, G. C.; Peter Peregrinus Ltd.: London, 1992, Ch. 14. b) Blythe, A. R. *Electrical Properties of Polymers*; Cambridge University Press: Cambridge, **1979**, Ch. 6. c) Ku, C. C.; Liepens, R. *Electrical Properties of Polymers: Chemical Principles*; Hanser Publishers: Munich, 1987, Ch. 4.

55. Artbauer, J. *J. Phys. D* **1996**, *29*, 446.

56. Stark, K. H.; Garton, C. G. *Nature* **1955**, *176*, 1225.

57. a) Stratton, R. *Progr. Dielectrics* **1957**, *3*, 235. b) Mizutani, T.; Hikita, M.; Umemura, A.; Ieda, M. *Ann. Rep. Conf. Elec. Insul. & Diel. Phen.* 1989, 315 – 320. as referenced in Dissado, L. A.; Fothergill, J. C. *Electrical Degradation and Breakdown in Polymers*; Edited by Stevens, G. C.; Peter Peregrinus Ltd.: London, 1992.

58. Nigrey, P. J.; MacDiarmid, A. G.; Heeger, A. J. *Chem. Commun.* **1979**, *96*, 594.

59. Coakley, K. M.; McGehee, M. D. *Chem. Mater.* **2004**, *16*, 4533.

60. Petterson, L. A. A.; Ghosh, S.; Inganäs, O. *Organic Electronics* **2002**, *3*, 143.

61. Ouyang, J.; Xu, Q.; Chu, C.-H.; Yang, Y.; Li, G.; Shinar, J. *Polymer* **2004**, *45*, 8443.

62. Lapkowski, M.; Pron, A. *Synth. Met.* **2000**, *110*, 79.

63. Chen, X.; Inganäs, O. *J. Phys. Chem.* **1996**, *100*, 15202.

64. Garreau, S.; Louarn, G.; Buisson, J. P.; Froyer, G.; Lefrant, S. *Macromolecules* **1999**, *32*, 6807.

65. Rabuffi, M.; Picci, G. *IEEE Trans. on Plasma Science* **2002**, *30*, 1939.

66. Reed, C. W.; Cichanowski, S. W. *IEEE Trans. on Dielectrics and Electrical Insulation* **1994**, *1*, 904.

67. Walgenwitz, B.; Tortai, J.-H.; Bonifaci, N.; Denat, A. IEEE 2004 Inter. Conf. on Solid Dielectrics, Toulouse, France.

68. Tsumura, A.; Koezuka, K.; Ando, T. *Appl. Phys. Lett.* **1986**, *49*, 1210.

69. Horowitz, G.; *Adv. Mater.* **1998**, *10*, 365.

70. Katz, H. E.; Bao, Z. *J. Phys. Chem. B* **2000**, *104*, 671.

71. Dimitrakopoulos, C. D.; Mascaro, D. J. *IBM J. Res. And Dev.* **2001**, *45*, 11.

72. Dimitrakopoulos, D. D.; Malenfant, P. R. L. *Adv. Mater.* **2002**, *14*, 99.

73. Horowitz, G. *J. Mater. Res.* **2004**, *19*, 1946.

74. Brown, A. R.; Jarrett, C. P.; de Leeuw, D. M.; Matters, M. *Synth. Met.* **1997**, *88*, 37.

75. Horowitz, G.; Hajlaoui, R.; Bouchriha, H.; Bourguiga, R. Hajlaoui, M. *Adv. Mater.* **1998**, *10*, 923.

76. Kelley, T. W.; Muyres, D. V.; Baude, P. F.; Smith, T. P.: Jones, T. D. in *Organic and Polymeric Materials and Devices* eds. Blom, P. W. M.; Greenham, N. C.; Dimitrakopoulos, C. D.; Frisbie, C. D. (*Mater. Res. Soc. Symp. Proc.*) Warrendale, PA 2003, *771*, p. 169.

77. Wang, G. M.; Swensen, J.; Moses, D.; Heeger, A. J. *J. Appl. Phys.* **2003**, *93*, 6137.

78. Dimitrakopoulos, C. D.; Brown, A. R.; Pomp, A. *J. Appl. Phys.* **1996**, *80*, 2501.

79. Vissenberg, M. C. J. M.; Matters, M. *Physical Review B* **1998**, *57*, 12964.

80. Dimitrakopoulos, D. D.; Malenfant, P. R. L. *Adv. Mater.* **2002**, *14*, 99. in reference to Silinsh, E. A.; Cğápek, V. *Organic Molecular Crystals; Interaction Localization and Transport Phenomena*; AIP: New York 1994, Ch. 7.

81. Clayden, J.; Lund, A.; Vallverdú, L.; Helliwell, M. *Nature,* **2004**, *431*, 966.

82. Collet, J. Tharaud, O., Chapoton, A.; Vuillaume, D. *Appl. Phys. Lett.* **2000**, *76*, 1941.

83. Dimitrakopoulos, C. D.; Purushothaman, S.; Kymissis, J.; Callegari, A.; Shaw, J. M. *Science* **1999**, *283*, 822.

84. Veres, J.; Ogier, S.; Leeming, S.; Cupertino, D.; Khaffaf, S. M. *Adv. Funct. Mater.* **2003**, *13*, 199.

85. Veres, J.; Ogier, S.; Leeming, S.; Cupertino, D.; Khaffaf, S. M.; Lloyd, G. *Proc. of SPIE: Organic Field Effect Trans. II* Eds. Dimitrakopoulos, C. D.; Dodabalapur, A. Bellingham, WA **2003**, 147.

86. Lu, J.; Pinto, N. J.; MacDiarmid, A. G. *J. Appl. Phys*. **2002**, *92*, 6033.

87. (a) Epstein, A. J.; Hsu, F.-C.; Chiou, N.-R.; Prigodin, V. N. *Current Appl. Phys.* **2002**, *2*, 339. (b) Epstein, A. J.; Hsu, F.-C.; Chiou, N.-R.; Waldmann, O.; Park, J. H.; Kim, Y.; Prigodin, V. N. *Proc. SPIE-Organic Field Effect Transistors II* **2003**, *5217*, 141.

88. Epstein, A. J.; Park, J. H.; Youngmin, K.; Hsu, F.-C.; Chiou, N.-R.; Waldmann, O.; Prigodin, V. N. *Polym. Prepr. (Am. Chem. Soc., Div. Polym. Chem.)* **2004**, *45(1)*, 149.

89. Nilsson, D.; Chen, M.; Kugler, T.; Remonen, T.; Armgarth, M.; Berggren, M. *Adv. Mater*. **2002**, *14*, 51.

90. Thackeray, J. W.; White, H. S.; Wrighton, M. S. *J. Phys. Chem.* **1985**, *89*, 5133.

91. Zhu, Z.-T.; Mabeck, J. T.; Zhu, C.; Cady, N. C.; Batt, C. A.; Malliaras, G. G. *Chem. Commun*. **2004**, 1556.

Chapter 2

Quantitative Analysis of Amide Crosslinking in

Heat Treated Polyelectrolyte Multilayer Films

2.1 Introductory Remarks

The expanding ability to modify the chemistry of pre-assembled multilayer films has significantly enhanced the utility of the layer-by-layer assembly deposition technique for many diverse applications. Some examples of the capabilities used for these pre-assembled films include the formation of microporous structures upon exposure to acidic solutions,[92] the fabrication of refractive index gradients with the internal synthesis of silver nanoparticles,[93] and the formation of structurally stable microspheres with chemically activated cross-linking of 3-dimensional templated films.[94] Another simple way to modify the chemistry of these types of films has been demonstrated with the formation of amide crosslinks in poly(allylamine hydrochloride)/poly(acrylic acid) (PAH/PAA) multilayer films with heat treatment.[95] The crosslinking of these films has been shown to improve their utilization as Cu^{2+} templated ion-selective membranes[96] and as a passivation layer for aluminum substrates.[97]

Qualitatively, the degree of crosslinking of PAH/PAA multilayers has been shown with infrared spectroscopy to depend on the pH of the polyelectrolyte solutions and the heat treatment temperature.[95,97] The former trend implies a direct conversion of the ionic interactions between the carboxylate and ammonium groups into amide crosslinks upon heating. A more quantitative approach is taken herein by performing a Gaussian fit analysis of reflective Fourier transform infrared (FT-IR) spectra obtained from multilayer films deposited at different pH or heat treated to various temperatures. The results from the fit analysis were used to calculate the degree of

46

amide cross-linking in these films as a function of solution pH, post-assembly heat treatment temperature, and a combination of both. A compilation of this data was used to describe the degree of conversion for the condensation (amide crosslinking) reaction and its dependence on the heat treatment temperature. The results will be addressed further in Chapter 3 as a means to improve the understanding of the relationship between the crosslinking characteristics for the PAH/PAA multilayer films and their dielectric strength. Additionally, PAH was substituted with linear poly(ethyleneimine) (PEI) to investigate the formation of tertiary amide crosslinks within the multilayers. The substitution of the tertiary amide for the secondary amide will be addressed further in Chapter 3 to investigate its influence on the electronic breakdown of multilayer films.

2.2 Experimental

The polymers used in this study, poly(acrylic acid) (M_w = 90,000), poly(allylamine hydrochloride) (M_w = 60,000), and linear poly(ethylenimine) (M_w = 25,000), were purchased from Polysciences, Inc. Polyelectrolyte solutions (10 mM) were pH-adjusted with NaOH and HCl using an Orion model 230A pH meter. Each monolayer deposition cycle (~ 15 min) was followed with multiple rinse steps in deionized (18 MΩ·cm) H_2O in a Carl Zeiss Microm DS-50 automatic slide stainer. A multi-step process involving 15 min sonication steps in water, 1,1,1-trichloroethane, acetone, and methanol and 15 min in a Harrick PDC – 236 plasma cleaner was used to the clean glass slides. Aluminum and gold were thermally evaporated onto glass slides at a rate of 4 – 5 Å/s and 3 Å/s, respectively, in an Explorer 18 Denton Vacuum system (< 10^{-7} Torr) using a Telemark model 860 deposition controller. The gold substrates were initially coated with a self-assembled monolayer of 16-mercaptohexadecanoic acid by submerging the substrate for 1 day into a 1 mM ethanol solution. Film thicknesses were measured with a Tencor

P-10 surface profiler at a stylus force of 0.6 mg. The multilayer films were heated at 85 ºC under N_2 for 1 hour and then heated at a desired temperature under vacuum for approximately 5 - 6 hours. The absorbance spectra were obtained using a Nexus 470 Fourier transform infrared spectrometer (FT-IR) in the reflectance mode.

2.3 Results and Discussion

2.3.1 Absorbance of Heat Treated PAH/PAA Multilayer Films

The degree of carboxylic acid, carboxylate, amide, and acetic anhydride present in the multilayer film was used to determine the degree of ionic interactions and amide crosslinking. The concentration of these functional groups was determined from the absorbance of their carbonyl stretch in the reflective FT-IR spectra of the films. The absorbance contribution from each of these functional groups was compared after using a Gaussian fit analysis program to deconvolute their respective peaks within the infrared spectrum. Representative fits for a sample, before and after heat treatment, are illustrated with the assigned peaks in Figure 2-1. An additional peak at 1570 cm^{-1} was also used for samples deposited at a higher pH to account for the NH_2 bend of PAH. Up to seven peaks could be used simultaneously to perform the fit and were assigned previously reported energies.[98] Although the peaks were not fixed to these assigned values, they generally stayed within a range of 10 cm^{-1}. An additional broad peak was required to properly fit the absorbance due to the carbonyl stretch of the amide group (Amide I), which was attributed to the formation of a dimerized form of the amide groups through hydrogen bonding. Similar observations have been noted for the carboxylic acid groups in these PEMs.[99]
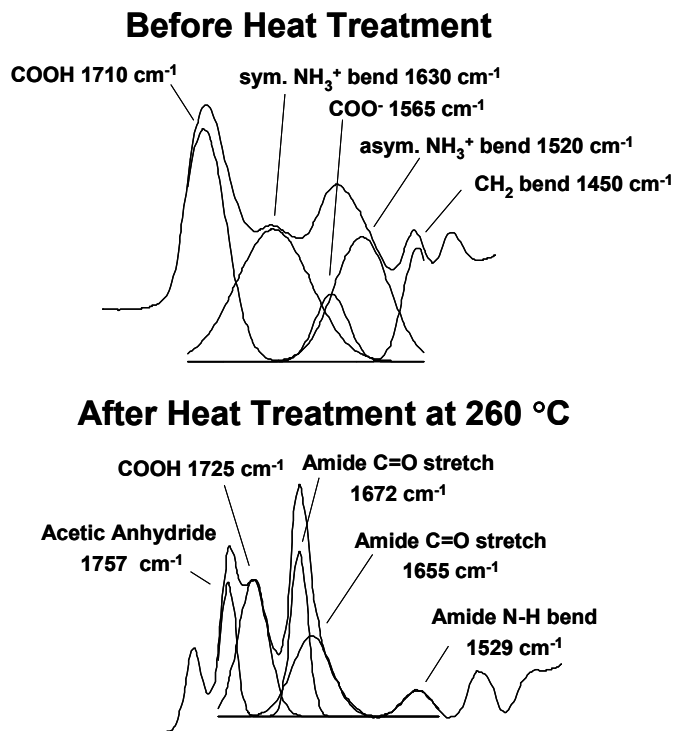
Figure 2-1. Examples of Gaussian fit analysis performed on a PAH/PAA multilayer film deposited at a pH of 2.1 demonstrating the peaks used to quantify the degree of ionization and amide crosslinking.

In order to use the fit analysis to calculate the degree of crosslinking within the heat treated PAH/PAA films, the effective molar absorbtivity (absorbance units/number of bilayers) of the carbonyl stretch for each functional group had to be calculated to account for their variations in absorbance with film thickness. The proportionality constants for the molar absorbtivities were ignored since they cancel each other out in the calculation of functionalization for PAA (Equation 2.1). The reflective FT-IR absorbance spectra were obtained from heat treated PAH/PAA films with 20, 40, 60, and 80 bilayers that were deposited at a pH of 3.0. As shown in Figure 2-2a, a linear growth in thickness with an increase in number of bilayers was maintained after heat treating the PAH/PAA films at 260 °C under vaccuum. The initial bilayer thickness of approximately 54 Å, which agrees with previously reported results,[100] decreased to about 43 Å after heat treatment. Although a decrease in film thickness was observed, the level of shrinkage

(21%) was independent of the number of bilayers. This independence implies a uniform distribution of crosslink density throughout the film thickness. A Gaussian fit analysis was then used to deconvolute the absorbance spectra from each of these films. The results from these fits are shown in Figure 2-2b with the absorbance of the carbonyl stretches for each of the functional groups on PAA as a function of number of bilayers. A linear fit of this data was used to determine the molar absorbtivity (slope) of each functional group needed to calculate the degree of crosslinking.
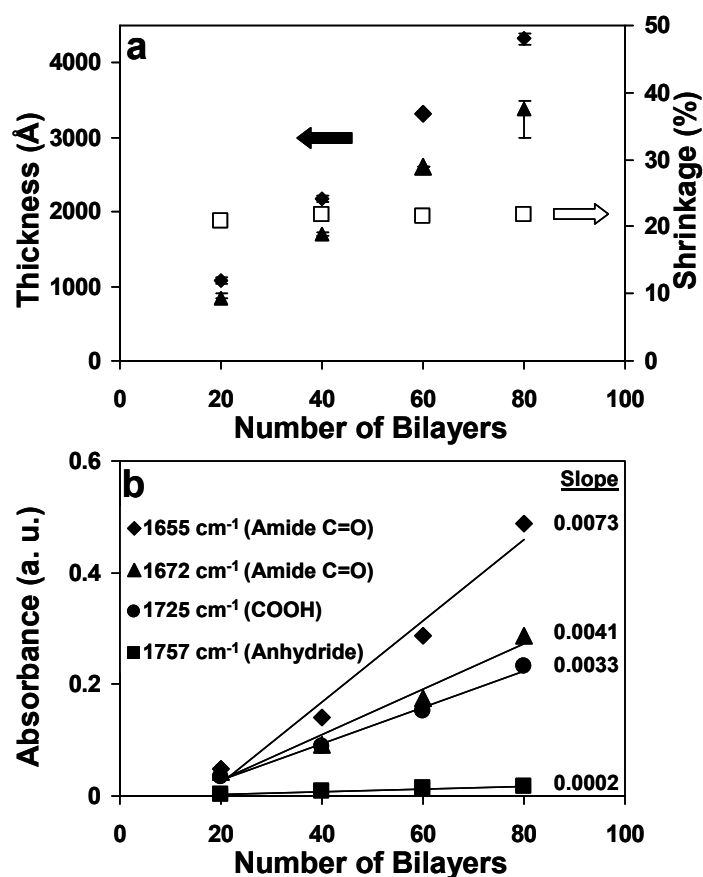
Figure 2-2. A) Thickness measurements of PAH/PAA films (deposited at a pH of 3.0), before (♦) and after (▲) heat treatment at 260 °C under vacuum, and the shrinkage in film thickness (□) as a function of number of bilayers. B) Linear fit of the absorbance for the carbonyl peaks of select functional groups as a function of number of bilayers.

2.3.2 Quantitative Analysis of the Degree of Crosslinking within PAH/PAA

2.3.2.1 Function of solution pH

The reflective FT-IR absorbance from several PAH/PAA films, deposited from different solutions with varying pH, were used to investigate the correlation between the ionic interaction and the formation of crosslinks. The absorbance spectra in Figure 2-3 were obtained from these samples before (a) and after (b) heat treating at 260 ºC under vacuum. The multilayer films were deposited onto an aluminum surface using solutions with a pH range of 2.1 to 6.0 in order to correlate with the breakdown measurements in the following chapter. However, at pH values greater than 6.0, the aluminum separated from the glass slide. Therefore, the PAH/PAA films were deposited at pH values of 7.0, 8.0, and 9.0 onto a gold substrate that was pretreated with a self-assembled monolayer to form carboxylate groups on the surface.
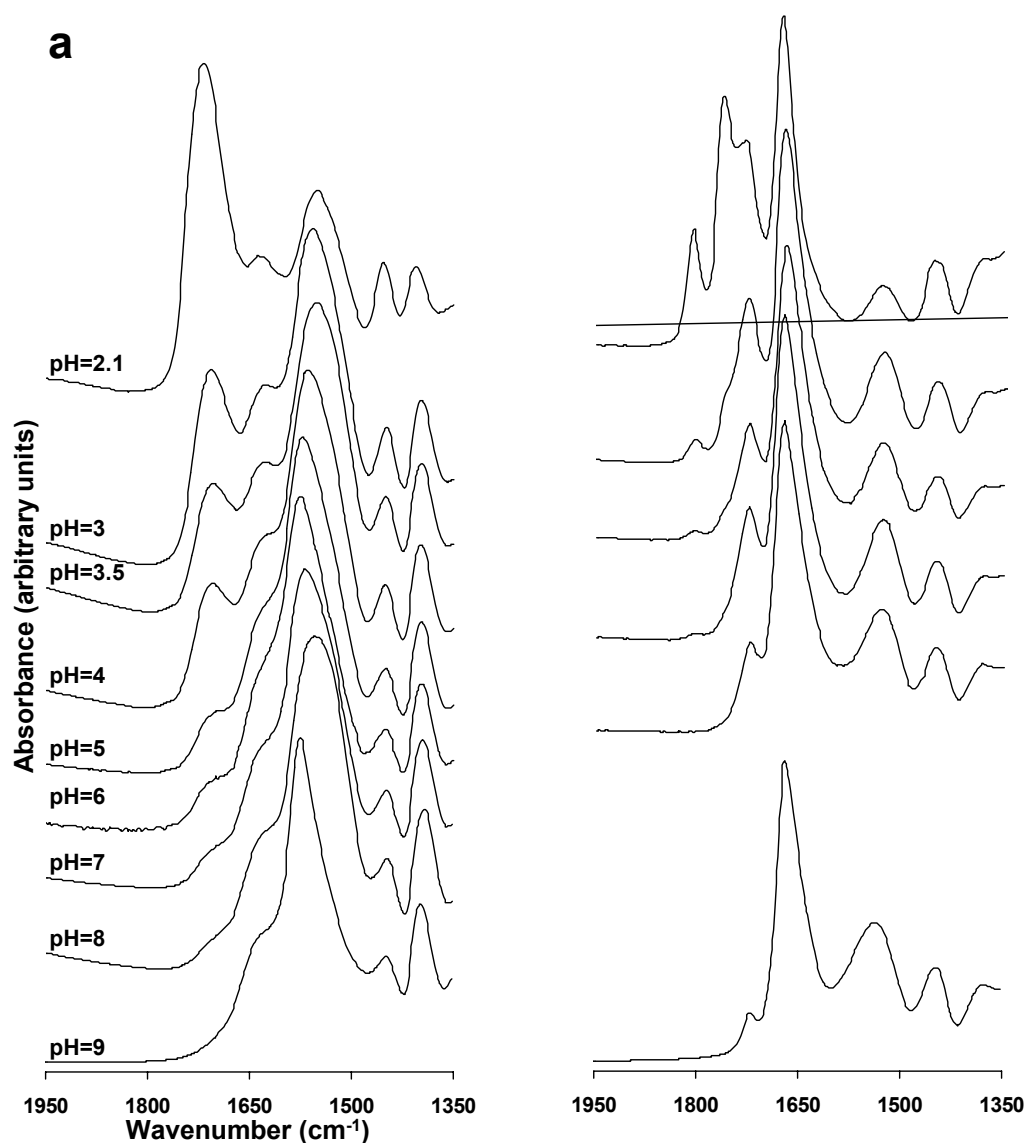
Figure 2-3. FT-IR spectra obtained in the reflection mode, before (a) and after (b) heat treatment at 260 °C under vacuum, of PAH/PAA samples that were deposited with a wide range of solution pH.

The concentration of functional groups on the PAA was compared before and after heat treating the PAH/PAA multilayers to determine the correlation between the degree of ionic crosslinking and the density of amide crosslinks. A higher degree of ionization of PAA has previously been shown to be present when incorporated into polyelectrolyte mutilayers, as compared to pure cast films, and was attributed to its ionic interaction with PAH.[98] The same calculation was used here to verify the degree of ionization in these samples before heat treatment. This calculation was based on the peak heights of the carbonyl stretches for the

carboxylic acid and the carboxylate anion due to the similarity in their molar absorbtivity. As shown in Figure 2-4a, the degree of ionization in these films agreed with the reported values below a pH of 6.5. The degrees of ionization for the films deposited onto the gold surface were also in agreement at low pH and continued the plateau for the upper limit above a pH of 6.0.

$$\frac{\dfrac{\left[\nu(\text{CONH})_{1672cm^{-1}}\right]}{\varepsilon_{\text{CONH}(1672cm^{-1})}} + \dfrac{\left[\nu(\text{CONH})_{1655cm^{-1}}\right]}{\varepsilon_{\text{CONH}(1655cm^{-1})}}}{\dfrac{\left[\nu(\text{COOH})\right]}{\varepsilon_{\text{COOH}}} + \dfrac{\left[\nu(\text{COO-})\right]}{\varepsilon_{\text{COO-}}} + \dfrac{\left[\nu(\text{CONH})_{1672cm^{-1}}\right]}{\varepsilon_{\text{CONH}(1672cm^{-1})}} + \dfrac{\left[\nu(\text{CONH})_{1655cm^{-1}}\right]}{\varepsilon_{\text{CONH}(1655cm^{-1})}} + \dfrac{\left[\nu(\text{Anhydride})\right]}{\varepsilon_{\text{Anhydride}}}} \times 100 \qquad (2.1)$$

The degree of amide crosslinking was determined from the results of the fit analysis of the absorbance spectra obtained from the same PAH/PAA multilayers after they were heat treated. The absorbance values and molar absorbtivities of the carbonyl stretches from the acetic anhydride, carboxylic acid, carboxylate anion and amide functional groups were used in Equation 2.1 to calculate the degree of crosslinking in respect to the PAA. As shown in Figure 2-4b, the degree of crosslinking followed a close trend with the degree of ionization within the pH range of 2.1 – 6.0. Above this pH range, the degree of crosslinking showed a slight decrease and an additional peak near 1570 cm^{-1} was required to obtain a good fit of the absorbance spectra. This absorbance was attributed to the NH$_2$ bending vibration since its emergence would be expected with the deionization of ammonium cation above a pH of 6.5. The similarity between the degree of ionization and amide crosslinking of PAA for films deposited at a low pH and the trends observed when deposited at a high pH indicate a high conversion of the ionic interactions to amide crosslinks upon heat treatment.

It should also be noted that after heat treatment the peaks for the symmetric and asymmetric carbonyl stretches of the acetic anhydride (1760 cm^{-1} and 1810 cm^{-1}, respectively) become more predominant when using solutions with a pH lower than 3.5. Since this trend correlates with a

decrease in ionization past 50%, it may imply the formation of acetic anhydride predominantly between neighboring carboxylic acid groups within the same PAA chain. If this formation occurred between different PAA chains, the presence of acetic anhydride after heat treatment would persist at higher values of pH in a manner more similar to that observed for the carboxylic acid groups.
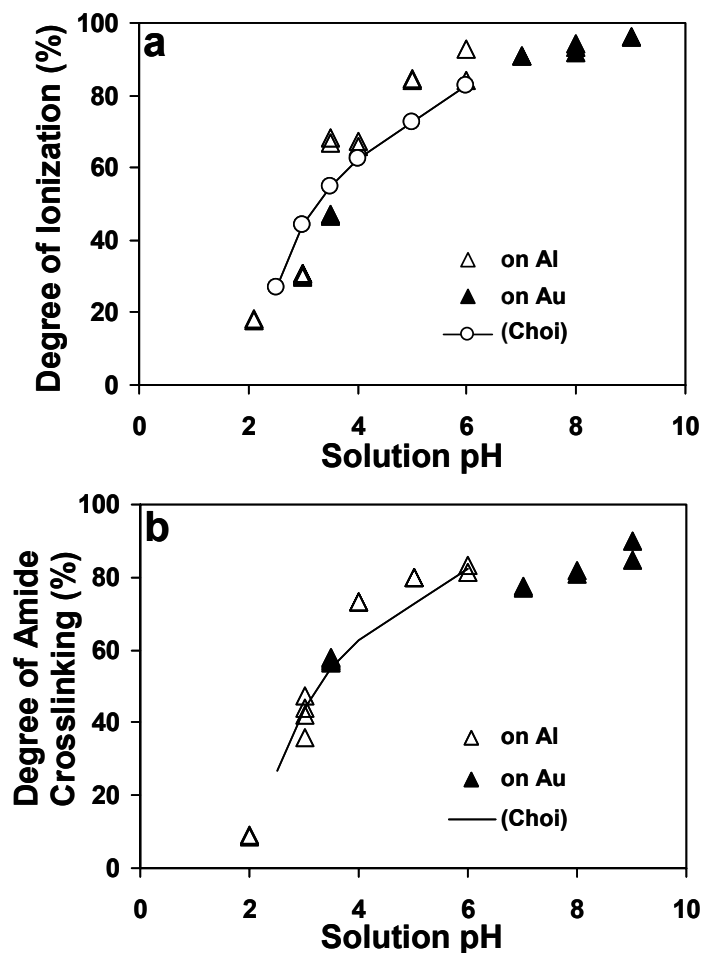
Figure 2-4. The initial degree of ionization of PAA (a) and the resulting degree of amide cross-linking with heat treatment at 260 °C under vacuum (b), both as a function of the pH used for the polyelectrolyte solutions. At least 2 data points are included for each value of pH (2 sets of data are included at a pH of 3.5; 1 for Al and 1 for Au). The results reported by Choi and Rubner are also indicated as a reference.

2.3.2.2 Function of heat treatment temperature

The degree of amide crosslinking was also investigated for PAH/PAA multilayer films as a function of heat treatment temperature. The absorbance spectra in Figure 2-5a were obtained from a film with 40 PAH/PAA bilayers deposited at a pH of 3.5. The top absorbance spectrum was obtained from the film before heat treatment and each sequential spectrum below it was obtained after heat treating the film at a higher temperature under vacuum. Similar absorbance spectra were also obtained from films deposited at pH values of 2.1, 5.0, and 6.0, which can be found in Appendix A. The dashed lines in Figure 2-5a are included to act as a guide for the transitions observed upon heat treatment.

The results from the Gaussian fit analysis of the absorbance spectra obtained from these films are shown in Figure 2-5b as a function of heat treatment temperature. A combination of seven peaks from the ones used in the examples in Figure 2-1, for samples before and after heat treatment, were used to perform this fit analysis. After the sample is heat treated at 120 ℃, the degree of ionization remains unaffected, but starts to decrease after heating to 140 ℃. As the heat treatment temperature was increased to 240 ℃, the degree of ionization continues to decrease linearly with a corresponding increase in the degree of amide crosslinking. The transition to the covalently crosslinked state appears to be complete at this point as little change is observed after heat treating at 260 ℃. It should be noted that the degree of ionization did agree with values discussed in Figure 2-4, but the degree of amide crosslinking was slightly higher for these samples due to the inability to include the small acetic anhydride peak in the fit analysis.
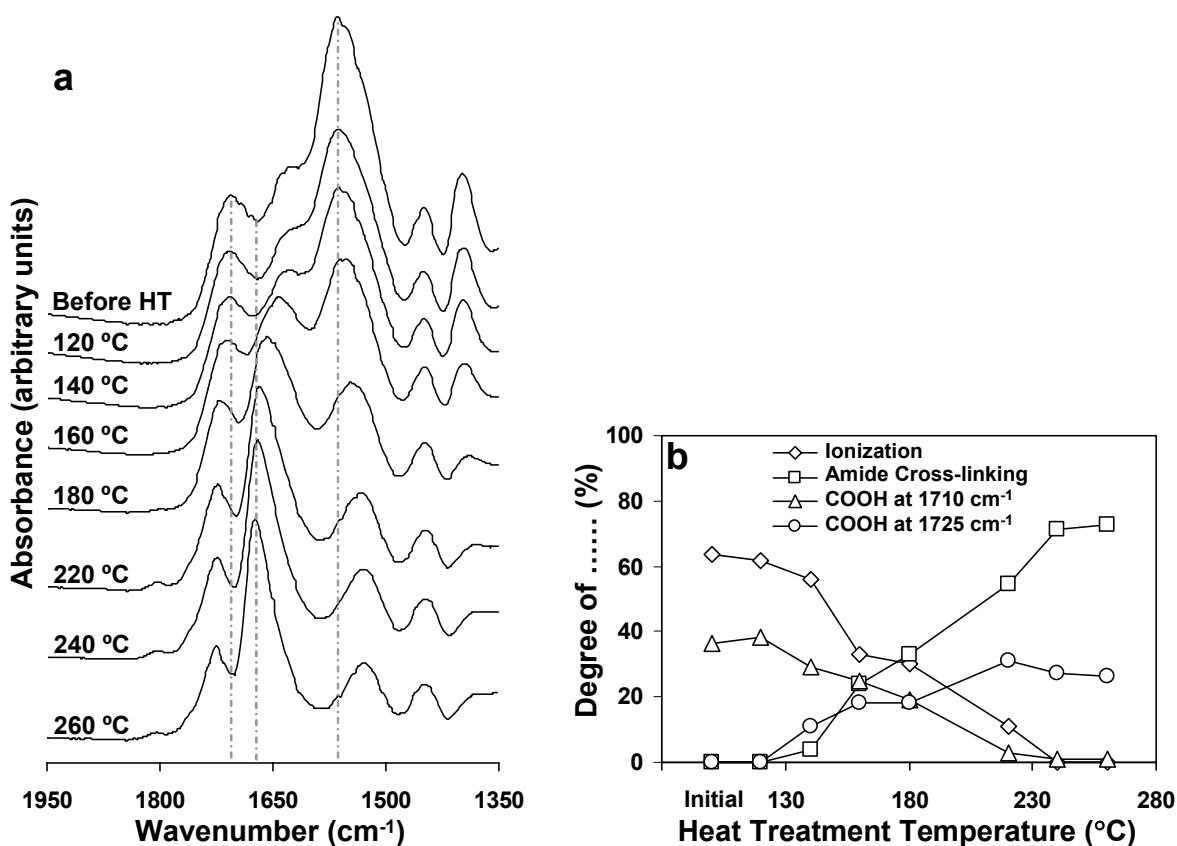
Figure 2-5. a) The reflective FT-IR absorbance spectra obtained from the PAH/PAA multilayers (deposited at a pH of 3.5) before heat treatment and each time after heating them with an incremental increase in temperature. b) Results from the Gaussian fit analysis of the absorbance spectra as a function of heat treatment temperature.

The absorbance peak due to the carbonyl stretch of the carboxylic acid was also observed with a correlating transition as the annealing temperature was increased. The energy of its absorbance peak (1710 cm^{-1}) has previously been noted as being red-shifted for PAH/PAA multilayers due to either hydrogen bonding with water or its formation into a dimerized state.[99] Although a similar energy was observed for these PAH/PAA multilayers before heat treatment, the peak shifted to a higher energy of approximately 1725 cm^{-1} after being heated, regardless of the deposition conditions. A fit analysis was performed using a combination of both of these peaks to determine their transition behavior. The peaks at 1710 cm^{-1} and 1725 cm^{-1} in Figure 2-5b appear to follow similar trends with an increase in heat treatment temperature as do the degree

of ionization and amide crosslinking, respectively. Since less moisture is expected to be present in the films after the formation of amide crosslinks,[101] the blue-shift of this peak is likely due to the decomplexation of water from the carboxylic acid.

2.3.3 Heat-induced Crosslinking within PEI/PAA Films

The layer-by-layer deposition of similar multilayer films was conducted using linear poly(ethylenimine) (PEI) as the polycation, instead of PAH, as a means to investigate the crosslinking of these type of films with a tertiary amide. The deposition of these films involved using an aqueous PEI solution with a low pH of 2.2 to induce ionization of this polyelectrolyte and an aqueous PAA solution with a pH of 2.7.   The linear growth in thickness with an increasing number of bilayers was also maintained for these films after heat treatment, as shown in Figure 2-6b. The initial bilayer thickness was 49 Å, which decreased to 36 Å after heat treatment at 260 ºC under vacuum.

The formation of tertiary amide crosslinks was investigated by analyzing the reflective FT-IR absorbance spectra obtained from a heat treated PEI/PAA film with 60 bilayers. As shown in Figure 2-6a, the absorbance spectrum was obtained from this film before heat treatment and each time after it was heated at a higher temperature. The dashed lines are present to assist with the observation of changes that occur between spectra obtained from samples heat treated at different temperatures.
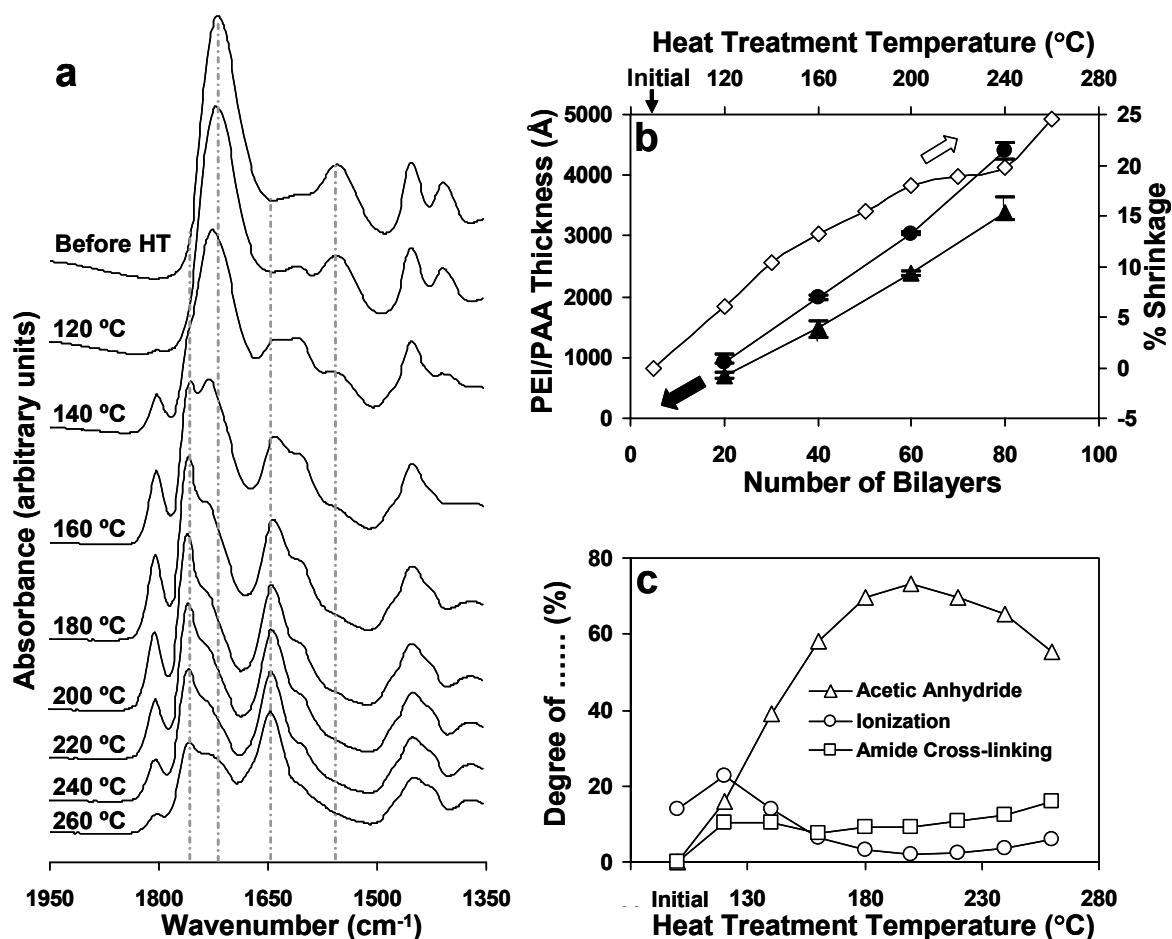
Figure 2-6. a) The reflective FT-IR absorbance spectra obtained before heat treatment (HT) and with incremental increases in heat treatment temperature of 60 PEI/PAA bilayers. b) The film thickness of the PEI/PAA multilayers before (●) and after (▲) heat treatment with an increase in the number of bilayers. The degree of shrinkage (○) in film thickness is also shown as a function of heat treatment temperature. c) Results from the Gaussian fit analysis of the absorbance spectra as a function of heat treatment temperature.

The formation of tertiary amide crosslinks was indicated with the emergence of the amide carbonyl stretch at 1642 cm^{-1} (Figure 2-6a) and the decrease in absorbance for the N-H bending above 3000 cm^{-1}(not shown). A Gaussian fit analysis was used to deconvolute the contribution of each functional group to the absorbance observed for the energy range of 1530 – 1845 cm^{-1} of each spectrum. Similar absorbance energies were used to perform this fit analysis as were used with the PAH/PAA multilayers. The differences included using a peak at 1605 cm^{-1} for the

NH$_2^+$ of PEI, lowering the energy (1642 cm^{-1}) to fit a single peak for amide carbonyl stretch, and eliminating the peaks due to the NH$_3^+$ bending. Even before heat treating the sample, both types of peaks (1710 cm^{-1} and 1725 cm^{-1}) for the carbonyl stretch of the carboxylic acid were required to provide a proper fit of the absorbance spectrum. As shown in Figure 2-6c, the post-assembly heat treatment of the sample at 120 ℃ initiated the formation of both the acetic anhydride and the tertiary amide. As the heat treatment temperature was increased further, the absorbance due to the acetic anhydride increased significantly until it appeared to decrease at temperatures above 200 ℃. This degradation was also indicated with a sudden increase in shrinkage of the film thickness above 240 ℃ (Figure 2-6b). The degree of tertiary amide crosslinking appeared to decrease slightly after the sample was heated at 140 ℃ and then gradually increased to 15% as the heat treatment temperature was increased to 260 ℃. This value agrees with the degree of crosslinking observed with the PAH/PAA multilayers deposited from solutions with similar pH values (Figure 2-4). The degree of ionization of PAA decreased for this PEI/PAA multilayer film with an increase in heat treatment temperature above 120 ℃, but then appeared to increase slightly when the film was heated above 200 ℃. A broad peak due to the carbonyl stretch of the carboxylate anion also remained after annealing at 260 ℃. These trends suggest decomposition of the acetic anhydride into a carboxylate type functional group at temperatures above 200 ℃.

2.4 Conclusion

The results obtained from the fit analysis of the absorbance spectra for these polyelectrolyte multilayer films were used here to provide a quantitative description of the reactions that occur when they are heat treated.   The transformation of the ionic interactions between the polyelectrolytes to the amide crosslinks were initiated at approximately 140 ℃ under a low

pressure environment. This conversion was completed with a high efficiency around 240 ºC. A blue-shift was also observed for the peak due to the carboxylic acid, which was attributed to the reduction of moisture in the film with an increase in crosslink density. At a high pH, the degree of crosslinking appeared to be limited by both the decreasing level of ionization of PAH and the maximum degree of ionization of PAA. The formation of acetic anhydride also appeared to occur between neighboring carboxylic acid groups on the PAA when the degree of ionization was below 50% for films deposited at a low pH. The formation of tertiary amide crosslinks was also demonstrated with the heat treatment of PEI/PAA multilayers and was shown to occur at a slightly lower temperature. Since these films required deposition at a low pH, a high concentration of acetic anhydride was present after the films were heat treated, but they appeared to decompose into carboxylates at temperatures above 200 ºC.

2.5 References

92. Mendelsohn, J. D.; Barrett, C. J.; Chan, V. V.; Pal, A. J.; Mayes, A. M.; Rubner, M. F. *Langmuir* **2000**, *16*, 5017.

93. Nolte, A. J.; Rubner, M. F.; Cohen, R. E. *Langmuir* **2004**, *20*, 3304.

94. Schuetz, P.; Caruso, F. *Adv. Funct. Mater.* **2003**, *13*, 929.

95. Harris, J. J.; DeRose, P. M.; Bruening, M. L. *J. Am. Chem. Soc.* **1999**, *121*, 1978.

96. Balachandra, A. M.; Dai, J.; Bruening, M. L. *Macromolecules* **2002**, *35*, 3171.

97. Dai, J.; Sullivan, D. M.; Bruening, M. L. *Ind. Eng. Chem. Res.* **2000**, *39*, 3528.

98. Choi, J.; Rubner, M. F. *Macromolecules* **2005**, *38*, 116.

99. Xie, A. F.; Granick, S. *Macromolecules* **2002**, *35*, 1805.

100. Shiratori, S. S.; Rubner, M. F. *Macromolecules* **2000**, *33*, 4213.

101. Durstock, M. F. Ph. D. Thesis, Department of Materials Science and Engineering, Massachusetts Institute of Technology, Cambridge, 1999.

Chapter 3

Breakdown Strength of Crosslinked

Layer-by-Layer Assembled Films

3.1 Introductory Remarks

The development of insulating polymeric materials continues to increase because of their tailorability and processability, but the improvement in understanding of their dielectric properties is challenging because of their entropic nature. This understanding is required to improve the ability to use polymeric materials as thin dielectric layers for high voltage applications. Currently, a thin polymer film with a dielectric strength near 10 MV/cm is desired for the low cost development of high energy density, pulsed power capacitors.[102,103]

The incorporation of layer-by-layer assembled films as ultra-thin, pinhole-free insulating layers into several types of electronic devices was investigated. The previous chapter entailed characterizing the formation of amide crosslinks in these films as a function of post-assembly heat treatment temperature and the pH conditions used during deposition. The increase of mechanical stability,[104] the restriction of ionic conductivity,[105] and the elimination of defects in these PAH/PAA multilayers with crosslinking may improve their dielectric strength for use in high voltage applications. The dielectric strength of these multilayer films was investigated by incorporating them as insulating layers into parallel plate capacitors and then operating them at high voltages. The following chapters will discuss the application of these films as a dielectric material for different types of thin film transistors.

The dielectric strengths of these multilayer films were investigated by applying a voltage across the parallel plate capacitors and increasing it until breakdown. The initial tests were

conducted using a standard technique involving the application of an individual probe to the bottom electrode and to the free standing top electrode. The observation of a self-healing clearing effect then necessitated the development of another testing technique to avoid premature ending of the breakdown test due to the occurrence of these events under the probe tip. This new test involved using capacitors with an overlaying architecture of perpendicular electrodes with multilayer films stacked in between them. The capacitance and dielectric strength of PAH/PAA multilayer films were then investigated by increasing the applied voltage and obtaining dielectric measurements until breakdown occurred. Additionally, the breakdown strengths of these devices as a function of crosslink density and film thickness were studied. Lastly, the breakdown strengths of devices with crosslinked PEI/PAA multilayer films as the insulating layer were tested as a means to investigate the effect tertiary amide crosslinks have on the insulating properties of these multilayer films.

3.2 Experimental

The polymers used were poly(acrylic acid) (M_w = 90,000), poly(allylamine hydrochloride) (M_w = 60,000), and linear poly(ethylenimine) (M_w = 25,000), which were purchased from Polysciences, Inc. Polyelectrolyte solutions (10 mM) were pH adjusted with NaOH and HCl using an Orion model 230A pH meter. Each monolayer deposition cycle (~ 15 min) was followed with multiple rinse steps in deionized (18 MΩ·cm) H_2O in a Carl Zeiss Microm DS-50 automatic slide stainer. A multi-step process involving 15 min sonification steps in water, 1,1,1-trichloroethane, acetone, and methanol and 15 min in a Harrick PDC – 236 plasma cleaner was used to the clean glass slides. Top and bottom aluminum electrodes were thermally evaporated at a rate of 1 and 4 – 5 Å/s, respectively, to a thickness of 350 Å in an Explorer 18 Denton

Vacuum system ($< 10^{-7}$ Torr) using a Telemark model 860 deposition controller. Film thicknesses were measured with a Tencor P-10 surface profiler at a stylus force of 0.6 mg. The multilayer films were heated at 85 ºC under $N_2(g)$ for 1 hour and then heated at a desired temperature under vacuum for approximately 5 – 6 hours. The absorbance spectra were obtained using Nexus 470 Fourier transform infrared spectrometer in the reflectance mode. Capacitance and dielectric constant measurements were obtained using a Novocontrol broadband dielectric spectrometer. Breakdown measurements were performed with a Keithley 237 High Voltage Source Measuring Unit® while being observed under a Carl Zeiss Stemi DV4 microscope.

3.3 Results and Discussion

3.3.1 Influence of Heat Treatment on the Dielectric Strength of PAH/PAA Films

The initial tests of the dielectric strength for PAH/PAA multilayer films entailed using the device architecture shown with the schematic diagram in Figure 3-1. Several samples were fabricated with the layer-by-layer deposition of 40 PAH/PAA bilayers onto an aluminum coated (1000 Å) glass slide, but were then heat treated at different temperatures. These multilayers were deposited at a pH of 3.5 with a bilayer thickness of ~ 59 Å, which decreased to ~ 45 Å as the heat treatment temperature was increased to 240 ºC (Figure 3-1a). The top circular aluminum electrodes were thermally evaporated onto the surface of the heat treated multilayers to a thickness of 1000 Å with a diameter of 1.5 mm. The breakdown tests were conducted under ambient conditions with the application of the probe tips to the top and bottom electrodes. The voltage between the electrodes was then increased until either the resistance of the instrument (100 kΩ), or an open circuit, was obtained. The breakdown strengths of each device was determined by dividing the applied voltage at which breakdown occurs by the thickness of the

insulating layer. As shown in the graph of Figure 3-1, the breakdown strengths of these devices increased dramatically with an increase in the heat treatment temperature from 140 ºC to 160 ºC. Similar heat treatment temperatures were demonstrated in Chapter 2 to initiate a sudden increase in the degree of crosslinking in these PAH/PAA multilayers. Although higher breakdown strengths were observed with the samples heat treated at 160 ºC and 180 ºC, the breakdown measurements appeared to be more precise and have an increasing trend with heat treatment at temperatures from 200 °C to 240 °C. These results suggest the dielectric strength of the PAH/PAA multilayer films was dependent upon their degree of crosslinking.
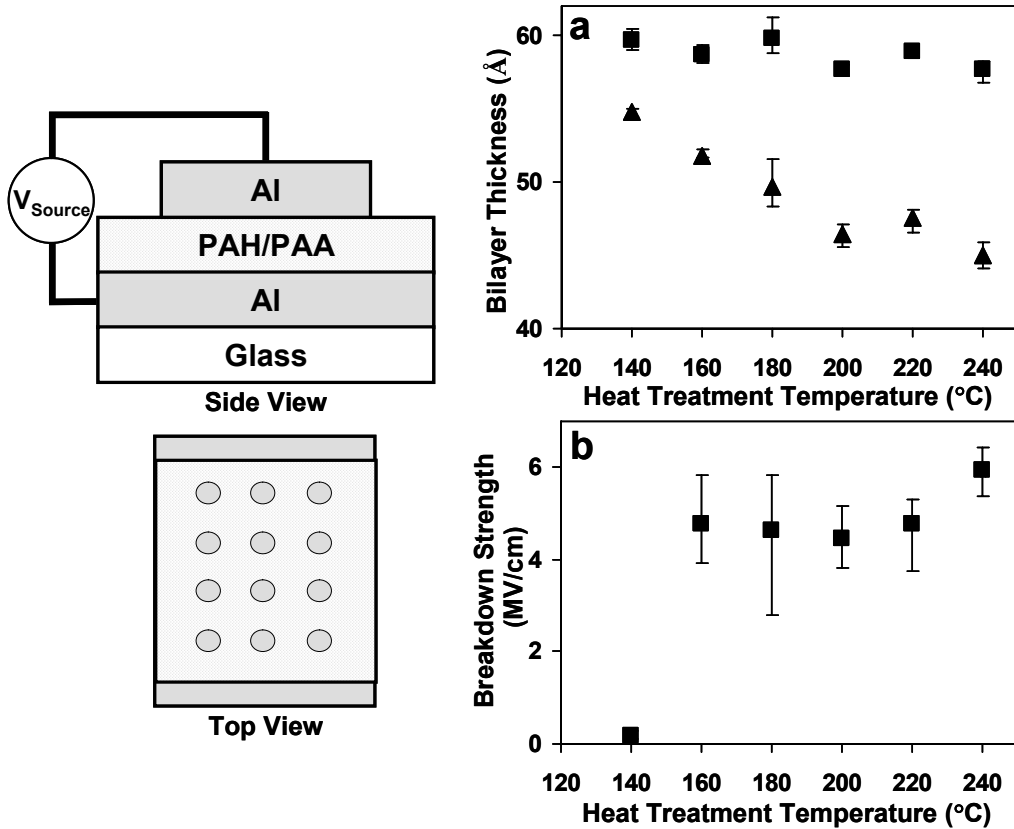
Figure 3-1. Schematic diagram illustrating the device architecture used to test the breakdown strength of insulating layers that contained 40 PAH/PAA bilayers and were heat treated at different temperatures. a) PAH/PAA bilayer thickness, before and after heat treatment, as a function of heat treatment temperature. b) The results from the breakdown tests are depicted in the graph as a function of heat treatment temperature.

A micromanipulator was also used under a microscope for the breakdown testing of these devices as a means to prevent the probe tip from puncturing through the thin films and to enable visual observation of the breakdown. A thin gold wire (diameter = 0.01 mm) was lowered at small increments to make contact with the top electrode and a tungsten probe tip was used to puncture through to the bottom aluminum electrode. As the voltage between the electrodes was increased, localized breakdown events occurred randomly throughout the capacitor. The events could also be heard with popping sounds and seen in the dark with flashes of light. This effect has previously been observed with other thin insulating layers in capacitors and is commonly described as being a localized self-healing event.[102,106,107] With enough charge build-up, a discharge event is suspected to occur at weak points in the device which results in the combustion of material down to the glass substrate.[106] In addition, the resulting increase in pressure causes the removal of the top aluminum electrode in the near vicinity, which leads to its isolation from the rest of the device. The effects of these breakdown events is illustrated in Figures 3-2a and 3-2b with images of a sample with 20 PAH/PAA bilayers (heat treated at 260 ºC) after it was tested for breakdown. A schematic illustration of a clearing site is included in the inset of Figure 3-2a. The energy discharge was also evident with the coinciding surges in current as observed with the spikes in the $I - V$ characteristics shown in Figure 3-2c. The overall leakage current initially increased at an exponential rate as the voltage was increased, but then leveled off, and decreased slightly, before critical breakdown at 70 V (~ 4.4 MV/cm). This breakdown occurred when either a clearing site formed under the gold probe tip or with the removal of the bottom aluminum electrode near the other probe tip.
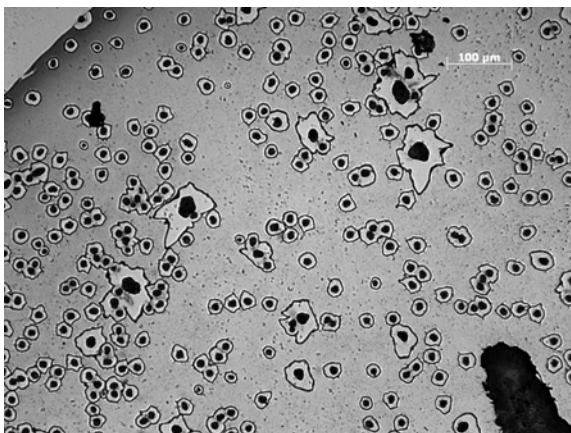
Figure 3-2. Image of the surface of a capacitor with 20 PAH/PAA bilayers (thickness = 1600 Å) as the insulating layer at a) 100x magnification and b)10x magnification. The schematic diagram contained in the inset of image (a) illustrates the clearing effect that was observed upon an increase in voltage across the dielectric material. c) *I – V* characterstics of the sample during testing.

3.3.2 Capacitor with Overlapping Perpendicular Electrode Architecture

The device architecture was modified to the arrangement illustrated in Figure 3-3 in an attempt to eliminate premature ending of the breakdown test due to the occurrence of localized clearing events directly under the probe tip. The bottom electrodes were patterned into strips along the glass slide and deposited to a thickness of 350 Å. After the deposition and heat treatment of the PAH/PAA multilayers, the top electrodes were evaporated as perpendicular strips with a similar thickness. The connections to the electrodes were made at the edges of the device and the site of overlap of the electrodes acted as the stacked capacitor.
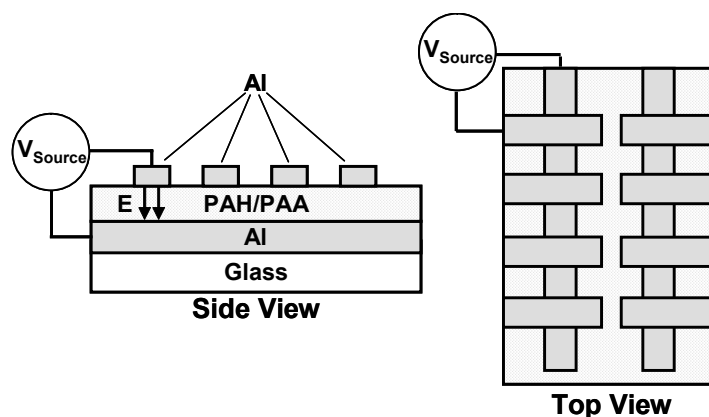
Figure 3-3. Schematic diagram illustrating the perpendicular arrangement of the overlaying electrodes.

3.3.2.1 Breakdown strength as a function of heat treatment temperature

Several capacitors were fabricated with 40 PAH/PAA bilayers using this device architecture and were heat treated at different temperatures before evaporation of the top electrode. The dimensions of the overlapping area between the top and bottom electrodes were approximately 1.9 mm by 3.8 mm. Similar procedures were used for the breakdown tests of these samples, but the probe tips were connected to the electrodes at points away from the capacitor to avoid probe tip effects. The applicability of this device architecture was demonstrated using these multilayer films with minimal influence at the edges of the overlap on the breakdown of at high voltages. The breakdown strengths of the devices were determined by dividing the breakdown voltage by the dielectric layer thickness. The method used to identify the breakdown voltage will be discussed later. The results from these tests are shown in Figure 3-4a and 3-4b as a function of the heat treatment temperature. The breakdown strengths for the device with no heat treatment (HT) and the one heat treated at 140 ºC were higher than what was measured using the other more traditional testing technique. A similar improvement in breakdown strength was observed with an additional increase in heat treatment temperature to 180 ºC. As the heat treatment temperature was raised further, the breakdown strength of these capacitors continued a more

gradual increase. This improvement in strength was a result of both the higher breakdown voltage and the decrease in thickness of the insulating layer, as shown in Figure 3-4b. These characteristics were both observed with a slightly more dramatic effect as the heat treatment temperature was increased from 140 ºC to 180 ºC. The real component of the dielectric constant of these PAH/PAA multilayers also decreased as the heat treatment temperature was increased (Figure 3-4a), which has previously been attributed to the formation of amide crosslinks.[105] The results suggest the dielectric strength of these films is dependent upon the crosslink density.
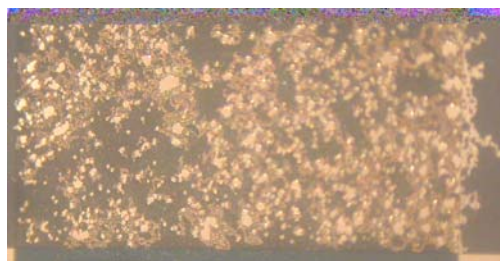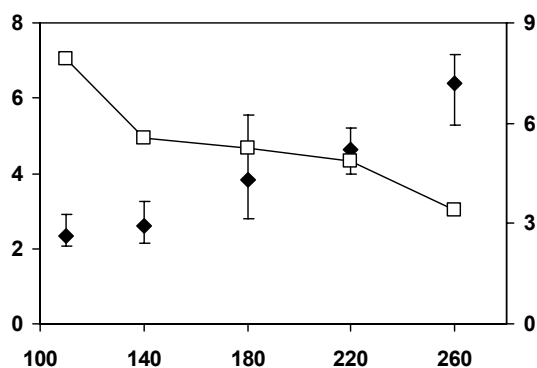
Figure 3-4. a) The breakdown strength and dielectric constant of devices with the overlapping architecture and 40 PAH/PAA bilayers are presented as a function of heat treatment temperature. b) The breakdown voltage and bilayer thickness of the PAH/PAA multilayer films as a function of heat treatment temperature. The images below are of the devices after testing.

The appearance of the samples after testing also indicated a difference in breakdown when the dielectric was heat treated at different temperatures. Images of these samples after breakdown are shown in Figure 3-4. The multilayer film that was not heat treated had an instantaneous breakdown that resulted in a global deformation of the stacked layers. The inset within its image is at a higher magnification and illustrates how a localized breakdown event led to the formation of creases in its vicinity. This effect observed throughout the film. The image of the sample heat treated at 140 ºC had a similar appearance after testing, but the physical damage appeared to be more localized. The transition in physical appearance of these samples after breakdown appeared to be more dramatic with a further increase in annealing temperature. For samples heat treated at 180 ºC and 220 ºC, the emergence of the clearing sites occurred at a slower rate with an increase in the applied voltage, and the physical damage was more localized. These characteristics coincided with the trend observed for the increase in crosslink density with heat treatment temperature. An increase in toughness of these films with crosslink density may limit the physical damage of a localized breakdown event, thereby preventing a catastrophic failure.

3.3.2.2 Breakdown strength as a function of dielectric thickness

The breakdown of heat treated PAH/PAA multilayers was investigated by studying the gradual appearance of clearing sites as a function of maximum applied voltage. The results in Figure 3-5 were obtained with the breakdown testing of a device with 10 PAH/PAA bilayers that was heat treated at 260 ºC (thickness = 750 Å). The dimensions of the overlapping area between the top and bottom electrodes were approximately 2.0 mm by 2.4 mm. The capacitance and dissipation factor (tan δ = $\varepsilon''/\varepsilon'$) of this device was measured after sequential tests to higher

voltages until a connection was lost due to excessive damage. Before breakdown occurs, only a minimal change was observed with the dissipation factor and the capacitance decreased by only a small amount when the maximum testing voltage was increased above 30 V. The small decrease in capacitance (12.5%) was attributed to the loss in the effective area of the top. A large degree of clearing is shown in Figure 3-5 after sequential testing to higher maximum voltages. A catastrophic failure was observed with the testing of this device as a sudden decrease in capacitance and excessive damage occurred at a voltage of 44 V (~ 5.9 MV/cm). The pattern observed with the formation of clearing sites in these images was often noticed during the testing of these types of devices and is believed to be caused by the presence of dust particles.
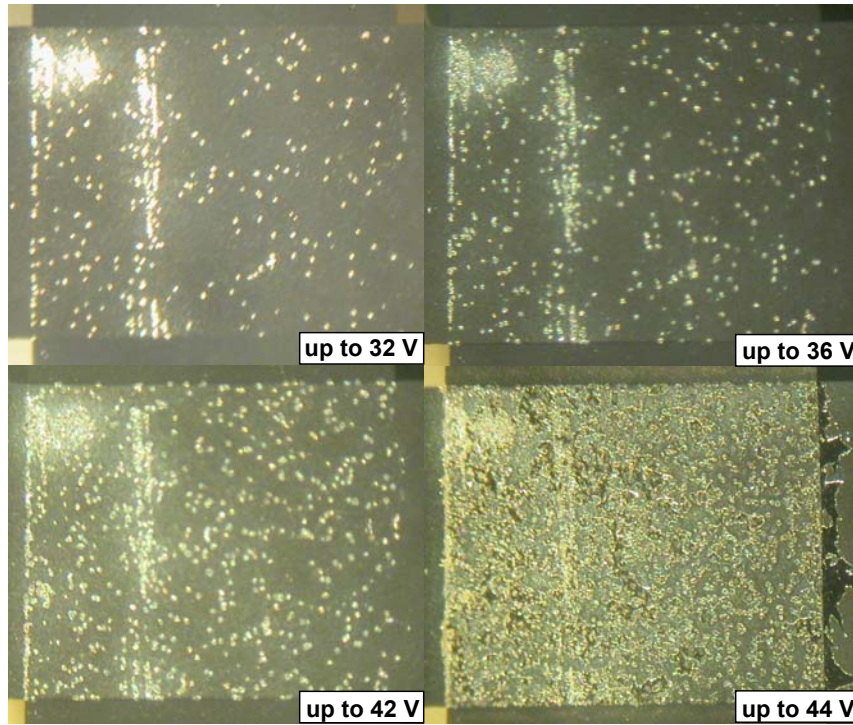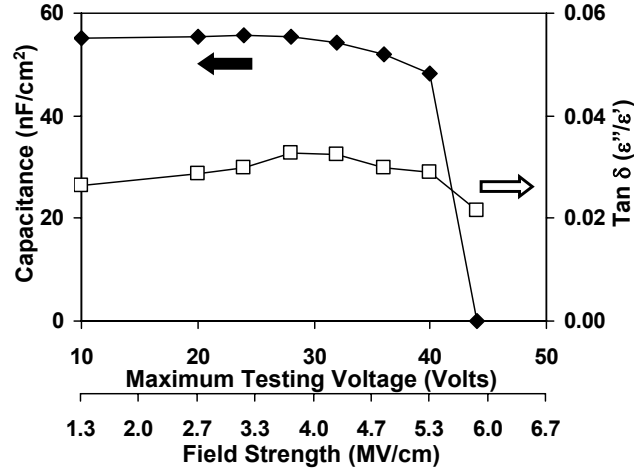
Figure 3-5. The capacitance and dissipation factor of a heat treated device (260 °C) with 10 PAH/PAA bilayers (pH = 3.5) after sequential breakdown tests to higher voltages. The images illustrate the degree of clearing present after testing to higher voltages.

A device with 40 PAH/PAA bilayers (thickness = 4010 Å) as the insulating layer was also heat treated at 260 °C and tested for breakdown in the same manner. Representative $I – V$ characteristics are shown in Figure 3-6a, which were obtained with an initial breakdown test to 120 V and a subsequent increase by 20 V for each following test. Large variations in the current and several clearing events were observed at relatively low voltages during the first test. These

effects were reduced in the following tests as observed with the more stabilized increase in current with voltage and the higher field strengths needed to reinitiate the formation of clearing sites. Applying a bias below the breakdown limit is commonly used in manufacturing to pre-clear metallized polymer film capacitors.[106] In order to monitor the performance of the capacitor, the dielectric properties were obtained after each sequential test. As shown in Figure 3-6b as a function of test number, the capacitance and dissipation factor of the device appeared to decrease much more with each additional test than was observed during the testing of the capacitor with 10 PAH/PAA bilayers (Figure 3-5). Additionally, the sizes of the clearing sites were significantly larger for this device after testing, as shown with the images in Figure 3-6. This increase in size of the clearing sites was due to higher discharge energy at higher voltages and explains why there was a larger decrease in capacitance (32%) before catastrophic breakdown. The discharge energy of a clearing event has been shown to have a linear relationship with the capacitance, but a fifth power dependence on the voltage.[107] Breakdown of this device finally occurred with a second test to 300 V, which was due to disconnection of the device at the edge.
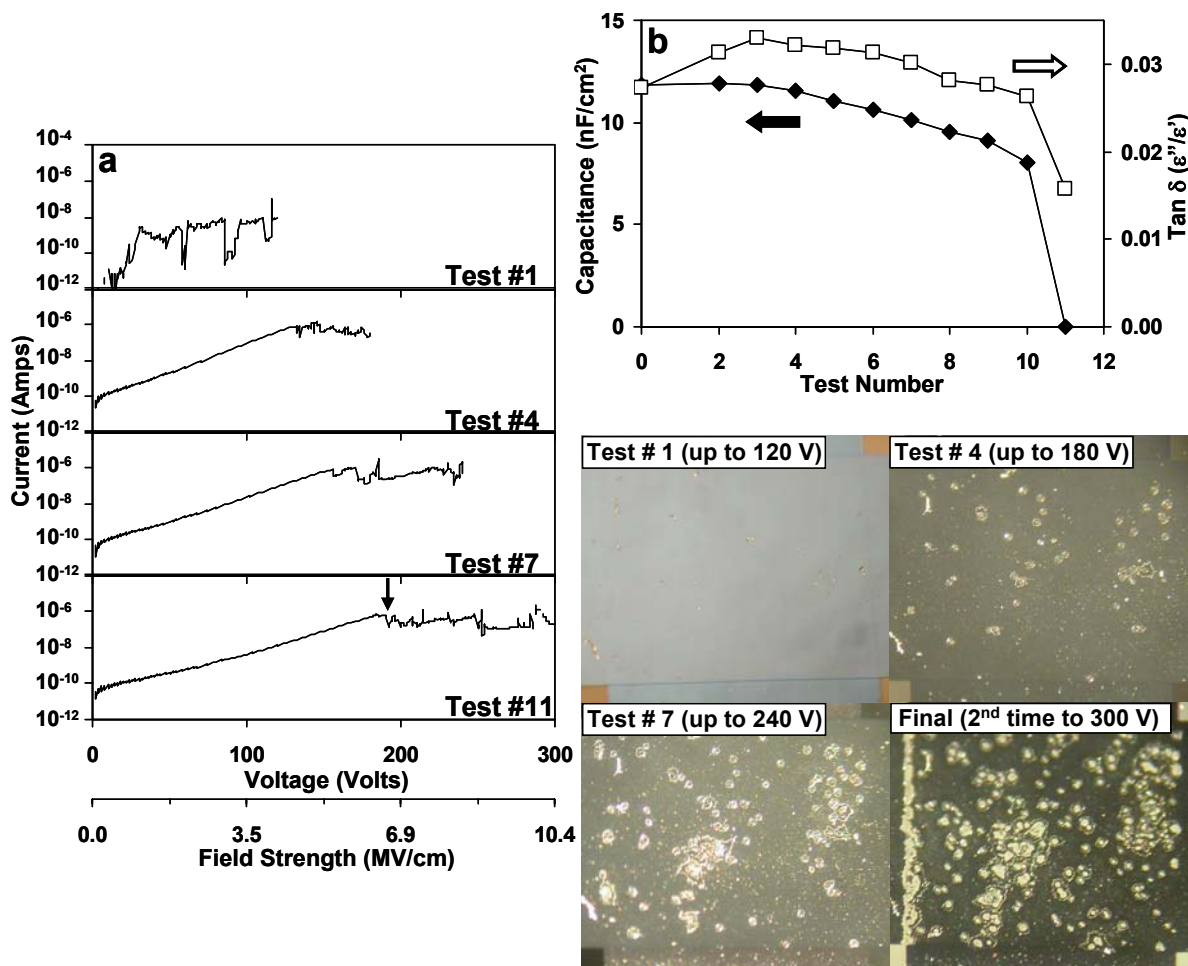
Figure 3-6. a) *I – V* characteristics obtained during the sequential breakdown testing of a device at higher maximum applied voltages. A heat treated (260 ºC) multilayer film with 40 PAH/PAA bilayers (pH = 3.5) was used as the insulating layer. b) The capacitance and dissipation factor of the device after testing to a higher applied voltage. The images illustrate the degree of clearing present after testing to these higher voltages.

The connection to the aluminum electrodes was commonly lost at high voltages due to damage of the metal from the high discharge energy of the clearing events.[107] This effect was observed with devices with thicker insulating layers (approximately > 1000 Å), and appeared to coincide with the disruption of the smooth increase in current with voltage, as shown with the *I – V* characteristics in Figure 3-6a. Therefore, the preclearing technique was used to investigate the dielectric strength of these crosslinked multilayer films. The devices were tested numerous times at higher voltages and the dielectric properties were measured to ensure a connection was

reestablished. A breakdown voltage was then identified with the highest obtainable voltage while still maintaining a connection, as is demonstrated in Figure 3-6a with the arrow in test number 11.

Several devices with a controlled range of dielectric layer thicknesses were tested for breakdown at high voltages. A linear increase in thickness of the insulating layer was obtained by increasing the number of PAH/PAA bilayers with the conditions shown in Figure 3-7. The thicknesses of the crosslinked multilayer films ranged from 750 Å to 4010 Å. The results from the breakdown testing of these devices are shown in Figure 3-7. Although a linear increase in breakdown voltage was observed with a higher number of PAH/PAA bilayers, the breakdown strength (6.6 MV/cm) did appear to decrease slightly with thickness. Assuming a consistent crosslink density throughout the film, these results suggest that thickness does have a subtle effect on the breakdown mechanism.
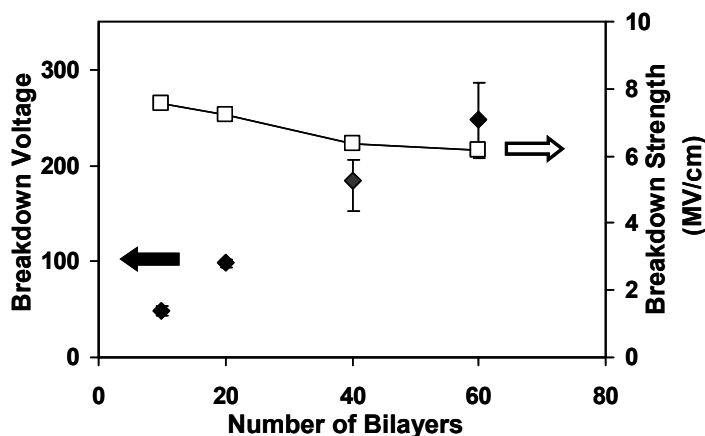
Figure 3-7. Breakdown characteristics of devices with an increasing number of PAH/PAA bilayers (pH = 3.5) as the dielectric layer. The films were heat treated at 260 ºC with a final bilayer thickness ~ 70 Å.

A similar study was also used to investigate the dielectric of crosslinked PAH/PAA multilayers deposited from solutions with a different pH. The results in Figure 3-8 were obtained with the breakdown testing of devices with dielectric layers deposited at a pH of 6.0. The dimensions of the overlapping area between the top and bottom electrodes were either 2.0

mm by 2.4 mm or 1.9 mm by 3.8 mm. As discussed in the previous chapter, the deposition of PAH/PAA multilayers under these conditions results in extended polyelectrolyte configurations and a higher crosslink density with heat treatment. The average film thicknesses of these insulating layers after heat treatment (260 °C) ranged from approximately 90 to 540 Å with an increase in the number of bilayers from 20 to 80. The dielectric measurements of a device with 80 PAH/PAA bilayers were obtained with the sequential testing to higher applied voltages. As shown in Figure 3-8a, the device appeared to maintain a steady capacitance (decreased 16%) and dissipation factor until a significant degree of clearing occurred before breakdown at 44 V (~ 7.5 MV/cm). The breakdown strength measurements for devices fabricated at a pH of 6.0 are shown in Figure 3-8b as a function of the number of bilayers. The breakdown of these devices occurred at higher voltages as the film thickness was increased, but a trend could not be distinguished for the breakdown strength (~ 6.8 MV/cm).

Although a dependence of breakdown strength on the film thickness was not apparent for the devices with PAH/PAA deposited at a pH of 6.0, a difference was observed in their appearance during breakdown. The images in Figure 3-8 are representative illustrations of samples after testing with a different number of bilayers. An almost completely uniform transformation in physical appearance was observed for the breakdown of each device. For the device with 80 PAH/PAA bilayers as the dielectric layer, a high density of small clearing sites (diameter ~ 10 - 15 µm) formed before catastrophic breakdown. The size of these clearing sites was consistent with a decrease in dielectric layer thickness, and therefore lower discharge energy, from the samples fabricated at a pH of 3.5. For samples with 60 PAH/PAA bilayers, the clearing sites were smaller (diameter ~ 1 - 7 µm), and were not always visibly apparent. A transition in the breakdown mechanism appeared to occur at this range of dielectric layer

thickness as two regions with a different physical appearance appeared during breakdown. This new region had a white semi-transparent appearance, which predominates in the images of the broken down samples fabricated with 20 and 40 PAH/PAA bilayers. During the breakdown of these devices, a gradual transition in appearance occurred and the thickness of the capacitor increased by over 1000 Å. This transition may be due to a different breakdown mechanism, such as an electrochemical reaction with the aluminum electrode or due to a significant increase in surface roughness caused by a high density of sub-microscopic clearing sites.
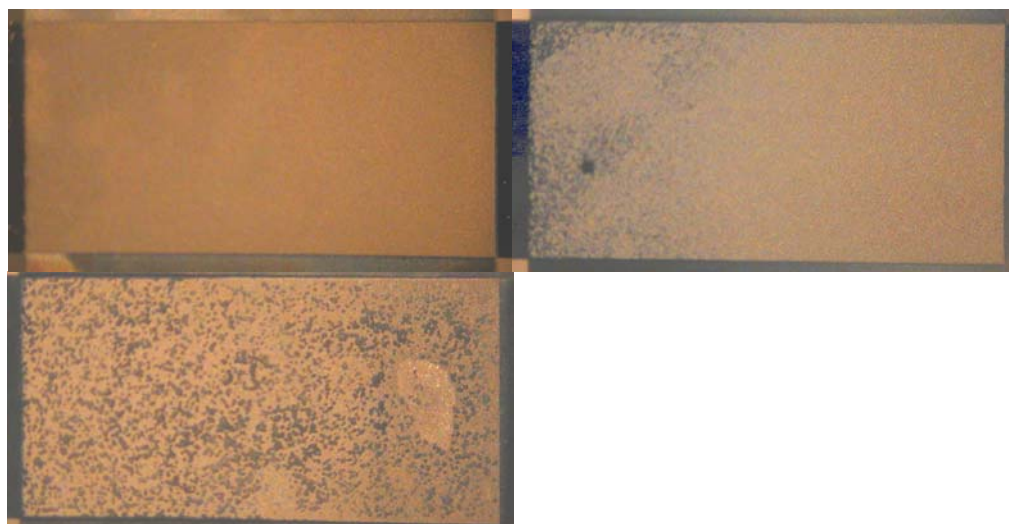
Figure 3-8. a) The dielectric properties of a device with 80 PAH/PAA bilayers (BL) deposited as the insulating layer after sequential testing to higher applied voltages. The multilayer films were deposited from solutions with a pH of 6.0 and then heat treated at 260 ºC with a resulting bilayer thickness ~ 4 - 7 Å. b) Breakdown characteristics of devices with an increasing number of PAH/PAA bilayers. The images below are of the devices with an indicated number of bilayers that were previously tested for breakdown.

Several different devices were fabricated with crosslinked PAH/PAA multilayers deposited at different pH conditions and tested for breakdown as a means to investigate the dependence of the dielectric strength on the polylelectrolyte configuration. Capacitors were fabricated using polyelectrolyte solutions at a pH of 2.1 and 4.0, in addition to the devices already discussed above. The appearance of these devices during breakdown was similar to that observed with the devices deposited at a pH of 3.5. The average breakdown strengths and PAH/PAA bilayer thicknesses for all the devices (including those deposited at a pH of 3.5 and 6.0) are listed in Table 3-1. A gradual increase in breakdown strength from 6.0 to 7.4 MV cm^{-1} was observed for these devices as a function of the pH conditions used during film deposition. The gradual increase in breakdown strength with pH does not appear to have a strong correlation with either the polymer configuration or the crosslink density since they have a more dramatic dependence on the pH of the polyelectrolyte solutions used during film deposition. The bilayer thickness of the PAH/PAA multilayers has been shown to increase slowly with pH at the low end, but transitions to much higher and then to a much lower value as the pH is increased from 4.0 to 6.0. The degree of crosslinking increases at a rapid rate with an increase in pH, but reaches a plateau near pH = 6.0, as discussed in Chapter 2. The gradual increase in breakdown strength of heat treated devices with pH and its sudden increase with the initial formation of amide crosslinks suggests that a certain amount of crosslinking physically toughens the film, thereby localizing the clearing effect. A continued increase in crosslink density then has a more gradual effect on improving the intrinsic resistance to high voltages, as was shown with an increase in both the heat treatment temperature and the pH used for film deposition.

Table 3-1. A comparison of breakdown strengths for devices fabricated with crosslinked multilayer films (heat treated at 260 °C) deposited at different pH conditions. (a), (b), and (c) are measurements obtained from the studies in Figures 3-4, 3-7, and 3-8, respectively.

	pH = 2.1	pH = 3.5 (a)	pH = 3.5 (b)	pH = 4.0	pH = 6.0 (c)
Dielectric Strength (MV/cm)	6.0	4.9	6.4	7.4	7.4
# of Bilayers	34	40	40	20	80
Bilayer Thickness (Å)	34	61	72	83	6.8

3.3.3 Tertiary Amide Crosslinking with Linear Poly(ethylenimine) (PEI)

The layer-by-layer deposition and heat treatment of PEI/PAA multilayer films were used as a method to investigate the influence of tertiary amide crosslinks on the dielectric strength of multilayer films. A small degree of crosslinking (14%) was shown in Chapter 2 to occur within these films when heat treated at 260 ºC under a vacuum. Several devices were fabricated with insulating layers containing an increasing number of PEI/PAA bilayers. The dimensions of the overlapping area between the top and bottom electrodes were 1.9 mm by 3.8 mm. The breakdown characteristics of these devices at high voltages are shown in Figure 3-9 with an increase in the number of bilayers from 20 to 60 (thickness range ~ 700 to 2400 Å). The breakdown voltage increased with a higher number of PEI/PAA bilayers, but the breakdown strength decreased from 9.1 MV/cm to 7.1 MV/cm. Overall, a higher dielectric strength was found for these films than that measured for crosslinked PAH/PAA multilayers with similar thicknesses. This improvement in dielectric strength may be attributed to the elimination of proton hopping with the formation tertiary amide crosslinks instead secondary amide crosslinks. The decrease in breakdown strength with an increase in dielectric layer thickness may be due to damage of the electrode contacts caused by the large discharge energies at higher applied voltages. Additional studies are ongoing to continue investigation of these subtle effects at lower dielectric layer thicknesses and verify the improvement in dielectric strength with the incorporation of tertiary amide crosslinks.
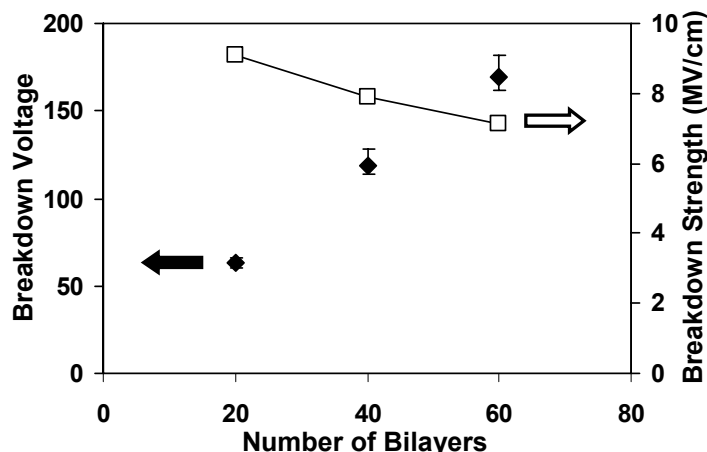
Figure 3-9. Breakdown characteristics of devices with an increasing number of crosslinked PEI/PAA bilayers. The multilayers films were deposited from solutions with a pH of 2.2/2.7 and then heat treated at 260 ºC with a resulting bilayer thickness ~ 35 - 40 Å.

3.4 Conclusion

Several testing techniques were applied to investigate the breakdown characteristics of heat treated polyelectrolyte multilayer films. The dielectric strength of PAH/PAA multilayer films was shown to increase with heat treatment temperature as secondary amide crosslinks were formed. This trend was observed by using traditional breakdown testing methods and by testing devices with a modified architecture of overlapping perpendicular electrodes. The inclusion of the crosslinked multilayer films into this device architecture also demonstrated the capability to use these materials as ultra-thin insulating layers without significant breakdown at the edges of overlap. A high density of localized clearing events was observed randomly throughout each device, but their effect on device performance was minimal until catastrophic breakdown occurred. This point of failure was used as a means to define the maximum breakdown strength and enabled characterization of these materials as a function of film thickness, polymer configuration, and crosslink density. The most significant improvement in dielectric strength was observed with the initial introduction of crosslinks between 140 °C and 180 °C, which

appeared to limit the physical damage caused by localized breakdown events. A further increase in crosslink density of the film with higher heat treatment temperatures resulted in a more subtle increase in dielectric strength. A similar effect was observed with an increase in crosslink density of films deposited at higher pH conditions, which suggested the breakdown did not depend on the polymer configurations. High breakdown strengths were observed with the formation of these amide crosslinks, but even higher levels were reached with the formation of the tertiary amide crosslinks in heat treated PEI/PAA multilayer films. The dielectric properties and deposition characteristics of these layer-by-layer assembled multilayer films are desirable for electronic applications requiring thin, but robust insulating layers.

3.5 References

102. Rabuffi, M.; Picci, G. *IEEE Trans. on Plasma Science* **2002**, *30*, 1939.

103. Rose, M. F. IEEE AES Magazine, November 1989.

104. Pavoor, P. V.; Gearing, B. P.; Bellare, A.; Cohen, R. E. *Wear* **2004**, *256*, 1196.

105. Durstock, M. F. Ph. D. Thesis, Department of Materials Science and Engineering, Massachusetts Institute of Technology, Cambridge, 1999.

106. Reed, C. W.; Cichanowski, S. W. *IEEE Trans. of Dielectrics and Electrical Insulation* **1994**, *1*, 904.

107. Walgenwitz, B.; Tortai, J.-H.; Bonifaci, N.; Denat, A.; 2004 Inter. Conf. on Solid Dielectrics, Toulouse, France, July 5-9, 2004.

Chapter 4

An Ultra-thin Gate Dielectric for Organic Field Effect Transistors

Using Layer-by-Layer Assembly

4.1 Introductory Remarks

Organic field effect transistors (OFETs) have received considerable attention as a low-cost, light-weight, flexible alternative to traditional amorphous silicon devices in a variety of applications.[108,109,110,111] Some specific examples include large area flat-panel displays, sensor arrays, and smart cards. Previous studies have investigated the use of a variety of semiconducting organic materials for the active layer in various transistor architectures. Since these devices operate primarily in the accumulation mode, they require well ordered and chemically undoped materials to obtain high charge carrier mobilities and large $I_{on/off}$ ratios, respectively.

The application of organic materials as the dielectric layer in OFET devices has recently received significant attention due to their compatability, processability, and tailorability.[112,113,114] The incorporation of different types of dielectric layers into the device architecture also effects the performance of the transistor. The thickness and dielectric constant of these insulating layers determines the effective capacitance across the dielectric, thereby influencing the number of charge carriers induced in the active layer with an applied voltage. While a dielectric layer thickness as low as 25 Å has been demonstrated with self-assembled monolayers,[115] film thicknesses are generally limited to more than an order of magnitude higher because of pinhole formations at thinner dimensions. A higher dielectric constant has a similar impact on the capacitance, but has been shown to result in a low field effect mobility of the semiconducting

active layer. The dipolar interactions at the interface are believed to cause energetic disorder and a change in morphology of the semiconducting material, thereby leading to a higher degree of trapping of charge carriers.[116] As a result, a multilayer film structure with a high-ε internal component and a low-ε external component has been suggested as being the ideal dielectric to obtain low operating voltages while limiting charge trapping.[116]

The layer-by-layer (LbL) assembly of polyelectrolytes was investigated as a method to incorporate ultra-thin multilayered films as the dielectric layer into OFETs. In particular, crosslinked poly(allylamine hydrochloride)/poly(acrylic acid) (PAH/PAA) multilayers were used as the dielectric material for devices with poly(3-hexylthiophene-2,5-diyl) (P3HT) as the active layer. A field effect was demonstrated using this dielectric material as a negative applied voltage between the gate and source electrodes increased the conductivity of the P3HT active layer. The performance characteristics of these devices are presented with an analysis of the operating voltage, $I_{on/off}$ ratio, field effect mobility, and leakage current as a function of dielectric thickness.

4.2 Experimental

The polymers, poly(acrylic acid) (M_w = 90,000) and poly(allylamine hydrochloride) (M_w = 60,000), and linear poly(ethylenimine) (M_w = 25,000), were purchased from Polysciences, Inc. Polyelectrolyte solutions (10 mM) were pH adjusted with NaOH and HCl using an Orion model 230A pH meter. Each monolayer deposition cycle (~ 15 min) was followed with multiple rinse steps in deionized (18 MΩ·cm) H_2O in a Carl Zeiss Microm DS-50 automatic slide stainer. A multi-step process involving 15 min sonification steps in water, 1,1,1-trichloroethane, acetone, and methanol and 15 min in a Harrick PDC – 236 plasma cleaner was used to the clean glass slides. The bottom aluminum electrode was thermally evaporated at a rate of 4 – 5 Å/s to a

thickness of 350 Å in an Explorer 18 Denton Vacuum system ($< 10^{-7}$ Torr) using a Telemark model 860 deposition controller. Film thicknesses were measured with a Tencor P-10 surface profiler at a stylus force of 0.6 mg. The multilayer films were heated at 85 ºC under $N_2(g)$ for 1 hour and then at 260 ºC under vacuum for approximately 5 – 6 hours. Capacitance and dielectric constant measurements were obtained using a Novocontrol broadband dielectric spectrometer. Further device fabrication and testing was carried out by James Swensen at the University of California at Santa Barbara. The samples were heated under an inert environment to 120 °C for 30 min to remove moisture. Highly regioregular poly(3-hexylthiophene-2,5-diyl) was purchased from Rieke Metals. P3HT was spincoated from toluene (~ 50 mM) onto crosslinked PAH/PAA multilayers. Gold was thermally evaporated as the source and drain electrodes onto the P3HT active layer using a shadow mask at a rate of 0.5 Å /s. The channel lengths were 15 μm and the widths ranged from 500 – 1500 μm. The devices were tested in a dry box under $N_2(g)$ using a Kiethley 4200 Semiconductor Characterization System.[®] Voltages were applied to the drain and gate electrodes with the source electrode acting as the common ground.

4.3 Results and Discussion

A schematic representation of the OFET device architecture used in this study is provided in Figure 1. PAH/PAA multilayer films were deposited onto an aluminum gate electrode through layer-by-layer (LbL) assembly to obtain a gate dielectric of controllable thickness. The films were then heat-treated to covalently crosslink the multilayer films to improve their stability, resistivity, and dielectric strength.[117,118] After spin-coating a P3HT layer directly onto the assembled dielectric layer, gold source and drain electrodes were evaporated onto opposite sides of the active channel to complete the device.

1 mm

20 μm

Au Source (Ground)		Au Drain (V_{DS})
Poly(3-hexylthiophene)		
PAH/PAA		
Al Gate (V_G)		

500 – 1500 μm
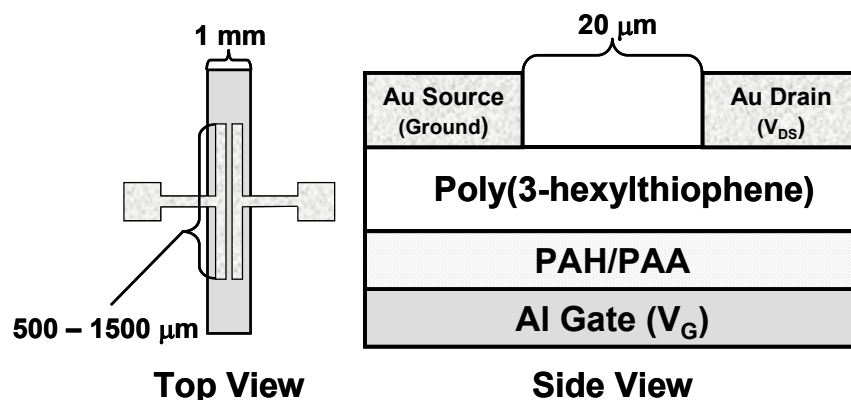
Top View   **Side View**

Figure 4-1. Schematic illustration of the device architecture used with P3HT as the active layer and PAH/PAA multilayers as the gate dielectric. The side view demonstrates the stacked architecture of the device and top view indicates the orientation of the Au and Al electrodes.

Representative output characteristics are shown in Figure 4-2a for an OFET with a gate dielectric comprised of 10 PAH/PAA bilayers deposited at a pH of 3.5. The total thickness of the gate dielectric was approximately 650 Å, which corresponds to an individual bilayer thickness of about 65 Å, consistent with that reported by Shiratori *et al* and the results in Chapter 2.[119] The capacitance per unit area (C_i) for this dielectric layer was approximately 47 nF cm^{-2}, which was based on its film thickness and the capacitance measurements from Chapter 3. As a negative voltage (V_G) was applied between the gate and source electrodes, the conductivity of the semiconducting P3HT layer appeared to increase. This field effect is demonstrated in Figure 4-2a, as the application of V_G at higher magnitudes induces higher levels of I_{DS} for similar ranges of V_{DS}. As V_{DS} is increased past V_G, I_{DS} saturates due to the potential drop and corresponding depletion of charge build-up near the drain electrode. At a V_G of 5.5, an $I_{on/off}$ ratio of ~ 60 was obtained in the saturated region. A notable shift of I_{DS} below the origin at $V_{DS} = 0$ V was also observed at this gate voltage. This increase in I_{DS} to a positive value was attributed to a related effect with the leakage current (I_G) through the dielectric layer. As shown with the $I_G – V_{DS}$ characteristics in Figure 4-2b, the magnitude of leakage current at $V_{DS} = 0$ V increases significantly as V_G is changed from -4.4 to -5.5 V. As V_{DS} was increased when $V_G = 5.5$ V, I_G

initially decreased in magnitude, but then slowly increased in an unstable manner. Similar trends were observed with the $I_G - V_{DS}$ characteristics obtained at lower magnitudes of V_G, but with a continued, and more stable decrease in I_G at higher magnitudes of V_{DS}. Although a field effect was apparent with the operation of these devices, their performance was limited to lower voltages due the leakage current through the dielectric layer.
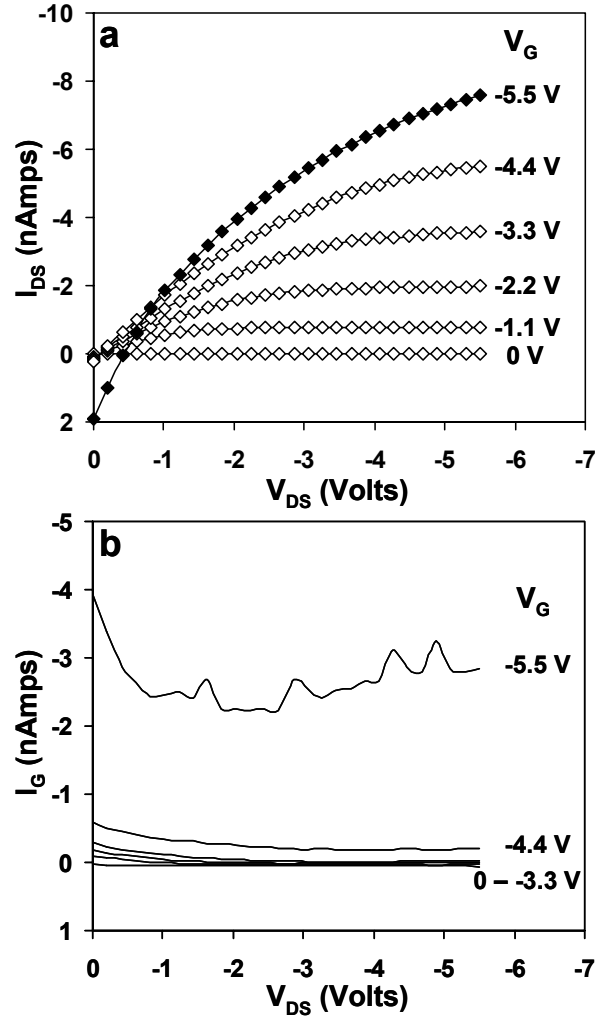
Figure 4-2. a) Output characteristics ($I_{DS} - V_{DS}$; I_{DS} and V_{DS} are the source-drain current and voltage, respectively) of an OFET with P3HT as the active layer and 10 PAH/PAA bilayers (deposited at a pH of 3.5) as the dielectric layer. b) Leakage currents for the tests in (a) as a function of the applied voltage between the source and drain electrodes.

The transfer characteristics of a similar device is shown in Figure 4-3a with I_{DS} and I_G as a function of V_G for the saturated region ($V_{DS} = 5.5$ V). The magnitude of I_{DS} increased with a

more negative gate bias, reaching similar values as was observed for the saturated region of the output characteristics for the device (same architecture) discussed in Figure 4-2. The gate bias was either increased or decreased for three more sequential tests and minimal hysteresis was observed in the I_{DS}, thereby indicating a low degree of charge carrier trapping at the interface. The $I_{on/off}$ ratio between the I_{DS} values at $V_G = 5.5$ V and $V_G = 0$ V was ~ 50, but was as high as 195 when the current at $V_G = 0.8$ V was used as the lower limit. The latter value of V_G corresponds with the threshold voltage (V_T) listed in Table 4.1, as determined by the linear fit of the $I_{DS}^{1/2} - V_G$ characteristics in Figure 4-2b. These characteristics indicate a low level of doping of the P3HT active layer, which is most likely caused by exposure to trace amounts of oxygen during fabrication. The field effect mobility ($\mu = 2.6$ x 10^{-4} cm^2 V^{-1} s^{-1}) was calculated from the slope of the linear fit and with the use of Equation 1.9 for the saturated regime. The mobility for this device was an order of magnitude lower than what has previously been demonstrated ($\mu \sim$ 3.2 x 10^{-3} cm^2 V^{-1} s^{-1}) for a P3HT active layer deposited from toluene.[120] The lower mobility was attributed to differences in fabrication of the active layer. Although a field effect mobility as high as 0.2 cm^2 V^{-1} s^{-1} has been demonstrated with the deposition of highly ordered P3HT from chloroform,[121] this solvent had limited wettability on the crosslinked PAH/PAA multilayer dielectric materials.

An exponential increase in the magnitude of I_G was observed as V_G approached -5.5 V (Figure 4-3a), which agrees with the output characteristics in Figure 4-2. This sudden increase in leakage current resembles the "super-ohmic" behavior discussed in Chapter 3 with a high voltage applied across the dielectric, but appears to occur here at a much lower field strength (E = 0.9 MV cm^{-1}). A higher magnitude of V_{DS} appears to minimize the effect of the gate bias until a significant degree of leakage current is obtained. These trends indicate a high level of interaction

between the gate and the drain electrodes. The large degree of leakage current through the gate dielectric most likely results in a loss of its capacitance, thereby limiting the $I_{on/off}$ ratio and field effect mobility.
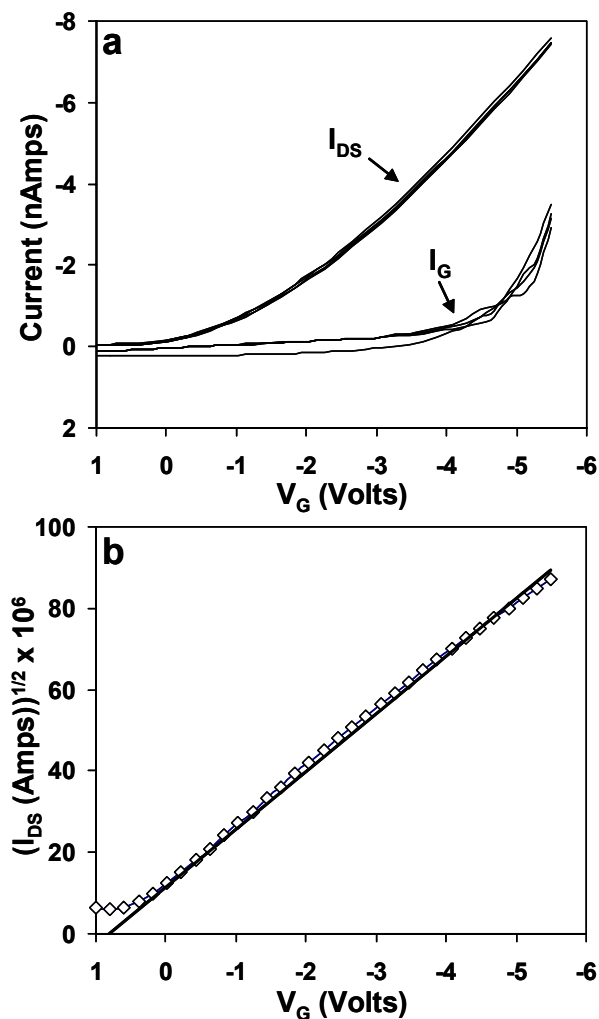
Figure 4-3. The transfer characteristics in the saturated regime (V_{DS} = -5.5 V) for a device with P3HT as the active layer and 10 PAH/PAA bilayers (deposited at a pH of 3.5) as the dielectric layer. a) The drain and leakage current as a function of voltage applied between the gate and source electrode. b) The $I_{DS}^{1/2}$ – V_G characteristics for the results in (a).

Similar devices were also fabricated with 20 and 40 PAH/PAA bilayers as a means to characterize the device performance as a function of dielectric layer thickness. The output and transfer characteristics that were obtained from these devices are presented in Appendix B. The testing parameters used for the characterization of devices with 10, 20, and 40 bilayers as the

gate dielectric layer, and the resulting performance measurements, are listed in Table 4-1. As the number of bilayers was increased for the dielectric layer, an almost linear increase in thickness was observed. The values of capacitance per area (C_i) for the thicker dielectric layers are listed in Table 4.1. It should be noted that an OFET was also fabricated with five PAH/PAA bilayers, but a field effect was not observed due to a significant amount of leakage current through the gate dielectric layer. This high degree of leakage may be attributed to pinholes present at lower multilayer film thicknesses, which may be related to the interactions between the first few bilayers and the Al substrate.[122]

The results in Table 4-1 are listed in a manner to compare the performance of devices with a different number of PAH/PAA bilayers. The values of the applied voltages, measured currents, and calculated performance characteristics ($I_{on/off}$ and mobility) are listed for each of the devices. The values for V_G and V_{DS} were increased by almost an order of magnitude without significant damage to the dielectric material as the number of bilayers was increased from 10 to 20. The increase in magnitude of the applied voltages for the device with 20 bilayers also resulted in an increase in field strength by a factor of 3, which was comparable to the dielectric strength measurements of these materials in Chapter 3 (5 – 6.5 MV cm^{-1}). As listed in Table 4.1, the $I_{on/off}$ ratio for the device with 20 PAH/PAA bilayers was lower than the highest value obtained for the device with 10 PAH/PAA bilayers when using similar magnitudes of V_{DS} and V_G. As the magnitudes of V_G and V_{DS} were increased to 40 V and 45 V, respectively, the $I_{on/off}$ ratio for the device with 20 PAH/PAA bilayers surpassed the highest one obtained for the device with 10 bilayers. Surprisingly, the $I_{on/off}$ ratio from the transfer characteristics of another 20 bilayer device was greater by almost a factor of three than that observed for the 10 bilayer device, which was attributed to a higher obtainable field strength.

Table 4-1. The testing parameters and performance characteristics for OFETs fabricated with dielectric layers comprised of crosslinked PAH/PAA multilayers. The PAH/PAA bilayers were deposited at a pH of 3.5 with a thickness of 63 – 72 Å.

10 Bilayers $t = 650$ Å $C_i = 47$ nF cm^{-2} W = 500 µm

Output Characteristics ($I_{DS} - V_{DS}$)

V_{DS} (V)	V_G (V)	E (MV/cm)	$I_{on/off}$	I_{DS} "on" (nAmps)	I_{DS} "off" (nAmps)	I_G "on" (nAmps) at V_{DS}	I_G "on" (nAmps) at $V_{DS} = 0$ V
-5.5	-5.5	0.9	57	-7.6	-0.13	-2.85	-3.93
-2.65	-3.3	0.5	23	-2.8	-0.12	-0.06	-0.29

Transfer Characteristics ($I_{DS} - V_G$)

V_{DS} (V)	V_G (V)	E (MV/cm)	$I_{on/off}$ at $V_G = 0$ V	$I_{on/off}$ at $V_G = V_T$	I_G "on" (nAmps)	Mobility x 10^{-4} (cm^2 V^{-1} s^{-1})	V_T (V)
-5.5	-5.5	0.9	50	195	-2.92	2.6	0.8

20 Bilayers $t = 1450$ Å $C_i = 20$ nF cm^{-2} W = 1500 µm

Output Characteristics ($I_{DS} - V_{DS}$)

V_{DS} (V)	V_G (V)	E (MV/cm)	$I_{on/off}$	I_{DS} "on" (nAmps)	I_{DS} "off" (nAmps)	I_G "on" (nAmps) at V_{DS}	I_G "on" (nAmps) at $V_{DS} = 0$ V
-45	-40	2.7	247	-41.7	-0.17	-3.18	-49.97
-6	-5	0.3	15	-0.3	-0.02	0.05	-0.14

Transfer Characteristics ($I_{DS} - V_G$)

V_{DS} (V)	V_G (V)	E (MV/cm)	$I_{on/off}$ at $V_G = 0$V	$I_{on/off}$ at $V_G = V_T$	I_G "on" (nAmps)	Mobility x 10^{-4} (cm^2 V^{-1} s^{-1})	V_T (V)
-45	-45	3.1	565	N/A	-4.7	0.79	-7.8

40 Bilayers $t = 2900$ Å $C_i = 10$ nF cm^{-2} W = 1000 µm

Output Characteristics ($I_{DS} - V_{DS}$)

V_{DS} (V)	V_G (V)	E (MV/cm)	$I_{on/off}$	I_{DS} "on" (nAmps)	I_{DS} "off" (nAmps)	I_G "on" (nAmps) at V_{DS}	I_G "on" (nAmps) at $V_{DS} = 0$ V
-60	-60	2.1	22	-86.9	-4.00	-1.34	-7.84
-46	-45	1.5	15	-56.4	-3.84	-0.61	-4.87

Transfer Characteristics ($I_{DS} - V_G$)

V_{DS} (V)	V_G (V)	E (MV/cm)	$I_{on/off}$ at $V_G = 0$ V	$I_{on/off}$ at $V_G = V_T$	I_G "on" (nAmps)	Mobility x 10^{-4} (cm^2 V^{-1} s^{-1})	V_T (V)
-60	-60	2.1	35	154	-2.41	0.60	13.2

"on" meaning when highest V_G was applied and "off" meaning when $V_G = 0$ V was applied

The $I_G - V_{DS}$ characteristics for the device containing 20 PAH/PAA bilayers as the dielectric layer were similar to those observed for the device with 10 bilayers. As shown with the I_G values in Table 4-1 for the highest "on" state (V_G = -40 V), the leakage current decreased as a higher magnitude of V_{DS} was applied. Although the leakage current was initially high for this device at V_{DS} = 0 V, it decreased with a higher source-drain voltage to a value similar to what was observed for the device with 10 PAH/PAA bilayers.

Slight differences were also observed in the threshold voltage and field effect mobility between devices as the dielectric layer was increased from 10 to 20 PAH/PAA bilayers. These values were determined from the transfer characteristics in the saturated region and are listed for each device in Table 4.1. A negative threshold voltage of -7.8 V was calculated from the linear fit of the $I_{DS}^{1/2} - V_G$ characteristics for the device with 20 PAH/PAA bilayers. This negative value implies a higher degree of trapping of charge carriers at the interface, which was also apparent with the increase in hysteresis observed between sequential tests of the transfer characteristics (see Appendix B). The field effect mobility was also calculated from the linear fit of the $I_{DS}^{1/2} - V_G$ characteristics and was more than a factor of three less than that obtained with the device with 10 PAH/PAA bilayers. While the lower V_T was caused by modified doping levels of the active layer, the decrease in μ may be due to a change in morphology at the interface between the active and dielectric layer as the dielectric layer thickness is increased. This field effect mobility trend needs to be investigated further at higher dielectric layer thicknesses and as a function of active layer morphology.

Similar trends with an increase in dielectric layer thickness were also observed for devices fabricated with 40 PAH/PAA bilayers. As shown in Table 4.1, the application of V_G and V_{DS} similar in magnitude to the maximum voltages used for the device with 20 PAH/PAA bilayers,

resulted in a lower field strength and $I_{on/off}$ ratio. Even when the magnitudes of V_G and V_{DS} were increased to 60 V, these values were still less due to the lower capacitance of the thicker dielectric layer. The highest $I_{on/off}$ ratio for the device with 40 bilayers was also lower than what was obtained for the device with 10 PAH/PAA bilayers. The high field strength (0.45 MV cm^{-1}) required to offset the positive V_T, or de-dope the active layer, for this device may have limited the attainable $I_{on/off}$ ratio. The field effect mobility for the 40 bilayer device was less, but decreased to a lesser extent (24%) from what was observed with the transition from 10 to 20 bilayers (70%).

OFETs were also fabricated with crosslinked PAH/PAA multilayers deposited at a pH of 6.0 with a resulting bilayer thickness of 4.5 – 7.5 Å. The resulting thickness for these multilayers is much lower due to the high degree of ionization of the polyelectrolytes.[123] This high linear charge density promotes a highly extended state for the polymers within the multilayer film. Devices were successfully fabricated with 20 and 40 bilayers, both of which had an observed field effect. Unfortunately, a significant amount of leakage current was observed for the device with 20 bilayers making the analysis too difficult to obtain quantifiable results. This limitation may indicate a lower limit of control of the dielectric layer thickness when using layer-by-layer assembly.

Table 4-2. The testing parameters and performance characteristics for OFETs fabricated with a dielectric layer comprised of crosslinked PAH/PAA multilayers. The PAH/PAA bilayers were deposited at a pH of 6.0 with a thickness of 4.5 – 5.0 Å.

40 Bilayers $t = 200$ Å $C_i = 155$ nF cm^{-2} $W = 500$ μm

Output Characteristics ($I_{DS} - V_{DS}$)

V_{DS} (V)	V_G (V)	E (MV/cm)	$I_{on/off}$	I_{DS} "on" (nAmps)	I_{DS} "off" (nAmps)	I_G "on" (nAmps) at V_{DS} = -2.5 V	I_G "on" (nAmps) at V_{DS} = 0 V
-2.5	-2.5	1.3	127	-3.6	-0.03	-0.04	-0.49

Transfer Characteristics ($I_{DS} - V_G$)

V_{DS} (V)	V_G (V)	E (MV/cm)	$I_{on/off}$ at V_G = 0 V	$I_{on/off}$ at V_G = V_T	I_G "on" (nAmps)	Mobility x 10^{-4} (cm^2 V^{-1} s^{-1})	V_T (V)
-2.5	-2.5	1.3	155	N/A	-0.47	4.14	-0.4

The parameters used to test OFETs with 40 PAH/PAA bilayers (pH = 6.0) and the corresponding results are listed in Table 4-2. These results were obtained from the output and transfer characteristics for this device found in Appendix B. The capacitance per area for this gate dielectric was also calculated based on its film thickness and measurements obtained from Chapter 3. The magnitudes of V_G and V_{DS} that were required to obtain similar $I_{on/off}$ ratios to those discussed in Table 4.1 were lower for this device due to its lower dielectric layer thickness. Although these $I_{on/off}$ ratios were not the highest ones obtained of all the devices, they are of the same magnitude. When the device with 10 PAH/PAA bilayers deposited at a pH of 3.5 was tested at similar magnitudes of V_G and V_{DS}, the $I_{on/Ioff}$ ratio was decreased by more than a factor of five. Additionally, the field effect mobility measured for the device with 40 PAH/PAA bilayers (pH = 6.0) was the highest of all the devices tested. These results demonstrate the capability of using LbL assembly to control the dielectric layer thickness in OFETs as a means to decrease the operating voltage. The change in device performance was attributed to an increase in capacitance of the dielectric layer, which was obtained by depositing a fewer number of bilayers or by depositing the polyelectrolytes with a highly extended configuration.

4.4 Conclusion

The layer-by-layer deposition technique was successfully demonstrated as a method to incorporate an ultra-thin gate dielectric into OFET architectures. This technique was used to decrease the dielectric layer thickness in a controlled manner, which was shown to decrease the operating voltage required to obtain high $I_{on/off}$ ratios. An increase the field effect mobility was also observed with a decrease in dielectric layer thickness, but additional efforts are required to investigate this trend. Although a low degree of hysteresis was observed for these devices, they tended to have a lower field effect mobility and $I_{on/off}$ ratio than has previously been demonstrated. These limitations were attributed to differences in the fabrication of the active layer and to a lower effective capacitance caused by high levels of leakage current through the dielectric layer. Furthermore, the LbL assembly technique is generally applicable to other organic transistor architectures.

4.5 References

1. Lu, J.; Pinto, N. J.; MacDiarmid, A. G. *J. Appl. Phys*. **2002**, *92*, 6033.

2. Lee, M. S.; Lee, S. B.; Lee, J. Y.; Kang, H. S.; Kang, H. S.; Joo, J.; Epstein, A. J. *Mol. Cryst. Liq. Cryst*. **2003**, *405*, 171.

110. Brown, A. R.; Jarrett, C. P.; de Leeuw, D. M.; Matters, M. *Synth. Met.* **1997**, *88*, 37.

111. Matters, M.; de Leeuw, D. M.; Vissenberg, M. J. C. M.; Hart, C. M.; Herwig, P. T.; Geuns, T.; Mutsaers, C. M. J.; Drury, C. J. *Optical Materials* **1999**, *12*, 189.

112. Peng, X.; Horowitz, G.; Fichou, D.; Garnier, F. *Appl. Phys. Lett.* **1990**, *57*, 2013.

113. Parashkov, R.; Becker, E.; Ginev, G.; Riedl, T.; Johannes, H.-H.; Kowalsky, W. *J. Appl. Phys.* **2004**, *95*, 1594.

114. Veres, J.; Ogier, S.; Lemming, S.; Cupertino, D.; Khaffaf, S. M; Lloyd, G. Proc. of SPIE, Vol. 5217, Organic Field Effect Transistors II, ed. Dimitrakopoulus, C. D.; Dodabalapur, A. Bellingham, WA 2003, 147.

115. Halik, M.; Klauk, H.; Zschieschang, U.; Schmid, G.; Dehm, C.; Schütz, M.; Maisch, S.; Effenberger, F.; Brunnbauer, M.; Stellacci, F. *Nature* **2004**, *431*, 963. Collet, J.; Tharaud, O.; Chapoton, A.; Vuillaume, D. *Appl. Phys. Lett.* **2000**, *76*, 1941.

116. Veres, J.; Ogier, S. D.; Leeming, S. W.; Cupertino, D. C.; Khaffaf, S. M. *Adv. Funct. Mater*. **2003**, *13*, 199.

117. Durstock, M. F.; Rubner, M. F. *Langmuir* **2001**, *17*, 7865.

118. Harris, J. J.; DeRose, P. M.; Bruening, M. L. *J. Am. Chem. Soc.* **1999**, *121*, 1978.

119. Shiratori, S. S.; Rubner, M. F. *Macromolecules* **2000**, *33*, 4213.

120. Bao, Z.; Dodabalapur, A.; Lovinger, A. J. *Appl. Phys. Lett*. **1996**, *69*, 4108.

121. Wang, G.; Swensen, J.; Moses, D.; Heeger, A. J. *J. Appl. Phys.* **2003**, *93*, 6137.

122. Kurth, D. G.; Volmer, D.; Klitzing, R. V. in *Multilayer Thin Films*; Decher, G.; Schlenoff,

J. B., Eds.; WILEY-VCH Verlag GmbH & Co.; Weinheim, 2003, Ch. 14.

123. Shiratori, S. S.; Rubner, M. F. *Macromolecules* **2000**, *33*, 4213.

Chapter 5

Layer-by-Layer Assembled Gate Dielectric for

Doped Organic Thin Film Transistors

5.1 Introductory Remarks

The operating mechanism of doped organic thin film transistors is still not completely understood, although it is generally believed that the observed field effect is related to ion motion under the applied field.[124] However, the nature of how this phenomenon effects a change in conductivity is still under consideration. Possibilities that have been suggested include the existence of a field-induced metal-insulator transition,[87] an electrochemical de-doping effect,[125] or a combination of both.[126] The former mechanism has been speculated for similar stacked TFTs architectures using PEDOT:PSS as the active layer, while the latter one is generally applicable to electrochemical transistors. Establishing the dependence of the device operation on the gate dielectric thickness may improve the understanding of the ion motion with an applied gate bias and help determine whether it is related to the electrochemical doping of the active layer.

The layer-by-layer approach was used herein to deposit a gate dielectric, comprised of cross-linked PAH/PAA bilayers, with a controllable thickness. By combining this method with the use of a conducting polymer active layer, we present device performance characteristics as a function of ultra-low dielectric thickness. This approach is also used as a means to develop a more complete understanding of the general operating mechanism behind these stacked TFTs with PEDOT:PSS as the active layer. Although these devices possess a stacked TFT architecture, they appear to operate in the depletion mode as a result of de-doping of the active layer with the

application of a positive gate bias. The crosslinked PAH/PAA multilayers behave as a solid polymer electrolyte, which is different than the standard insulating gate dielectric in traditional field effect transistors. The depletion and recovery rate are highly dependent on the level of hydration in the film and the environment under which the device is operated. These observations are consistent with an electrochemical de-doping of the conducting polymer during operation.

5.2 Experimental

Aqueous stock solutions of PEDOT:PSS, under the tradename of Baytron[®] P with a reported concentration range of 1 – 5%, were purchased from H.C. Stark Inc. and filtered with 1 μm pore size filters prior to use. Spin-coated films of PEDOT:PSS were prepared with solutions comprised of a mixture of the aqueous Baytron P stock solution with ethylene glycol in an 80/20 weight ratio with a small amount (< 1 %) of dodecabenzene sulfonic acid. The films were fabricated by spin-coating at 500 rpm for 10 s and then 3000 rpm for 60 s. Polyelectrolyte solutions (10 mM) were pH adjusted with NaOH and HCl using an Orion model 230A pH meter. Each monolayer deposition cycle (~ 15 min) was followed with multiple rinse steps in deionized (18 MΩ·cm) H_2O in a Carl Zeiss Microm DS-50 automatic slide stainer. Silver and aluminum electrodes were thermally evaporated at a rate of 3 and 4 – 5 Å/s, respectively, in an Explorer 18 Denton Vacuum system (< 10^{-7} Torr) using a Telemark model 860 deposition controller. Film thicknesses were measured with a Tencor P-10 surface profiler at a stylus force of 0.6 mg. The absorbance spectra were obtained using a Varian Cary 5000 UV-Vis-NIR spectrophotometer. The van der Pauw technique was used to determine film resistivity with a Keithley 4200 semiconductor characterization system. The size of the active channel was approximately 2 mm

wide by 3 mm long. The TFT device performance was characterized with two Keithley 2400 SourceMeters.[®] The $I_{DS} - V_{DS}$ characteristics were obtained with a V_{DS} dwell time of 10 seconds and a V_G dwell time of 60 seconds and the $I_{DS} - time$ characteristics were obtained using a V_{DS} of 0.1 V. The $I_{on/off}$ ratios obtained from the data for V_G = 2.0 and 2.5 V were calculated after adjusting the curves to pass through the origin to account for the effects caused by the device leakage current at these low I_{DS} values. Nitrogen was bubbled through deionized water (18 MΩ·cm) to create humidified N_2 conditions in the test chamber (relative humidity ~ 75 %). More precisely controlled humidity conditions were obtained by performing experiments in a SH-241 ESPEC bench-top type temperature and humidity chamber purged with N_2.

5.3 Results and Discussion

A schematic representation of the TFT device configuration used in this study is provided in Figure 1. Bilayers of poly(allylamine hydrochloride) (PAH), the polycation, and poly(acrylic acid) (PAA), the polyanion, were deposited onto an evaporated aluminum gate electrode (350 – 400 Å) through layer-by-layer assembly to obtain a gate dielectric of controllable thickness. The films were then heat-treated at 235 ºC for 4 hours under dry N_2 to chemically crosslink the film to improve stability and impermeability.[127,128] After spin-coating a PEDOT:PSS layer directly onto the assembled dielectric layer, silver source and drain electrodes were vapor deposited on opposite sides of the active channel to complete the device. The PEDOT:PSS active layer thickness varied from 500 – 900 Å with a conductivity of 65 – 75 S/cm. This bottom gate arrangement was utilized to avoid degradation of the conducting polymer layer during heat treatment of the gate dielectric.
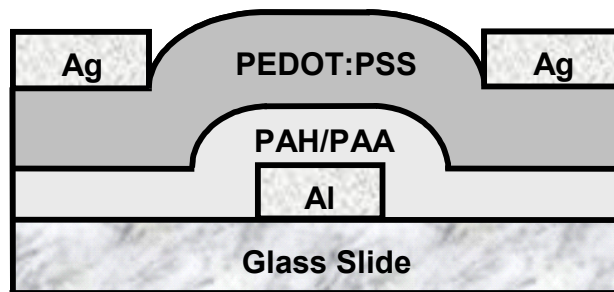
Figure 5-1. Schematic, bottom gate architecture of a TFT device with PEDOT:PSS as the active layer, PAH/PAA as the gate dielectric layer, silver as the source and drain electrodes, and aluminum as the gate electrode.

5.3.1 Device Operation as a Function of Dielectric Thickness

Representative performance characteristics are shown in Figure 2 for a device with a gate dielectric comprised of 10 PAH/PAA bilayers deposited at a pH of 6 to 6.5 that was tested under ambient conditions. Under these conditions, the total thickness of the gate dielectric was approximately 30 Å, which corresponds to an individual bilayer thickness of about 3 Å, consistent with that reported by Shiratori et al.[129] As expected, the application of a positive gate bias resulted in a slow decrease of the source-drain current (I_{DS}) for these devices. Figure 2a shows that as the gate bias was gradually increased from 1.0 to 2.5 V, the device exhibited a higher $I_{on/off}$ ratio, a faster depletion rate, and a recovery rate that was much slower than the depletion rate and appeared to be relatively independent of gate bias. These trends are shown explicitly in Figure 2b whereby the $I_{on/off}$ ratio was calculated from the change in I_{DS}, the depletion rate was characterized by the initial slope (obtained 3 s after the gate bias was applied) of the $I_{DS} - time$ curve, and the recovery rate was characterized by the slope of the $I_{DS} - time$ curve at 10 μA during recovery. Furthermore, the gate current (I_G) exhibited an initial increase upon application of the gate bias, and then decreased exponentially until the gate bias was removed. In all cases, the I_G decreased to several orders of magnitude less than the initial I_{DS}. In addition, the magnitude and time dependence of the gate current are significantly higher than a

simple capacitive charging current due to the gate dielectric. All of these trends are consistent with an electrochemical de-doping effect of the PEDOT:PSS and this will be discussed later in greater detail. It should also be noted that upon prolonged application of the gate bias in an ambient environment (data not shown), the aluminum gate can become electrochemically oxidized, which can affect the observed $I_{on/off}$ ratio, switching speed, and overall device performance. Care should be taken to avoid these effects.

By varying the number of PAH/PAA bilayers deposited, the thickness of the gate dielectric can be precisely tuned. As depicted in Figure 3, both the $I_{on/off}$ ratio and the depletion rate continuously decreased as the number of bilayers was increased from 10 to 40 (film thickness = 30 to 130 Å) with a constant V_G of 2.0 V. Furthermore, when the deposition conditions of the PAH/PAA bilayer film were changed such that much thicker gate dielectric layers than those shown were obtained, a significant decrease in the switching speed was observed. Specifically, when the pH of both polyelectrolyte deposition solutions was set to 3.5, a 40 bilayer PAH/PAA film had a thickness of 2400 Å. Using this film as the gate dielectric resulted in a device with a depletion rate four orders of magnitude less than the comparable devices shown in Figure 3. Only when the gate bias reached approximately 20.0 V did the depletion rate become comparable to those in Figure 3. This trend in switching speed is consistent with previously reported values for similar TFTs utilizing gate dielectric layers of an optical adhesive or a thin spin-coated film of poly(4-vinylphenol).[87,130] The $I_{on/off}$ ratios, however, were significantly lower, possibly due to the use of a top gate electrode architecture, interface effects, or different environmental test conditions. It should also be noted that devices with no PAH/PAA layer did function to a limited extent suggesting that the native aluminum oxide layer (2 – 3 nm)[131] can

serve as the gate dielectric. Indeed, aluminum oxide has previously been used as the dielectric layer, but at much larger thicknesses (26 – 130 nm).[132]Error! Bookmark not defined.
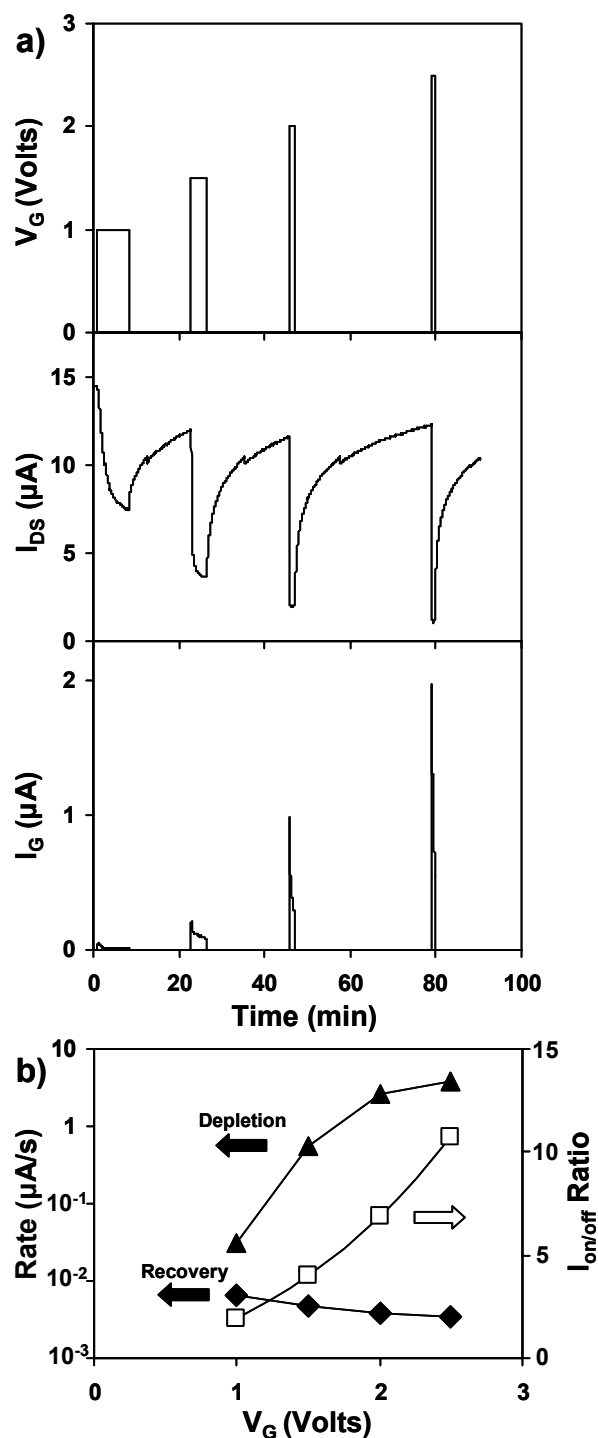
Figure 5-2. a) Performance characteristics of a TFT device tested under ambient conditions. The gate dielectric layer consisted of 10 PAH/PAA bilayers (deposited at a pH of 6.5) with a total thickness of ~ 30 Å. b) Depletion rate (▲), recovery rate at I_{DS} = 10 μA (♦), and $I_{on/off}$ ratio (□) as a function of gate bias for the devices shown in (a).
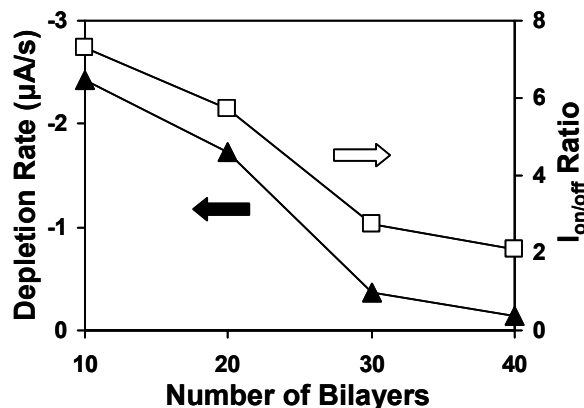
Figure 5-3. Depletion rate (▲) and $I_{on/off}$ ratio (□) as a function of the number of PAH/PAA bilayers deposited as the gate dielectric at a pH of 6.5. Devices were tested at $V_{DS} = 0.1$ V under ambient conditions with the application of a 2.0 V gate bias.

5.3.2 Environmental Influence on Device Performance

Due to the fact that the operating mechanism of these devices is believed to be related to ion motion under the applied field, it is expected that the level of hydration of these films will significantly influence their performance characteristics. In addition to testing under ambient conditions as described above, TFT devices were tested under both dry and humidified N_2 conditions. Representative $I_{DS} - V_{DS}$ characteristics obtained for a device with 40 PAH/PAA bilayers as the gate dielectric, under humidified N_2 conditions, are presented in Figure 4a. An approximately linear relationship was observed in all cases with a minor deviation around the origin, likely due to effects caused by ongoing depletion, ion drift within the film, or cross-talk between the electrodes. The $I_{on/off}$ ratios (at $V_{DS} = 0.1$ V) were significantly higher than those shown previously obtained under ambient conditions and agree with other reported values.[10887,130] The same general trends as those discussed above for increasing gate voltage and decreasing dielectric thickness were observed for devices tested under humidified N_2 conditions. Figure 4b illustrates the effects that the test environment has on the performance characteristics

of this device by showing I_{DS} as a function of gate bias under different test conditions. By comparing the data taken under ambient conditions (relative humidity (RH) $\sim 30 - 40\%$) to those taken under humidified N_2 conditions (RH $\sim 75\%$), it can be seen that the higher level of humidity not only caused a higher $I_{on/off}$ ratio, but also induced the device to switch at lower voltages. Surprisingly, when the device was operated in a dry environment, effectively no change in the I_{DS} was observed with V_G. In other words, the device switching behavior was completely inhibited when moisture was removed from the film.
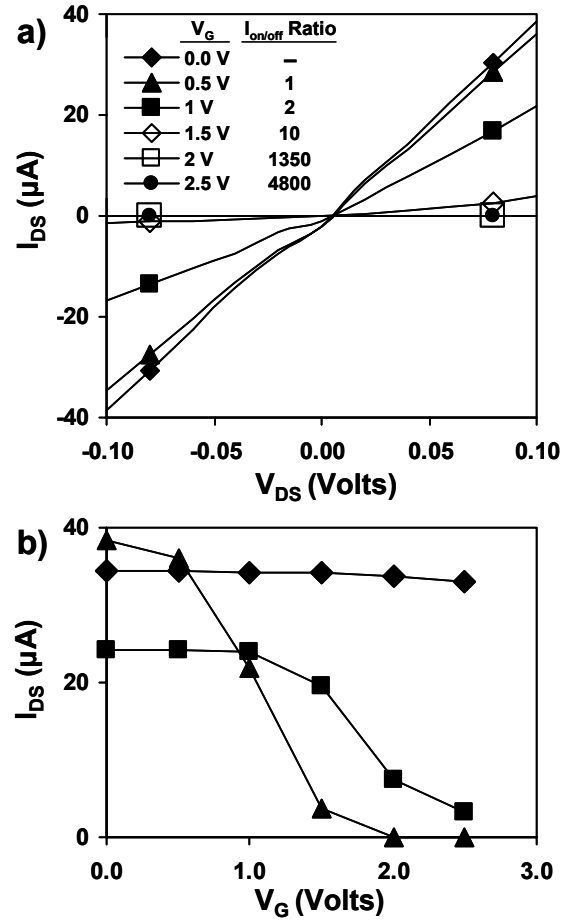
Figure 5-4. a) $I_{DS} - V_{DS}$ characteristics (at $V_{DS} = 0.1$ V) of a device tested under a humidified N_2 environment with a gate dielectric layer comprised of 40 PAH/PAA bilayers deposited at a pH of $6 - 6.5$ (thickness = 130 Å). b) $I_{DS} - V_G$ characteristics (at $V_{DS} = 0.1$ V) for this device tested under dry N_2 (♦), ambient (■), and humidified N_2 (▲) conditions.

To probe this effect further, device testing was performed under carefully controlled humidification conditions in a separate humidity chamber. Figure 5 shows the results for a device with 10 PAH/PAA bilayers as the gate dielectric tested under a RH value ranging from 0 to 75%. Consistent with the results above, both the $I_{on/off}$ ratio and the depletion rate systematically increased with RH. Apparently, the incorporation of moisture into the film is required for these devices to operate and better device performance is obtained with higher moisture content. This requirement is emphasized by the fact that if N_2 was bubbled through anhydrous methanol or ethanol (instead of water) before exposing it to the device, the effect was the same as with dry N_2. That is to say, the device switching behavior was inhibited.
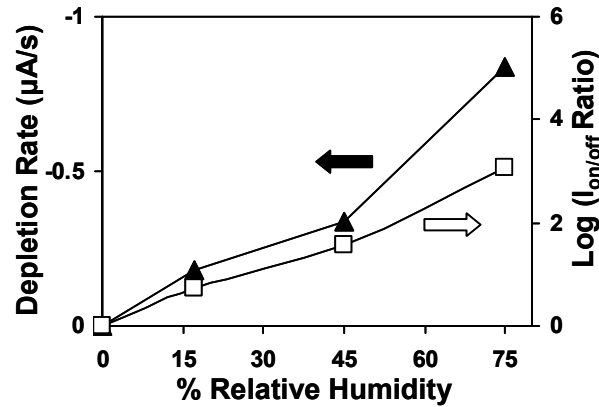
Figure 5-5. Depletion rate (▲) and $I_{on/off}$ ratio (□) (measured at 3 – 5 seconds and 260 seconds after application of the gate bias, respectively) for a device tested under a range of relative humidities at a gate bias of 1.25 V and having a gate dielectric comprised of 10 PAH/PAA bilayers deposited at a pH of 6 – 6.5 (thickness = 30 Å).

5.3.3 Depletion Mechanism

As mentioned above, the observed device behavior is consistent with an electrochemical de-doping of the PEDOT:PSS during device operation. Due to the dependence of the device performance on water content, equation (1) is presented as a description of the way in which the device operates. With a positive V_G, the aluminum gate electrode (see Figure 1) serves as the

anode at which the oxidation of water occurs to generate $O_2(g)$. Since crosslinked PAH/PAA

multilayers with a film resistivity of 5 $M\Omega$ cm^2 have been shown to passivate aluminum,[133] the

increase in ionic conductivity at higher levels of humidity are required for this mechanism.[134]

The source electrode serves as the cathode at which the oxidized $PEDOT^+$ molecules are reduced

back to their neutral species (i.e. de-doped). The protons generated at the anode can

subsequently migrate through the polyelectrolyte multilayer gate dielectric film to produce SO_3H

at the cathode. Consequently, a higher gate bias results in a faster depletion rate and a larger

$I_{on/off}$ ratio due to a larger driving force for ion migration and PEDOT de-doping. Similarly,

using a thicker gate dielectric (more PAH/PAA bilayers) results in both a smaller depletion rate

and $I_{on/off}$ ratio due to a reduction of the effective electric field. Water must be present for

oxidation, otherwise operation is inhibited, as observed.

$$\textbf{Anode:} \qquad\qquad 2H_2O(l) \rightarrow 4H^+(aq) + O_2(g) + 4e^- \qquad E^o_{ox} = -1.2\,V$$

$$\textbf{Cathode:} \qquad 4PEDOT^+ : PSS^-(s) + 4e^- \rightarrow 4PEDOT^0 : PSS^-(s) \qquad E^o_{red} \approx E_{1/2} \approx 0.2\,V$$

$$\textbf{Overall:}\ \ 4PEDOT^+ : PSS^-(s) + 2H_2O(l) \rightarrow 4PEDOT^0 : PSSH(s) + O_2(g) \quad E^o_{cell} \approx -1.0\,V \qquad \textbf{(5.1)}$$
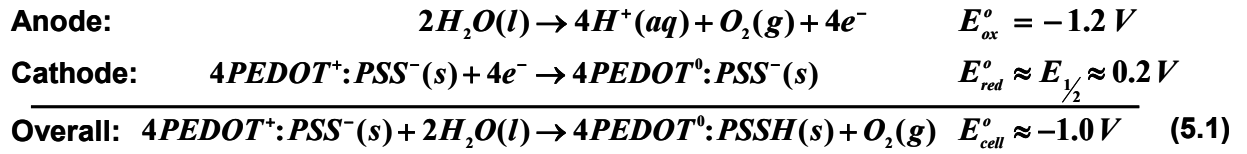
5.3.4 Recovery after Depletion under Humidified N_2 Conditions

The recovery behavior of the device was previously described above as being independent

of the gate bias applied. Upon removal of the gate bias, the reaction equilibrium favors the

doped form of PEDOT and so the rate of recovery is solely dependent upon this reverse reaction

rate. Given enough time, however, the $O_2(g)$ that is generated during depletion will diffuse out

of the film thereby prohibiting the back reaction (i.e. recovery) when the gate bias is removed.

This effect is illustrated in Figure 6 for a device with 10 PAH/PAA bilayers as the gate dielectric

tested under humidified N_2 conditions. By applying a gate bias of 1.5 V, the device becomes

completely depleted ($I_{on/off}$ ratio ~ 10^3) in approximately 4.5 minutes. If the gate bias were to be

removed at this point, the device would immediately begin to recover as demonstrated above. However, the gate bias is maintained at 1.5 V for 12 minutes. When the gate bias was removed after this time, the device effectively failed to recover and remained in the "off" state even though the gate bias had been removed. This effect is simply due to the fact that the $O_2(g)$ generated during depletion has diffused out of the film thereby prohibiting the back reaction (1) when the gate bias is removed. If the device is subsequently exposed to $O_2(g)$ again (at time ~ 45 min in Figure 6), the device immediately begins to recover at a rate that is consistent with that shown above under ambient conditions. Similar types of electrochemical effects have been demonstrated for PEDOT:PSS using laterally arranged devices and an electrolyte.[135] Additionally, the electrolysis of water is known to change the doping level of conjugated polymers[136] and is suspected of forming black spots in LEDs by reducing the PEDOT.[137]
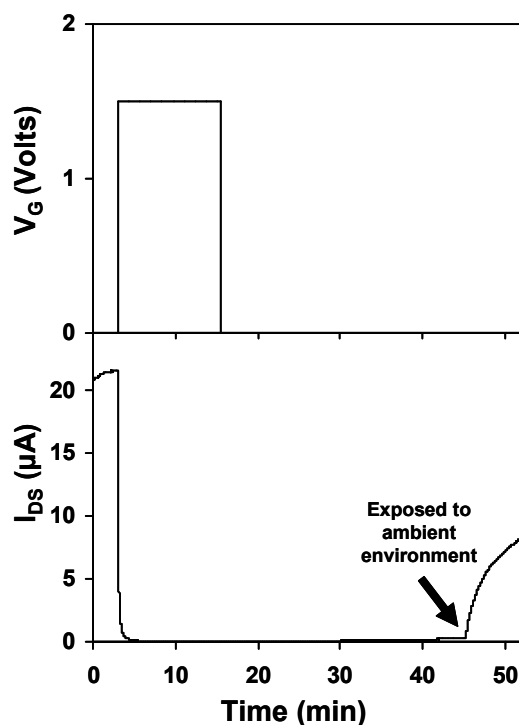
Figure 5-6. Time-dependent performance characteristics (at $V_{DS} = 0.1$ V) of a TFT device with a gate dielectric comprised of 10 PAH/PAA bilayers deposited at a pH of 6 – 6.5 (thickness = 30 Å). Testing was initially done under humidified N_2 conditions and switched to ambient conditions after 45 minutes.

5.3.5 Characterization of Device Operation using VIS-NIR Spectroscopy

To provide further evidence for this electrochemical de-doping mechanism, TFT devices were made using indium tin oxide (ITO) as a transparent gate electrode in order to investigate the optical properties of the active layer *in-situ*. Other than using a transparent gate electrode, the devices had the same architecture and operated with the same trends as previously discussed. The absorption spectra shown in Figure 7 were obtained for a device with ITO as the gate electrode and 40 PAH/PAA bilayers as the gate dielectric. The initial spectrum obtained before the application of a gate bias (V_G = 0.0 V) under humidified N_2 conditions clearly indicates the presence of doped PEDOT with broad peaks present at 965 nm and beyond 1500 nm, which are representative of the subgap states for the polaron and bipolaron charge carriers.[138] In addition the small peak at 650 nm corresponds to the $\pi \rightarrow \pi*$ transition in undoped PEDOT. Upon application of a gate bias (V_G = 4.0 V), the broad peak beyond 1500 nm decreases with a corresponding increase in the peaks at 965 nm and 650 nm. These spectral changes are consistent with a reduction in the doping level of the PEDOT[139] upon application of a positive gate bias. While the exact nature of the de-doping process is not completely understood, a multi-step electron transfer process has previously been reported to account for changes in the doping level of PEDOT and the associated changes in spectral features.[140]
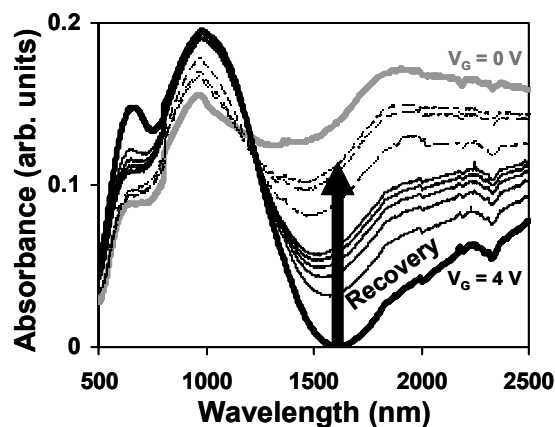
Figure 5-7. Absorption spectra obtained *in-situ* during operation of a device with an ITO gate electrode and a gate dielectric comprised of 40 PAH/PAA bilayers deposited at a pH of 6 – 6.5 (thickness = 130 Å). Spectra were obtained under humidified N_2 conditions before (thick grey line) and after (thick black line) a gate bias of 4.0 V was applied. During recovery, spectra (taken at 280 s intervals) were obtained first under humidified N_2 conditions (thin solid lines) and subsequently under ambient conditions (thin dashed lines).

Upon removal of the gate bias, the device starts to recover and the spectral features tend toward their initial, doped state. The initial recovery in a humidified N_2 environment (thin solid lines in the figure) is likely due to $O_2(g)$ remaining in the film, but this recovery becomes arrested and full recovery (re-doping) can only be obtained when the device is exposed to the ambient (i.e. O_2) environment (thin dashed lines), consistent with the results shown above.

5.4 Conclusion

The incorporation of ultra-thin polymer dielectric layers into TFT devices has been demonstrated using a layer-by-layer assembly deposition technique. The $I_{on/off}$ ratio and depletion rate for these devices increased with a higher gate bias or a lower dielectric thickness. An electrochemical mechanism involving water oxidation and $PEDOT^+$ de-doping (i.e. reduction) was presented as the depletion mechanism for these devices. The fact that moisture is required for depletion, $O_2(g)$ needed for recovery, and that the recovery rate is independent of gate bias, support this mechanism. The spectral evidence of de-doping and re-doping of the

active layer also provides additional support for this mechanism. While layer-by-layer deposition of the gate dielectric has been demonstrated for transistors based on doped, conducting polymer layers, it may be applicable to other types of transistor architectures in which ultra-thin, pin-hole free gate dielectrics are desirable.

5.5 References

124. a) Epstein, A. J.; Hsu, F.-C.; Chiou, N.-R.; Prigodin, V. N. *Current Appl. Phys.* **2002**, *2*, 339. b) Epstein, A. J.; Hsu, F.-C.; Chiou, N.-R.; Waldmann, O.; Park, J. H.; Kim, Y.; Prigodin, V. N. *Proc. SPIE-Organic Field Effect Transistors II* **2003**, *5217*, 141.

125. Nilsson, D.; Chen, M.; Kugler, T.; Remonen, T.; Armgarth, M.; Berggren, M. *Adv. Mater*. **2002**, *14*, 51.

126. Zhu, Z.-T.; Mabeck, J. T.; Zhu, C.; Cady, N. C.; Batt, C. A.; Malliaras, G. G. *Chem. Commun*. **2004**, 1556.

127. Durstock, M. F.; Rubner, M. F. *Langmuir* **2001**, *17*, 7865.

128. Harris, J. J.; DeRose, P. M.; Bruening, M. L. *J. Am. Chem. Soc.* **1999**, *121*, 1978.

129. Shiratori, S. S.; Rubner, M. F. *Macromolecules* **2000**, *33*, 4213.

130. Epstein, A. J.; Park, J. H.; Youngmin, K.; Hsu, F.-C.; Chiou, N.-R.; Waldmann, O.; Prigodin, V. N. *Polym. Prepr. (Am. Chem. Soc., Div. Polym. Chem.)* **2004**, *45(1)*, 149.

131. Shimizu, K.; Furneaux, R. C.; Thompson, G. E.; Wood, G. C.; Gotoh, A.; Kobayashi, K. *Oxidation of Metals* **1991**, *35*, 427.

132. Majewski, L. A.; Grell, M.; Ogier, S. D.; Veres, J. *Organic Electronics* **2003**, *4*, 27.

133. Dai, J.; Sullivan, D. M.; Bruening, M. L. *Ind. Eng. Chem. Res.* **2000**, *39*, 3528.

134. Durstock, M. F. Ph. D. Thesis, Department of Materials Science and Engineering, Massachusetts Institute of Technology, Cambridge, 1999.

135. Andersson, P.; Nilsson, D.; Svensson, P.-O.; Chen, M.; Malmström, A.; Remonen, T.; Kugler, T.; Berggren, M. *Adv. Mater.* **2002**, *14*, 1460.

136. Li, Y.; Qian, R. *Synth. Met.* **1993**, *53*, 149.

137. Kim, J. S.; Ho, P. K. H.; Murphy, C. E.; Baynes, N.; Friend, R. H. *Adv. Mater*. **2002**, *14*, 206.

138. a) Gustafsson, J. C.; Liedberg, B.; Inganäs, O. *Solid State Ionics* **1994**, *69*, 145. b) Patil, A. O.; Heeger, A. J.; Wudl, F. *Chem. Rev.* **1988**, *88*, 183.

139. Bredas, J. L.; Wudl, F.; Heeger, A. J. *Solid State Commun.* **1986**, *59*, 415.

140. Chen, X.; Inganas, O. *J. Phys. Chem.* **1996**, *100*, 15202.

Chapter 6

Bistability in Doped Organic Thin Film Transistors

6.1 Introduction

The use of doped organic polymers such as PEDOT:PSS as the active layer in thin film transistors (TFTs) has recently gained interest with the discovery of an unexpected field effect upon the application of a positive gate bias in these devices.[141] While the operating mechanism is not completely understood, possibilities that have been suggested include the existence of an ion-leveraged mechanism to disrupt the percolation path,[142] an electrochemical de-doping effect,[143] or a combination of both.[144] Layer-by-layer assembly of cross-linked poly(allylamine hydrochloride)/poly(acrylic acid) (PAH/PAA) bilayers was demonstrated in Chapter 5 as a method to incorporate ultra-thin gate dielectric layers into these types of transistors.[145] This assembly method involves dipping a substrate between two dilute polyelectrolyte solutions of opposite charge (i.e. a polycation and a polyanion) to build up a thin film via the electrostatic interactions between the polyelectrolytes. The depletion mechanism for these devices was shown to depend on an electrochemical redox reaction resulting in a de-doping of the active layer through the oxidation of water.

In this work, the recovery behavior of doped organic TFTs using cross-linked PAH/PAA bilayers as the gate dielectric layer was studied. By examining the device performance under different environmental test conditions, a more complete understanding of the device operation and of the role that water plays in this behavior is achieved. In addition, *in-situ* Raman spectroscopy was used to investigate the influence that these effects have on the intrinsic doping level of the PEDOT:PSS active layer.

6.2 Experimental

Aqueous stock solutions of PEDOT:PSS, under the trade name of Baytron® P with a reported concentration range of 1 – 5%, were purchased from H.C. Stark Inc. and filtered with 1 μm pore size filters prior to use. Spin-coated films of PEDOT:PSS were prepared with solutions comprised of a mixture of the aqueous Baytron P stock solution with ethylene glycol in an 80/20 weight ratio with a small amount (< 1%) of dodecabenzene sulfonic acid.   The films were spin-coated at 500 rpm for 10 s and then 3000 rpm for 60 s. Polyelectrolyte solutions (10 mM) were pH adjusted with NaOH and HCl using an Orion model 230A pH meter.   Each monolayer deposition cycle (~ 15 min) was followed with multiple rinse steps in deionized H_2O (18 MΩ·cm) in a Carl Zeiss Microm DS-50 automatic slide stainer. Silver and aluminum electrodes were thermally evaporated at a rate of 3 and 4 – 5 Å/s, respectively, in an Explorer 18 Denton Vacuum system (< 10^{-7} Torr) using a Telemark model 860 deposition controller. The aluminum gate electrode was deposited to a thickness of 350 – 400 Å. The size of the active channel was approximately 2 mm wide by 3 mm long. Film thicknesses were measured with a Tencor P-10 surface profiler at a stylus force of 0.6 mg. The TFT device performance was characterized with two Keithley 2400 SourceMeters.® Gases (air or N_2) were bubbled through deionized water (18 MΩ·cm) to create humidified conditions (relative humidity (RH) ~ 75%), purged through Drierite® to create dry conditions, and a mixture of both to create intermediate conditions (RH = 30%) in the test chamber. Raman spectra were obtained with a Renishaw inVia Raman Microscope using a Melles Griot Argon Laser.

6.3 Results and Discussion

Thin film transistors using PEDOT:PSS as the active layer and layer-by-layer assembled films as the gate dielectric have previously been studied and were shown to operate via an electrochemical de-doping process.[145] By way of describing this process, equation (1) is presented to illustrate the means by which depletion occurs in these devices. Upon application of a positive gate bias, the gate electrode serves as the anode at which water is oxidized to produce $O_2(g)$. The source electrode serves as the cathode at which PEDOT becomes reduced back to its neutral state $(E_{1/2} \sim 0.2~V)$[146] resulting in a decrease in the conductivity of the active layer and device "turn-off." Sulfonic acid (SO_3H) groups are generated on the PSS due to proton migration from the gate electrode. As a result, the *depletion* behavior was shown to depend critically on the level of water and $O_2(g)$ in the test environment.[145]

Depletion Mechanism

Anode (Gate with +V$_G$): $\qquad 2H_2O(l) \rightarrow 4H^+(aq) + O_2(g) + 4e^- \qquad E^o_{ox} = -1.23~V$

Cathode (Source): $4PEDOT^+{:}PSS^-(s) + 4e^- \rightarrow 4PEDOT^0{:}PSS^-(s) \qquad E^o_{red} \approx E_{1/2} \approx 0.2~V$

Overall: $\qquad 4PEDOT^+{:}PSS^-(s) + 2H_2O(l) \rightarrow 4PEDOT^0{:}PSSH(s) + O_2(g) \quad E^o_{cell} \approx -1.0~V$ **(6.1)**
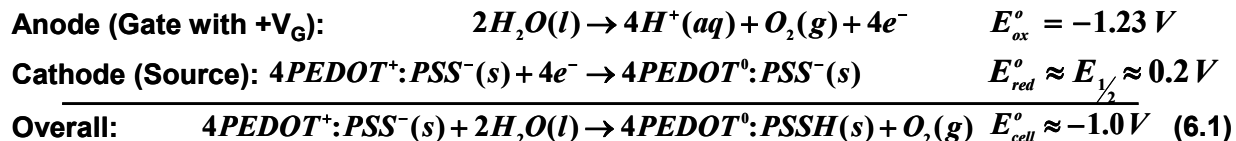
6.3.1 Recovery of the Active Layer under Different Environmental Conditions

To probe these effects further, the *recovery* behavior of a device was studied as a function of the test environment. Figure 1 shows the time-dependent performance characteristics of a TFT device using PEDOT:PSS (thickness = 500 – 900 Å) as the active layer and a cross-linked, layer-by-layer assembled film of PAH/PAA (thickness = 60 Å) as the gate dielectric layer. Upon application of a positive gate bias $(V_G = 2.5~V)$, the source-drain current (I_{DS}) decreases to turn the device to the "off" state. This initial switching of the device was conducted under humidified N_2 conditions. After the gate bias is removed (still under humidified N_2 conditions), the device immediately begins to recover as evidenced by an increase in I_{DS}. This recovery is due to

trapped $O_2(g)$ remaining in the film, which causes the reverse of reaction (1) to occur and the concomitant increase in the level of doped PEDOT when the gate bias is removed. When water is removed from the test environment by exposing the device to a purge of dry N_2, this recovery behavior becomes almost completely arrested. Although subsequent exposure of the device to dry air results in the resumption of the recovery due to a higher concentration of $O_2(g)$, the magnitude of I_{DS} does not reach its initial value. Only when the device is exposed to a humidified air environment does I_{DS} reach (and even surpasses) what it was initially. This behavior is consistent with the reversal of the mechanism put forth in equation (1). In order for spontaneous recovery (i.e. re-doping of the active layer) to occur, $O_2(g)$ must be present in the film in a high enough concentration and with sufficient mobility. Correspondingly, moisture contained in the film acts as both the reductant, as well as a plasticizer to increase the mobility within the film.

Figure 6-1. Time-dependent performance characteristics (at $V_{DS} = 0.1$ V) under different test conditions of a TFT device with PEDOT:PSS as the active layer and 20 PAH/PAA bilayers as the gate dielectric (deposited at a pH of 6 – 6.5 with a total thickness ~ 60 Å).

6.3.2 Induced Recovery of the Active Layer

It is interesting to note that if a *negative* gate bias is applied after the device has been depleted (i.e. turned "off"), it can be induced to quickly recover. In Figure 2, a *positive* gate bias of 3 V was used to initially deplete the device under humidified N_2 conditions (75% relative humidity (RH)) to an $I_{on/off}$ ratio ~ 70. As shown, if this bias is applied for a relatively short amount of time (~ 5 min), and then removed, the device begins to recover due to trapped $O_2(g)$ remaining in the film, consistent with the discussion above. If, however, this positive gate bias is applied for a longer period of time (~ 27.5 min), then when it is removed (at time ~ 35 min in the figure), the recovery is completely inhibited because no $O_2(g)$ is present since it has diffused out of the film. The device remains in the "off" state despite the fact that the gate bias has been removed. If a negative gate bias ($V_G = -2.5$ V) is subsequently applied, recovery is induced as

117

seen by an increase in I_{DS}. However, once this gate bias is removed, I_{DS} again begins to decrease. This same negative gate bias was applied three more times, each for approximately two minutes with about nine minutes in between each application. As shown, each time the gate bias is removed, I_{DS} begins to decrease, but at a slower rate and to a lesser extent. In fact, if the negative gate bias were applied long enough, I_{DS} would not decrease upon its removal, but would remain stable and the device would remain in the "on" state. It should be noted that care must be taken to avoid overoxidation of the PEDOT in the active layer upon induced recovery. The overoxidation of PEDOT is commonly suspected as the cause for permanent degradation of the active layer upon prolonged application of a negative gate bias.[141,147]
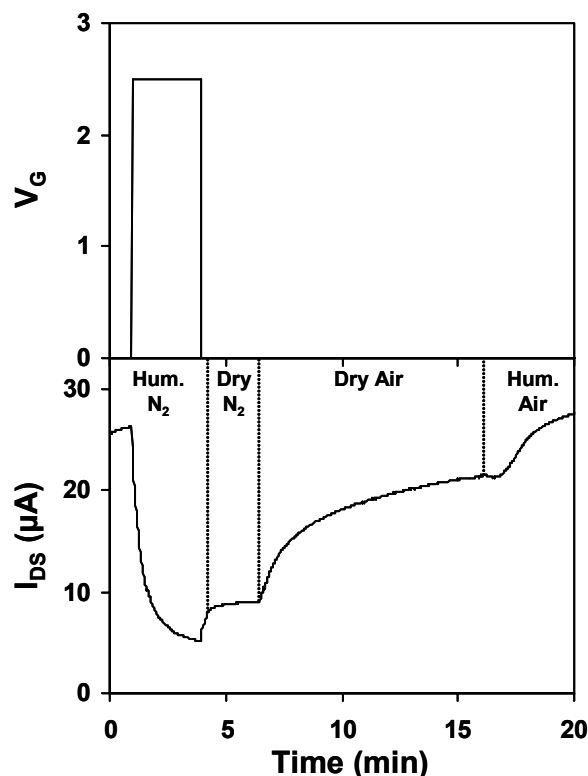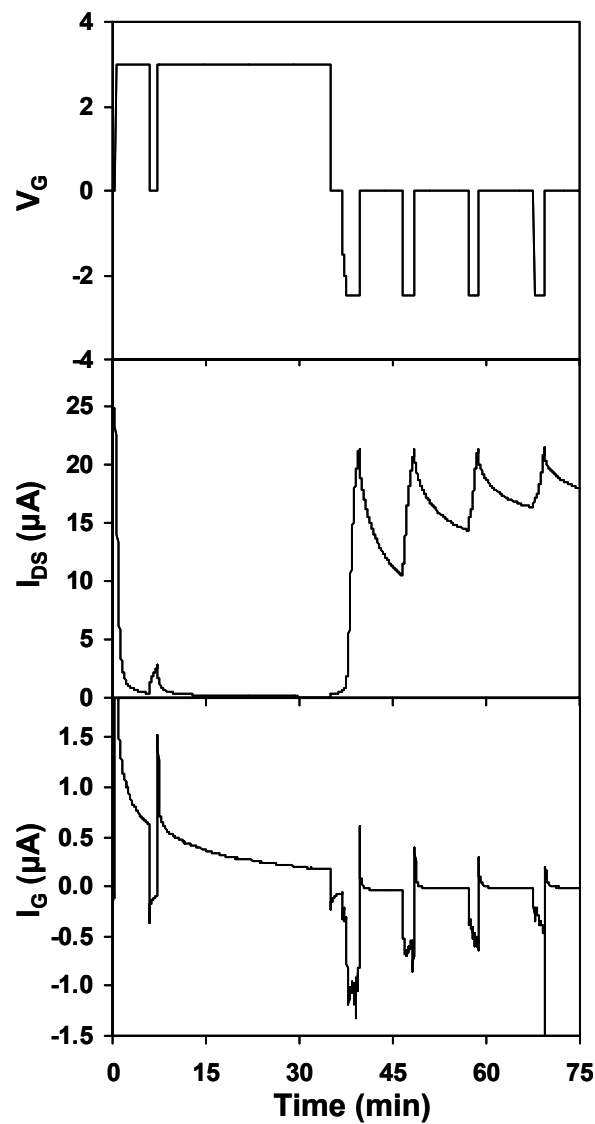
Figure 6-2. Time-dependent performance characteristics (at V_{DS} = 0.2 V) of a TFT device with PEDOT:PSS as the active layer and 40 PAH/PAA bilayers as the gate dielectric layer (deposited at a pH of 6 – 6.5 with a total thickness ~ 130 Å). The device was tested under humidified N_2 conditions (RH ~ 75%).

6.3.3 Mechanism for Induced Recovery

This induced recovery behavior is similar in nature but opposite in magnitude to the depletion behavior discussed above and in prior work.[145] The PEDOT:PSS active layer is electrochemically de-doped with a positive gate bias and it is subsequently induced to recover (i.e. re-doped) with a negative gate bias. By way of describing this process, equation (2) is

presented to illustrate the means by which recovery occurs in these devices. Upon application of a negative gate bias, the gate electrode serves as the cathode at which water is reduced to generate $H_2(g)$ and OH^- ions. The source electrode serves as the corresponding anode to re-oxidize (i.e. re-dope) neutral $PEDOT^0$ that was generated during depletion. The OH^- ions can subsequently migrate from the cathode to the anode to de-protonate the SO_3H groups of PSS. The overall net effect of a negative gate bias is to induce the recovery of the de-doped active layer through an electrochemical reduction of water to generate $H_2(g)$. Maintaining the negative gate bias for a long enough period of time will enable $H_2(g)$ to diffuse out of the device, thereby shifting the state of reaction equilibrium to favor the "on" state. It should be noted that the gate current observed during the switching of these doped organic TFTs (Figure 2) has previously been attributed to an ionic current.[148] For the devices shown here, the I_G observed with an applied gate bias is attributed to a combination of both faradaic (redox) and non-faradaic (ionic) processes associated with the electrochemical reactions put forth in equations (1) and (2). In addition, when the gate bias is removed, the magnitude of I_G is observed to reverse direction and decay exponentially, which is attributed to the ions drifting back to their original state of equilibrium as the reverse of reactions (1) and (2) proceed. It can be seen that the longer the negative gate bias is applied, the resulting gate current decreases due to the device being switched back to a stable "on" state. This type of behavior involving the oxidation and reduction of water to control the doping level of organic materials systems has previously been demonstrated[149] and is similar to what is observed here.

Induced Recovery Mechanism

Anode (Source): $2PEDOT^0{:}PSSH(s) \rightarrow 2PEDOT^+{:}PSSH(s) + 2e^-$ $E^o_{red} \approx E_{1/2} \approx 0.2\,V$

Cathode (Gate with -V_G): $2H_2O(l) + 2e^- \rightarrow H_2(g) + 2OH^-(aq)$ $E^o_{ox} = -0.83\,V$

Overall: $2PEDOT^0{:}PSSH(s) \rightarrow 2PEDOT^+{:}PSS^-(s) + H_2(g)$ $E^o_{cell} \approx -0.6\,V$ (6.2)
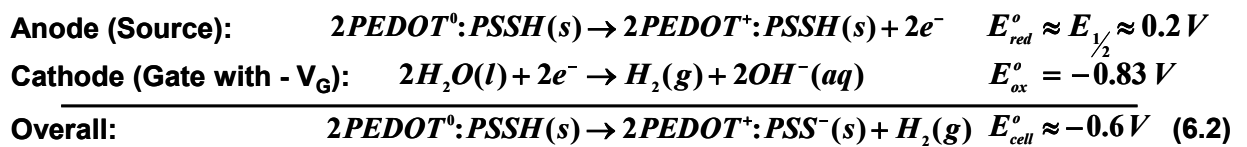
6.3.4 Bistability of the Active Layer under Controlled N$_2$ Conditions

As a result of being able to systematically control the doping state of the film by the application of either a positive or negative gate bias, bistable device operation can be achieved as shown in Figure 3. Although bistable operation of PEDOT/PSS electrochemical transistors has previously been demonstrated using lateral architectures of non-closed circuits, the bistability observed herein is obtained with controlled environmental conditions.[150] In this case, the device was tested under a lower relative humidity (RH ~ 30%) than that described above (RH ~ 75%). The device was alternately switched between stable "off" and "on" states with a positive (V_G = 4 to 6 V) and negative (V_G = – 4 to – 5 V) gate bias, respectively. The magnitude of I_{DS} changed from approximately 0.5 μA in the "off" state to approximately 10.5 μA in the "on" state. Due to the fact that this device was tested at a lower RH than those discussed above, a higher V_G was required to induce a change in I_{DS}, the magnitude of I_G (for any given V_G) was lower, and the tendency to overoxidize PEDOT (as indicated by a rapid, irreversible drop in I_{DS}[141]) appeared to decrease.

It should be noted that under these conditions, each time the gate bias is removed (either positive or negative), the magnitude of I_{DS} remains constant at the current value, and does not tend towards what it was previously, as was shown in Figures 1 and 2. In those cases, the magnitude of I_{DS} becomes stable only when the gate bias is applied for a long enough time to allow all of the $O_2(g)$ or $H_2(g)$ that is generated (see equations 1 and 2) to diffuse out of the film, thereby prohibiting the back reaction. In this case, the gate bias is applied for a sufficiently short amount of time that these products have not diffused out of the film. Instead, the lower level of humidity that is used in the test environment is unable to "plasticize" the matrix enough to allow for significant diffusion of these species. Apparently, enough moisture is present to act as the

reactant for both oxidation and reduction of PEDOT:PSS in equations (1) and (2), but not enough

to permit whole-scale diffusion of the reaction products. Consequently, while water acts as both

the reactant and plasticizer in these devices, a lower RH provides a means to enable bistable

device operation by reducing the mobility of other species in the film.
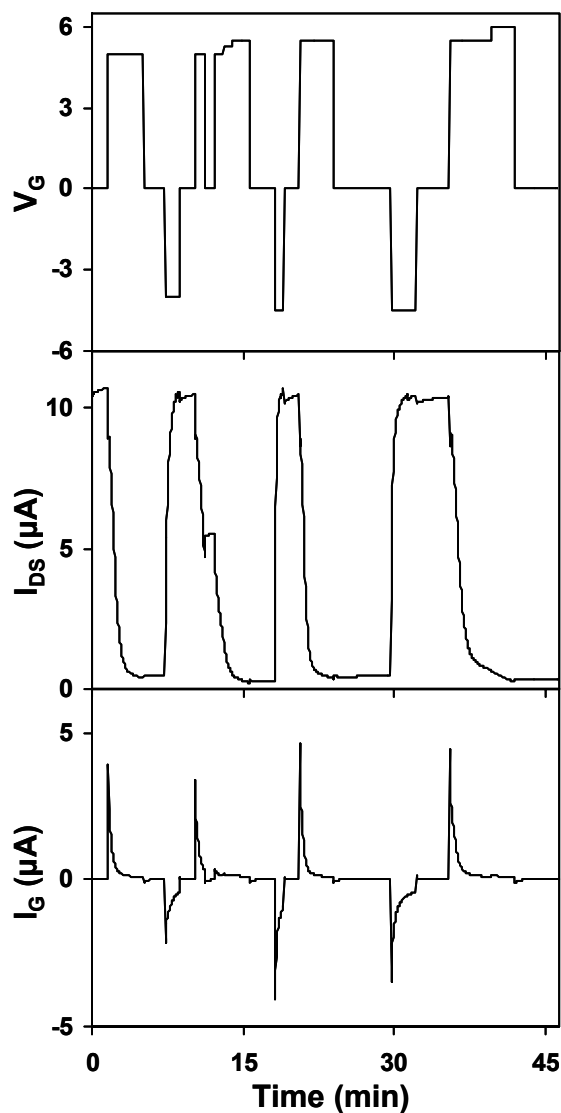
Figure 6-3. Time-dependent performance characteristics (at $V_{DS} = 0.2$ V) of the same device described in Figure 2, but tested under humidified N_2 at 30% RH.

Further support of this effect is shown in Figure 4 whereby a device is first equilibrated in a

humidified N_2 environment before operation. Immediately before applying a positive gate bias,

the test environment is switched to dry N_2. The device becomes depleted in approximately 5.5

122

minutes with an $I_{on/off}$ ratio ~ 300 due to the presence of moisture still contained in the film. Once the gate bias is removed, I_{DS} does not begin to recover as before, but rather the device remains in the "off" state because of the low mobility of the reactant products generated during depletion. Once moisture is re-introduced into the film by exposing it to a humidified N_2 environment, the device begins to recover because of the increased mobility of the $O_2(g)$ trapped in the film and the ability to re-oxidize the neutral PEDOT^0 generated during depletion. It should be noted that when the device was operated in a dry environment, an unexpected increase in I_G was sometimes observed. This effect could be eliminated by re-equilibrating with moisture. While not completely understood, this behavior is believed to be due to defects introduced into the polyelectrolyte multilayer gate dielectric resulting in an increase in the leakage current.
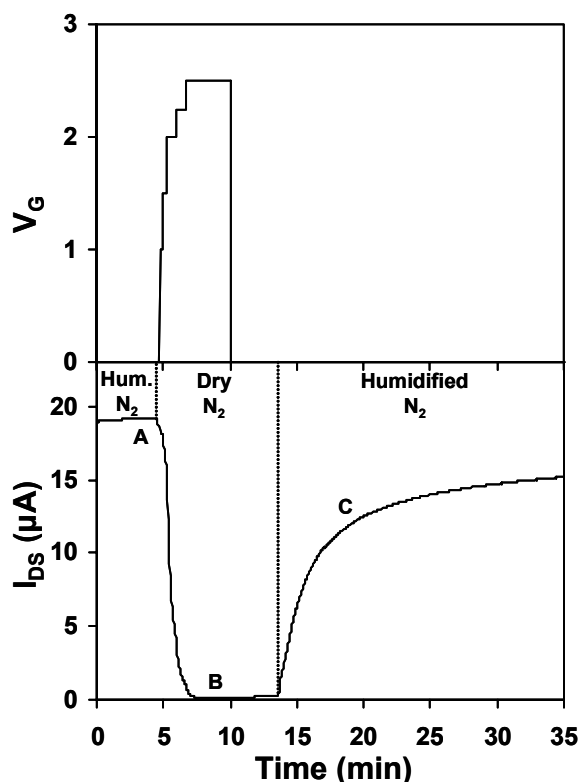
Figure 6-4. Time-dependent performance characteristics (at V_{DS} = 0.2 V) of a TFT device with PEDOT:PSS as the active layer and 40 PAH/PAA bilayers as the gate dielectric layer (deposited at a pH of 6 – 6.5 with a total thickness ~ 130 Å). The device was initially exposed to humidified N_2 (RH ~ 75%) and then purged with dry N_2 immediately before the gate bias was ramped up to 2.5 V. The labels A through C indicate the time at which the Raman spectra shown in Figure 5 were obtained.

123

6.3.5 Characterization of Device Operation using Raman Scattering Technique

Raman scattering was used to clarify the role that these effects have on the doping level of the PEDOT:PSS active layer during device operation under the environmental conditions described above. The Raman spectra presented in Figure 5 were obtained using an excitation wavelength (λ_{exc} = 514 nm) that exhibits a resonance with the $\pi \rightarrow \pi^*$ transition of PEDOT.[151] Spectra A, B, and C were obtained *in-situ* during device operation at the times and under the conditions shown in Figure 4. Before depletion, the spectrum appeared almost completely featureless (A), but after applying a gate bias (V_G = 2.5 V), peaks appeared at 989, 1365, 1428, and 1506 cm^{-1} (B). These peaks have previously been assigned to the ring deformation, $C_\beta - C_\beta$ stretch, $C_\alpha - C_\beta$ symmetrical stretch, and the $C_\alpha - C_\beta$ asymmetrical stretch of PEDOT, respectively.[152] An increase in the intensity of these peaks has been shown to correlate with a reduction in the doping level of the PEDOT.[151] These trends agree with the decrease observed in the I_{DS} after the gate bias was applied. As the device begins to recover upon exposure to a humidified N_2 environment, the peak intensities again decrease (C), consistent with an increase in both the PEDOT doping level and I_{DS}.
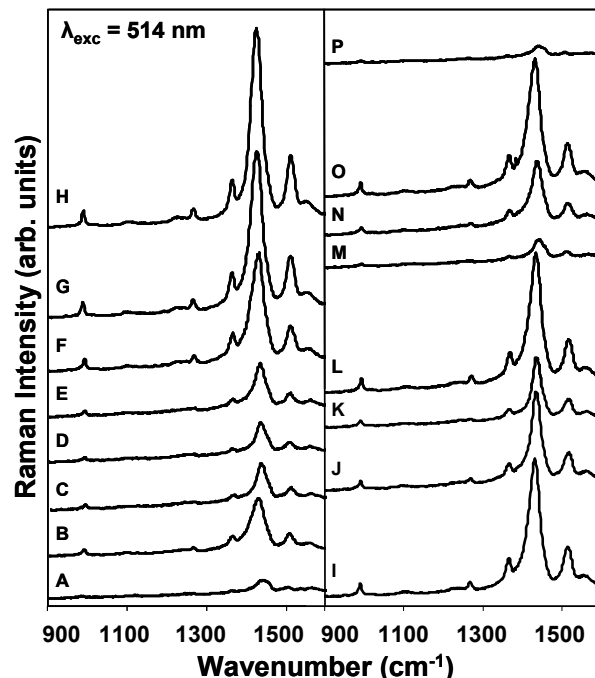
Figure 6-5. Raman spectra obtained *in-situ* during operation for the device described in Figures 4 and 6. Labels A through P correspond to the times indicated in Figures 4 and 6.

The remaining spectra shown in Figure 5 were obtained by continued testing of this device under a humidified N_2 environment. The device performance characteristics associated with these spectra are shown in Figure 6. The data for points D through H show that as the gate bias is increased from 0.0 to 2.0 V, the device becomes depleted (I_{DS} decreases) due to an increase in the level of de-doping of the PEDOT (i.e. increasing peak intensities in the Raman spectra). In addition, by comparing spectra B (dry N_2) and H (humidified N_2), the effects of humidity on the PEDOT doping level can be seen. In particular, the level of de-doping that occurred under a dry N_2 environment (B) was significantly lower than that under humidified N_2 (H), despite the fact that a higher gate bias was applied for B. The lower moisture content in the film at B limits the level of de-doping that can occur. However, it should also be noted that other, more subtle effects present themselves when comparing results obtained under these different conditions. It can be seen from the Raman spectra that at point B, the PEDOT has a higher level of doping

125

(smaller peak intensities) than at point F. However, I_{DS} (and hence the conductivity) is larger for point F (see Figures 4 and 6). This effect is not completely understood but is possibly the result of a morphology-dependent change in conductivity upon exposure to moisture that is analogous to the known, secondary doping effect of PEDOT:PSS.[153]
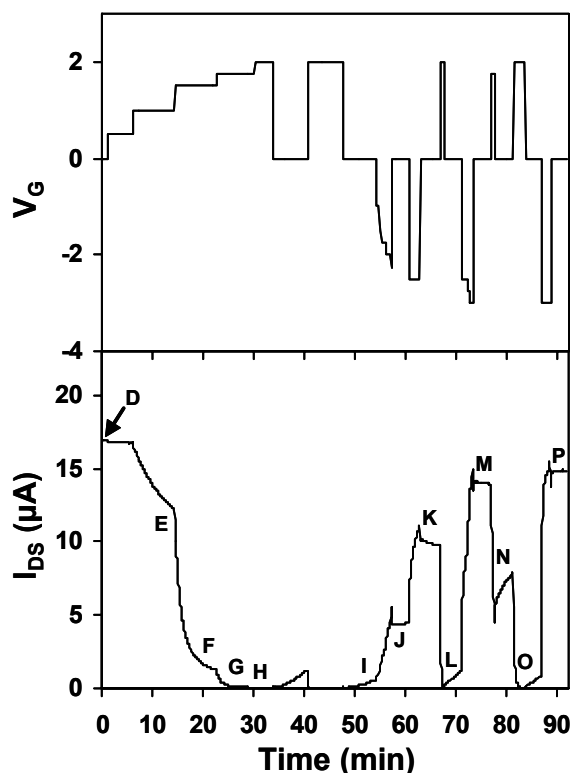

Figure 6-6. Time-dependent performance characteristics of the same device discussed in Figure 4, but tested under humidified N_2 conditions. Labels D through P correspond to the time at which the Raman spectra shown in Figure 5 were obtained.

The effects of induced recovery observed upon application of a negative gate bias are shown for points I through K. As expected, a negative gate bias induces the recovery of the device by re-doping the PEDOT active layer as seen by a decrease in the Raman peak intensities. The data for points L through P reiterate the ability to achieve bistable device operation by switching the device between "on" and "off" states and associating these changes to a change in the PEDOT doping level, as seen in the Raman spectra. All of these effects are consistent with the electrochemical device operation put forth in equations (1) and (2).

126

6.4 Conclusion

A bistable, doped organic TFT has been demonstrated under a controlled N_2 environment. Under humidified conditions, the depletion and recovery of the active layer can be induced with a positive and negative gate bias, respectively. This behavior was explained through electrochemical reactions involving the oxidation and reduction of water. Upon removal of V_G, both I_{DS} and I_G slowly return to their original value due to the reversal of the electrochemical depletion and recovery reactions put forth. Longer applications of the gate bias were required to stabilize the state of the device by allowing the reaction products to diffuse out of the film. Moisture contained in the film was shown to act as the reactant for both oxidation and reduction in addition to acting as a plasticizer to control the mobility and diffusion of other species ($O_2(g)$ and $H_2(g)$) in the film. Raman spectroscopy was utilized to show that the observed switching behavior in these devices is due to a change in the PEDOT doping level.

6.5 References

141. Lu, J.; Pinto, N. J.; MacDiarmid, A. G. *J. Appl. Phys*. **2002**, *92*, 6033.

142. Epstein, A. J.; Park, J. H.; Youngmin, K.; Hsu, F.; Chiou, R.; Waldmann, O.; Prigodin, N. *Polymer Preprints (Am. Chem. Soc., Div. Polym. Chem.)* **2004**, *45*, 149.

143. Nilsson, D.; Kugler, T.; Svensson, P.-O.; Berggren, M. *Sensors and Actuators B* **2002**, *86*, 193.

144. Zhu, Z.-T.; Mabeck, J. T.; Zhu, C.; Cady, N. C.; Batt, C. A.; Malliaras, G. G. *Chem. Commun*. **2004**, 1556.

145. Stricker, J. T.; Gudmundsdöttir, A. G.; Smith, A. P.; Taylor, B. E.; Durstock, M. F. To be submitted to J. Phys. Chem. B.

146. Chen, X.; Inganäs, O. *J. Phys. Chem*. **1996**, *100*, 15202.

147. Zykwinska, A.; Domagala, W.; Pilawa, B.; Lapkowski, M. *Electrochim. Acta* **2005**, *50*, 1625.

148. Epstein, A. J.; Hsu, F. C.; Chiou, N. R.; Prigodin, V. N. *Synth. Met.* **2003**, *137*, 859.

149. Li, Y.; Qian, R. *Synth. Met.* **1993**, 53, 149.

150. Nilsson, D.; Chen, M.; Kugler, T.; Remonen, T.; Armgarth, M.; Berggren, M. *Adv. Mater*. **2002**, *14*, 51.

151. Garreau, S.; Duvail, J. L.; Louarn, G. *Synth. Met.* **2002**, 125, 325.

152. Garreau, S.; Louarn, G.; Lefrant, S.; Buisson, J. P.; Froyer, G. *Synth. Met.* **1999**, 101, 312.

153. (a) Pettersson, L. L. A.; Ghosh, S.; Inganas, O. *Organic Electronics* **2002**, *3*, 143. (b) Jönsson, S. K. M.; Birgerson, J.; Crispin, X.; Greczynski, G.; Osikowicz, W.; Denier van der Gon, A. W.; Salaneck, W. R.; Fahlman, M. *Synth. Met*. **2003**, *139*, 1. (c) Ouyang, J.; Xu, Q.; Chu, C.-W.; Yang, Y.; Li, G.; Shinar, J. *Polymer* **2004**, *45*, 8443.

Chapter 7

Organic Thin Film Transistor with a

Layer-by-Layer Assembled Active Layer

7.1 Introductory Remarks

The continuous development of deposition techniques for polymeric materials enhances the capability to design unique electronic device architectures at a low cost. In conjunction with this process is the improved understanding of the role that these macromolecules can have in the operation of electroactive devices. Until now, the work herein has entailed the utilization of layer-by-layer (LbL) assembly of polyelectrolyte multilayers for insulating purposes. The LbL assembly technique has also been used for the deposition of multilayer films with an intrinsically conducting component, such as polypyrrole[154] and derivatives of polythiophene[155,156]. As the conductivity spectrum for these multilayer films broadens, so will their application in electroactive devices (i.e. thin film transistors and photovoltaics). A complimentary objective to this broadening is the development of the structure-property relationships. Determining the electronic properties of the polyelectrolyte multilayers with known polymer configurations in the bulk, and at interfaces, will play a significant role in understanding how nanoscale architecture affects device performance.

A device architecture with crosslinked PAH/PAA multilayers as the gate dielectric material and an aluminum gate electrode were used to study the application of LbL assembled active layers in thin film transistors (TFTs). The active layer for these devices consisted of the same doped conducting polymer, poly(3,4-ethylenedioxythiophene:poly(styrenesulfonate) (PEDOT:PSS), as was used in Chapters 5 and 6, but as a polyanion for the layer-by-layer

deposition with poly(allylamine hydrochloride) (PAH). The linear growth in film thickness and the conductivity of PAH/PEDOT:PSS multilayers were characterized as the number of bilayers was increased. TFTs were then fabricated with PAH/PEDOT:PSS multilayer films serving as the active layer and then tested for depletion of its conductivity. After testing these devices under different environments, the conductive properties of PEDOT in both the spincoated and multilayer films were compared.

7.2 Experimental

Aqueous stock solutions of PEDOT:PSS, under the trade name of Baytron[®] P with a reported concentration range of $1 - 5\%$, were purchased from H.C. Stark Inc. and filtered with 1 µm pore size filters prior to use. The spincoated films were spun at 500 rpm for 10 s and then 3000 rpm for 30 s. The LbL deposited conducting multilayer films were fabricated using an anionic solution that consisted of ~ 1 % Baytron[®] P and ~ 0.01 M NaCl, and a cationic solution that consisted of 5 mM poly(allylamine hydrochloride). The polymers used for the LbL assembled gate dielectric layer, poly(acrylic acid) (M_w = 90,000) and poly(allylamine hydrochloride) (M_w = 60,000) were purchased from Polysciences, Inc. Polyelectrolyte solutions were pH adjusted with NaOH and HCl using an Orion model 230A pH meter. Each monolayer deposition cycle (~ 15 min) was followed with multiple rinse steps in deionized H_2O (18 MΩ·cm) in a Carl Zeiss Microm DS-50 automatic slide stainer. Silver and aluminum electrodes were thermally evaporated at a rate of 3 and $4 - 5$ Å/s, respectively, in an Explorer 18 Denton Vacuum system (< 10^{-7} Torr) using a Telemark model 860 deposition controller. The aluminum gate electrode was deposited to a thickness of $350 - 400$ Å. The active layer channels for the TFTs were patterned with dimensions of approximately 6 mm wide by 3 mm long by using

Kapton tape with silicon adhesive. Film thicknesses were measured with a Tencor P-10 surface profiler at a stylus force of 0.6 mg. The absorbance spectra were obtained using a Varian Cary 5000 UV-Vis-NIR spectrophotometer. Resistivity measurements were obtained using the van der Pauw technique with a Kiethley 4200 semiconductor characterization system. The TFT device performance was characterized with two Keithley 2400 SourceMeters.[®] Gases (air or N_2) were bubbled through deionized water (18 MΩ·cm) to create humidified conditions (relative humidity (RH) ~ 75%) or purged through Drierite[®] to create dry conditions.

7.3 Results and Discussion

7.3.1 Layer-by-Layer Deposition of PAH/PEDOT:PSS Multilayers

The utilization of PEDOT/PSS in polyelectrolyte multilayer films was investigated to develop a conductive LbL assembled active layer that could be used for doped organic TFT devices. To form these multilayers, a glass substrate was dipped in an alternating sequence between dilute aqueous solutions of PEDOT:PSS and PAH. The films were deposited at a pH of 3.5, which resulted in an average bilayer thickness of ~ 17 Å. A linear growth in film thickness with an increase in the number of PAH/PEDOT:PSS bilayers is shown in Figure 7-1b. The growth of the multilayer films was a result of electrostatic interactions between the PSS polyanion and the PAH polycation. Additionally, the amount of PEDOT deposited onto the substrate was also observed to increase in a consistent manner with the number of bilayers. This effect was apparent with the changes observed in the UV-Vis absorbance spectra shown in Figure 7-1a as the number of bilayers was increased. With an increase in film thickness, a higher intensity was observed for the broad absorbance peaks present at 965 nm and beyond 1300 nm, which are representative of the subgap states for the polaron and bipolaron charge carriers in

PEDOT.[157] The absorbance values at λ = 2900 nm in Figure 7-1b appeared to increase linearly with the number of bilayers. Therefore, PSS acts as both a counterion for the doped state of PEDOT and the polyanion component for LbL deposition of conducting multilayered films. Additional information about the deposition characteristics of these multilayer films using different grades of PEDOT:PSS has been reported by Smith *et. al.*[158] In addition, similar multilayered films have previously been fabricated with PEDOT/PSS, but with the use of a different polycation that resulted in a thicker bilayer (~50 Å) which required sonication to obtain smooth films.[156]
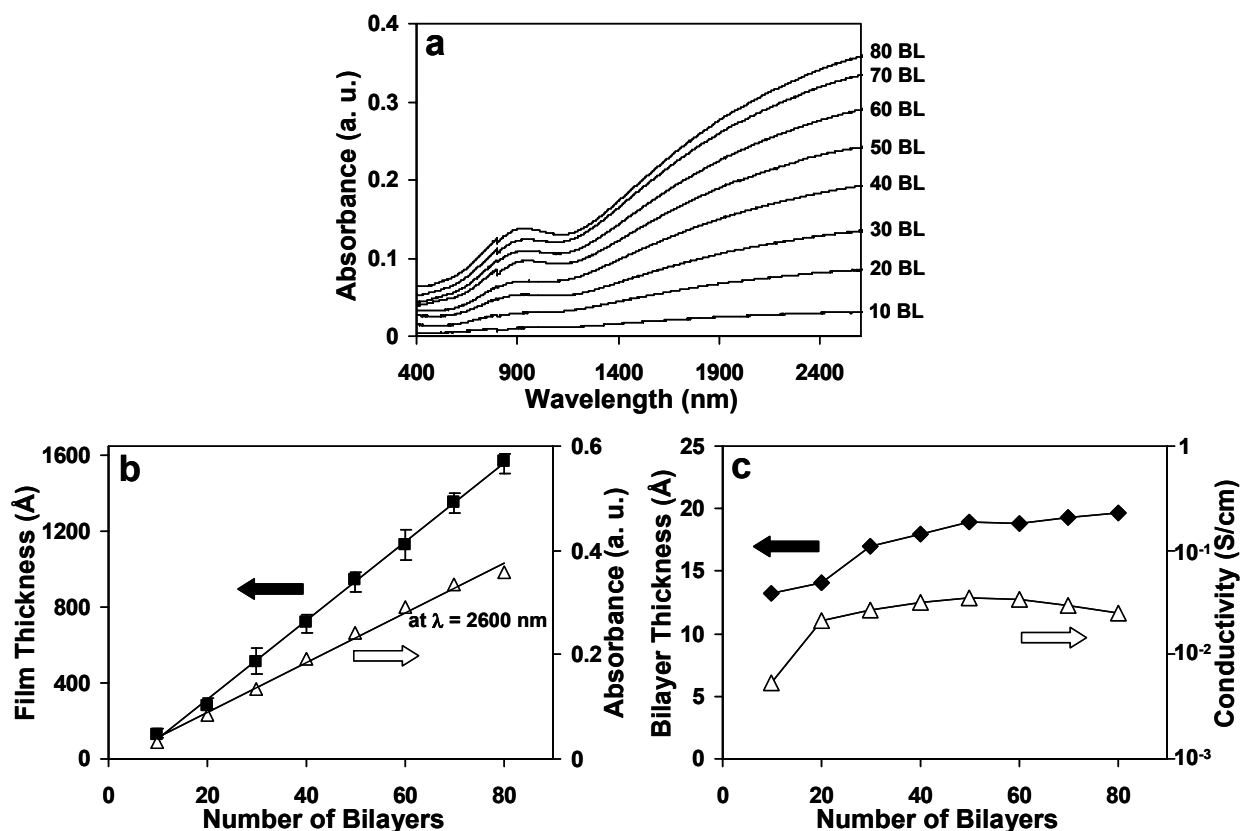

Figure 7-1. a) Visible-near infrared absorbance spectra obtained from PAH/PEDOT:PSS multilayer films with a number of bilayers (BL) ranging from 10 to 80. b) The film thickness and absorbance of the multilayer films in (a) as a function of the number of bilayers. c) Billayer thickness and conductivity as a function of the number of bilayers

The conductive characteristics of PAH/PEDOT:PSS multilayer films were investigated to gain a better understanding of how the multilayer structure effected the electronic properties of PEDOT. The conductivities of the multilayer films discussed in Figure 7-1a were measured to determine if there was a dependence on film thickness. As shown in Figure 7-1c, the conductivity of multilayer films with 10 bilayers was ~ 5 x 10^{-3} S/cm. The conductivity then increased an order of magnitude at 20 bilayers where it then remained similar as the number of bilayers increased. The increasing trend of the conductivity with the first 10 bilayers was recently verified and attributed to the build-up characteristics of LbL assembled films.[158] As charge overcompensation within the multilayer film becomes stabilized after depositing 20 bilayers,[159] changes in the multilayer structure may result in modifications to the charge percolation path between PEDOT particles.

Slight differences were also observed between the conductive characteristics of LbL deposited PAH/PEDOT:PSS multilayer films and those for spincoated PEDOT/PSS films. The conductivity of the multilayer films was slightly less than half than that measured for the spincoated films (thickness ~ 550 Å). The lower level of conductivity for these multilayer films was attributed to the PAH content and the partial decomplexation of PEDOT from PSS that has been demonstrated with UV-Vis-NIR techniques when deposited in this state.[158]

The other noticeable difference between LbL deposited PAH/PEDOT:PSS multilayers and spincoated films was their change in conductivity when exposed to ethylene glycol (EG). Solvents with two or more polar groups are commonly used to increase the conductivity of PEDOT:PSS and is referred to as a "secondary doping" effect.[160] The solvent is believed to cause a partial decomplexation of PEDOT from PSS, which allows it to adopt a quinoid bond configuration.[161] As the spincoated films of PEDOT:PSS were exposed to EG, the conductivity

increased by three orders of magnitude (30 - 70 S cm^{-1}). When the LbL deposited PAH/PEDOT:PSS multilayer films were exposed to EG, the conductivity decreased from 3.5 x 10^{-2} S cm^{-1} to 2.4 x 10^{-2} S cm^{-1}. The spincoated PEDOT:PSS films were also crosslinked with a multivalent cation by submerging the film into a 0.25 M CaCl$_2$ solution. Multivalent ions are commonly used to crosslink the PSS component in these films as a means to help maintain their physical integrity in aqueous solutions.[162] As these films were exposed to EG, the conductivity (~ 1 x 10^{-2} S cm^{-1}) gradually increased to ~ 2.2 S cm^{-1} within 24 hours.

These results suggested only PEDOT oligomers that are tightly bound to PSS in solution get incorporated into the multilayer films and that this association cannot be disrupted by solvents commonly used for "secondary doping." The conductivity of these films decreased slightly when exposed to EG probably because PEDOT was bound to the PSS, which most likely swelled in the presence of the solvent and trace amounts of moisture. Whereas, an additional amount of PEDOT gets incorporated into spincoated that may not have as strong of an interaction with PSS. Therefore, this added amount of PEDOT can adopt a modified bond configuration that is independent of the changes in PSS when exposed to different environments. Also, the increase in conductivity with the exposure of ionically crosslinked spincoated films to EG may have been less due to a more inhibited change of PSS or the removal of some PEDOT when submerged in the CaCl$_2$ solution.

7.3.2 OTFT with a PAH/PEDOT:PSS Multilayer Film as the Active Layer

The LbL deposited PAH/PEDOT:PSS multilayers and spincoated PEDOT:PSS films were utilized as an active layer material for TFTs using the device architecture described in Chapters 5 and 6. These devices were tested under different environments to provide a comparison to the

performance of devices fabricated with PEDOT:PSS active layers treated with EG. The performance characteristics of a device with 40 crosslinked PAH/PAA bilayers as the dielectric layer (deposited onto an aluminum gate electrode) and 80 PAH/PEDOT:PSS bilayers as the active layer are shown in Figure 7-2. Initially, a source-drain voltage (V_{DS}) of 0.5 V was applied to the device under ambient conditions and then exposed to a dry N_2 environment immediately. As shown in Figure 7-2b, the source-drain current (I_{DS}) through the multilayer active layer increased when exposed to dry N_2, whereas the exposure of a secondary doped active layer to a dry environment typically resulted in a small decrease. I_{DS} did not appear to decrease and a high leakage current (I_G) was observed when a gate bias of $V_G = 2$ V was applied under a dry environment. Similar effects were described in Chapter 6 for a device with a secondary doped active layer. When the device with the multilayer active layer was exposed to humidified N_2 at time = 18 min, the I_{DS} decreased to a lower level than was observed under ambient conditions. This trend is also in direct contrast to the increase in I_{DS} typically observed when devices with a secondary doped active layer were exposed to a humid environment. As shown in Figure 7-2, when V_G was increased under humidified N_2 conditions, a decrease in I_{DS} was observed. Additionally, I_G was lower with the application of a gate bias under humidified N_2 than was observed under a dry environment. After the application of $V_G = 2.5$ V for over 20 min, the device remained in the "off" state until a recovery of I_{DS} was initiated by exposing the device to humidified air. Although I_{DS} increased significantly when exposed to dry N_2, it stabilized after a few minutes and then continued to increase when exposed to dry air. Finally, a decrease in I_{DS} was observed when the device was exposed to EG. This decrease was attributed to the presence of water, which could not be separated from EG.
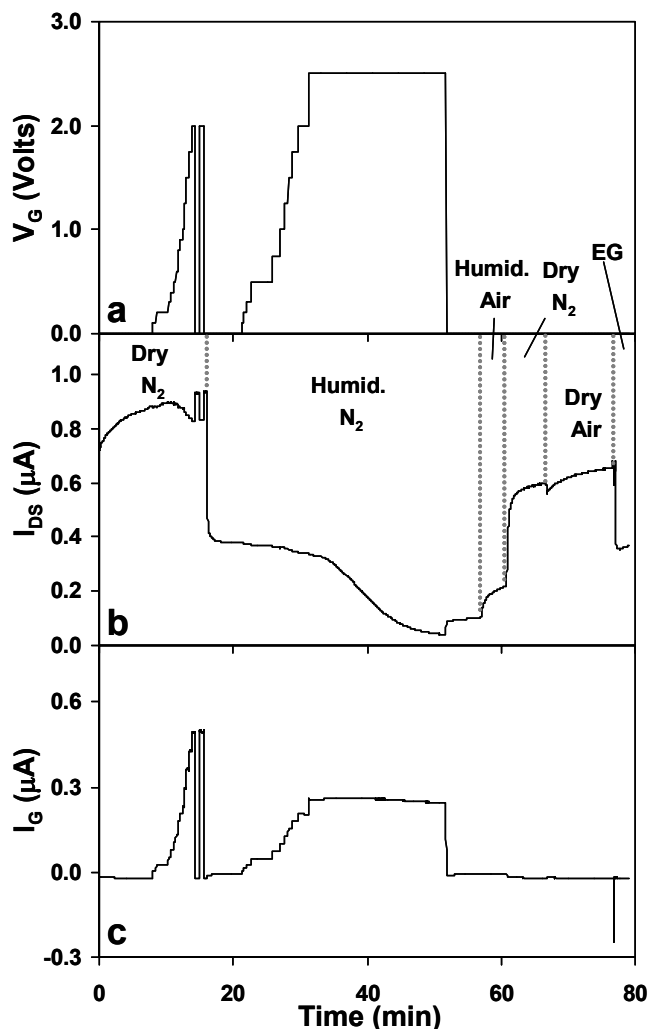
Figure 7-2. Performance characteristics of a TFT with 60 crosslinked PAH:PAA bilayers (deposited at a pH of 6.0 and heat treated at 260 °C) as the dielectric layer and 80 PAH/PEDOT:PSS bilayers as the active layer (thickness = 1770 Å). a) Applied gate voltage as a function of time. b) Measurement of source-drain current as a function of time with the change in environmental conditions indicated therein. c) Measurement of leakage current as a function of time.

Similar observations were made using a spincoated PEDOT:PSS active layer that was not treated with EG. The only significant difference observed between the devices with a spincoated PEDOT:PSS active layer and those with a LbL deposited active layer was that the former could be treated with EG to perform as if it had initially been deposited with EG. The similarities between the devices in how I_{DS} changed with humidity and how it changed when exposed to EG supports the thought that "secondary doping" decreases the interaction between PEDOT and PSS

136

in spincoated films, but has no effect on the stronger interaction between these components in LBL deposited films.

7.4 Conclusion

The LbL deposition of a conductive film was demonstrated using PAH and PEDOT:PSS, This technique was used to deposit a multilayer film as an active layer for a TFT. As the number of bilayers was increased, a linear increase in film thickness was observed and the content of PEDOT was shown to be constant using UV-Vis-NIR techniques. After the deposition of 20 bilayers, the bulk film conductivity was obtained, which was lower than the spincoated films due to the PAH content and the partial decomplexation of PEDOT from PSS. The inability to increase the conductivity of PAH/PEDOT:PSS multilayers with EG, as is known to occur for spincoated PEDOT:PSS films, suggested only PEDOT with a strong interaction with PSS in solution was incorporated using the LbL technique. The device performance when using these materials as the active layer supported the depletion mechanism involving the electrolysis of water, but the response of I_{DS} to a change in humidity was different. Devices with LbL deposited PAH/PEDOT:PSS multilayers and spincoated films as the active layer had a similar response to a change in humidity, but the response of the spincoated active layers could be reversed (i.e. response of I_{DS} with a change in humidity) when exposed to ethylene glycol.

7.5 References

154. Fou, A. C.; Rubner, M. F. *Macromolecules* **1995**, *28*, 7115.

155. Cutler, C. A.; Bouguettaya, M. Reynolds, J. R. *Adv. Mater.* **2002**, *14*, 684.

156. Wakizaka, D.; Fushimi, T.; Ohkita, H.; Ito, S. *Polymer* **2004**, *45*, 8561.

157. (a) Gustafsson, J. C.; Liedberg, B.; Inganäs, O. *Solid State Ionics* **1994**, *69*, 145. (b) Patil, A. O.; Heeger, A. J.; Wudl, F. *Chem. Rev.* **1988**, *88*, 183.

158. Rachel R. Smith, R. R.; Smith, A. P.; Stricker, J. T.; Taylor, B. E.; Durstock, M. F. *Macromolecules* accepted for publication.

159. Kurth, D. G.; Volmer, D.; Klitzing, R. V. in *Multilayer Thin Films*; Decher, G.; Schlenoff, J. B., Eds.; WILEY-VCH Verlag GmbH & Co.; Weinheim, 2003, Ch. 14.

160. Petterson, L. A. A.; Ghosh, S.; Inganäs, O. *Organic Electronics* **2002**, *3*, 143.

161. Ouyang, J.; Xu, Q.; Chu, C.-H.; Yang, Y.; Li, G.; Shinar, J. *Polymer* **2004**, *45*, 8443.

162. Ghosh, S.; Inganäs, O. *Synth. Met.* **1999**, *101*, 413 and references therein.
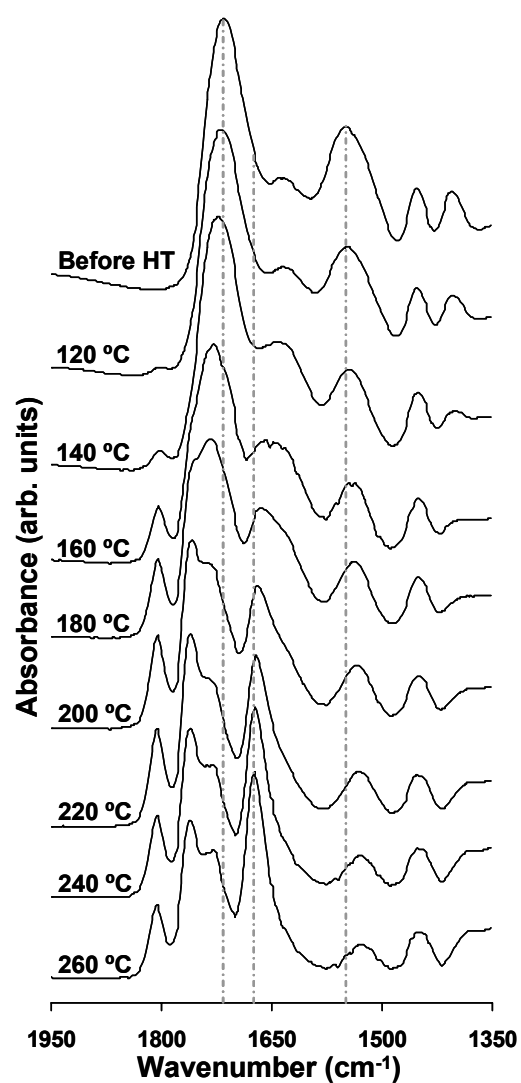
Appendix A

Figure A-1. The reflective FT-IR absorbance spectra obtained from the PAH/PAA multilayers (deposited at a pH of 2.1) before heat treatment (HT) and each time after heating them with an incremental increase in temperature.
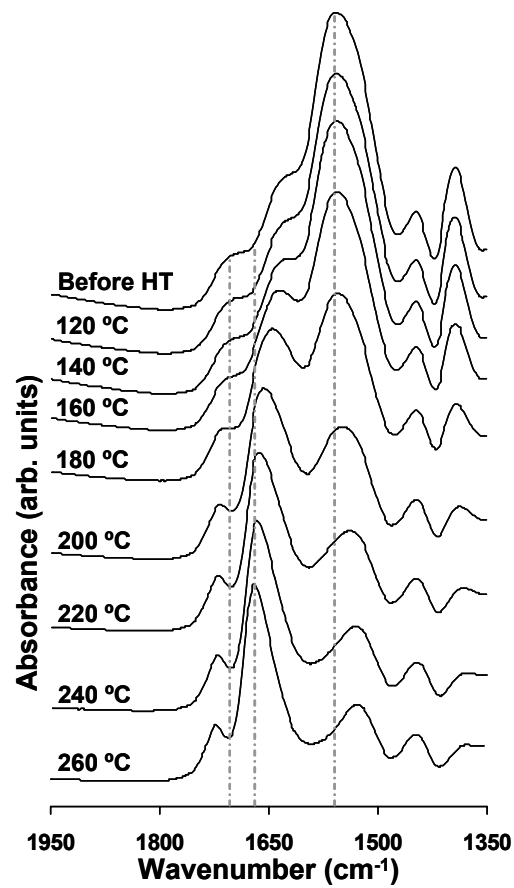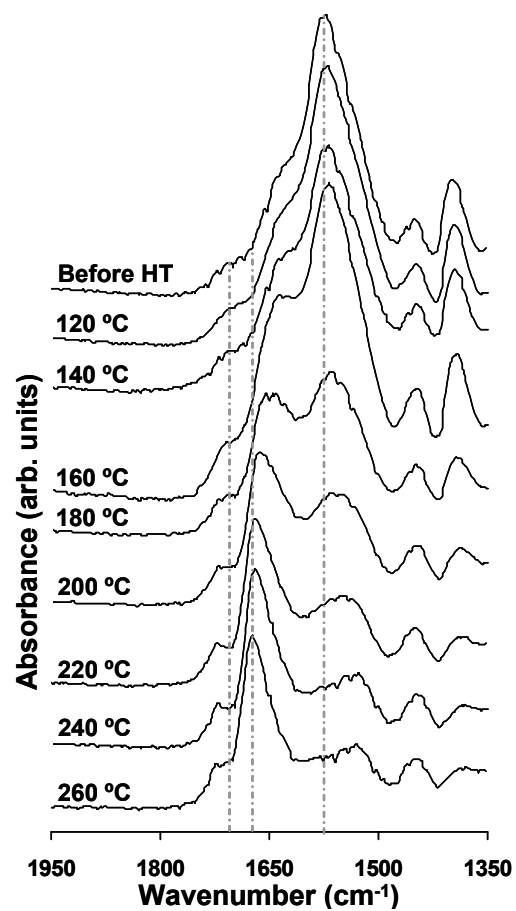
Figure A-2. The reflective FT-IR absorbance spectra obtained from the PAH/PAA multilayers (deposited at a pH of 5.0) before heat treatment (HT) and each time after heating them with an incremental increase in temperature.

Figure A-3. The reflective FT-IR absorbance spectra obtained from the PAH/PAA multilayers (deposited at a pH of 6.0) before heat treatment (HT) and each time after heating them with an incremental increase in temperature.
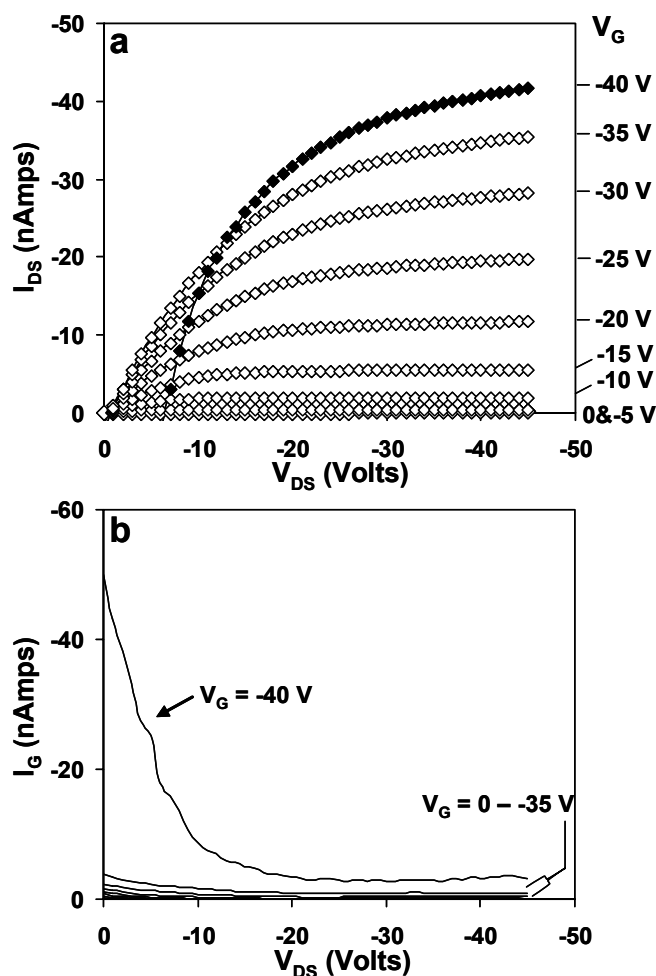
Figure B-1. a) Output characteristics ($I_{DS} - V_{DS}$) of an OFET with P3HT as the active layer and 20 PAH/PAA bilayers (deposited at a pH of 3.5) as the dielectric layer. b) Leakage currents for the tests in (a) as a function of the applied voltage between the source and drain electrodes.
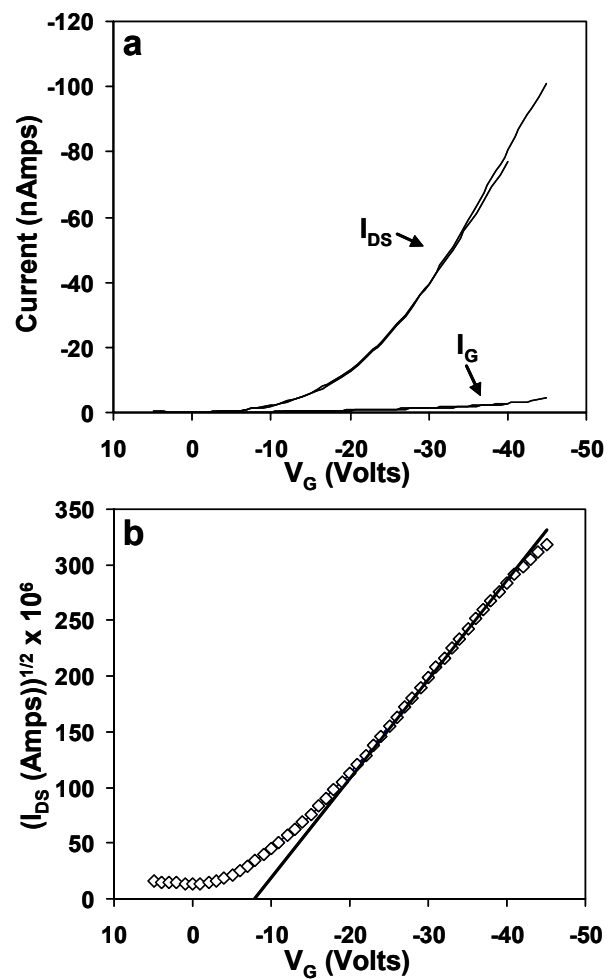
Figure B-2. The transfer characteristics in the saturated regime ($V_{DS} = -5.5$ V) for a device with P3HT as the active layer and 20 PAH/PAA bilayers (deposited at a pH of 3.5) as the dielectric layer. a) The drain and leakage current as a function of voltage applied between the gate and source electrode. b) The $I_{DS}^{1/2} - V_G$ characteristics for the results in (a).
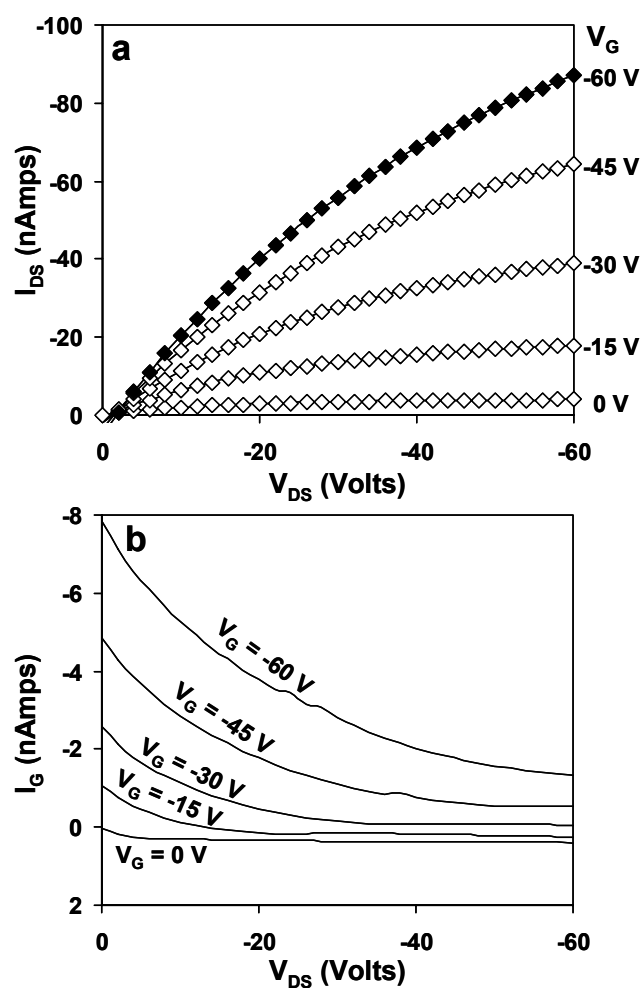
Figure B-3. a) Output characteristics (I_{DS} – V_{DS}) of an OFET with P3HT as the active layer and 40 PAH/PAA bilayers (deposited at a pH of 3.5) as the dielectric layer. b) Leakage currents for the tests in (a) as a function of the applied voltage between the source and drain electrodes.
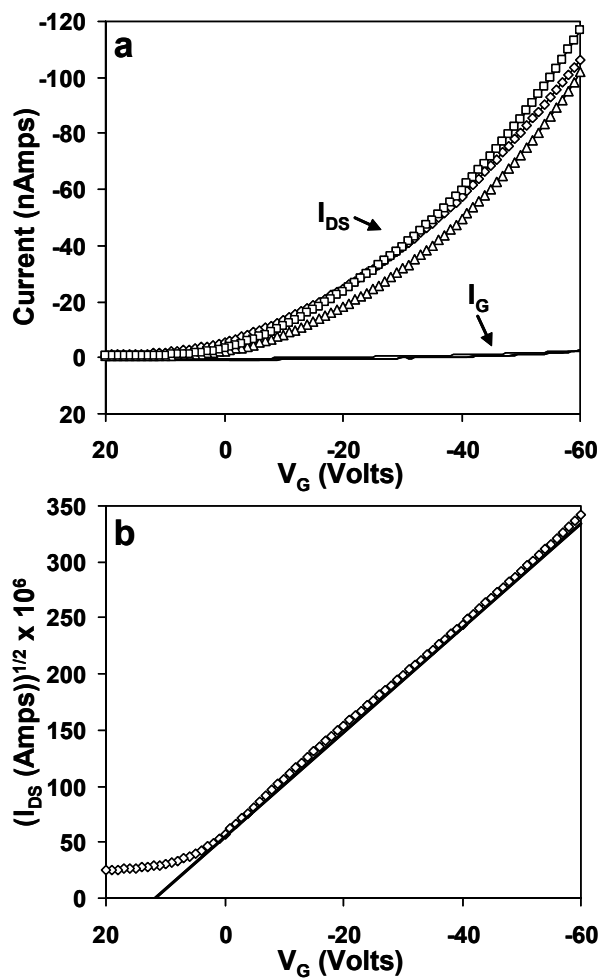
Figure B-4. The transfer characteristics in the saturated regime (V_{DS} = -5.5 V) for a device with P3HT as the active layer and 40 PAH/PAA bilayers (deposited at a pH of 3.5) as the dielectric layer. a) The drain and leakage current as a function of voltage applied between the gate and source electrode. b) The $I_{DS}^{1/2}$ – V_G characteristics for the results in (a).
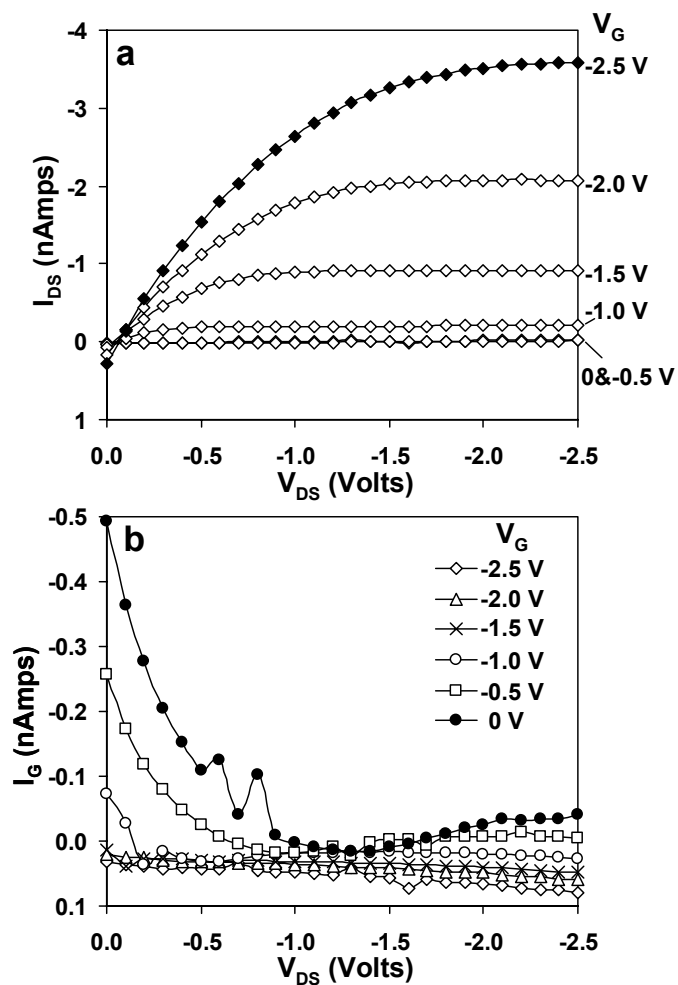
Figure B-5. a) Output characteristics (I_{DS} – V_{DS}) of an OFET with P3HT as the active layer and 40 PAH/PAA bilayers (deposited at a pH of 6.0) as the dielectric layer. b) Leakage currents for the tests in (a) as a function of the applied voltage between the source and drain electrodes.
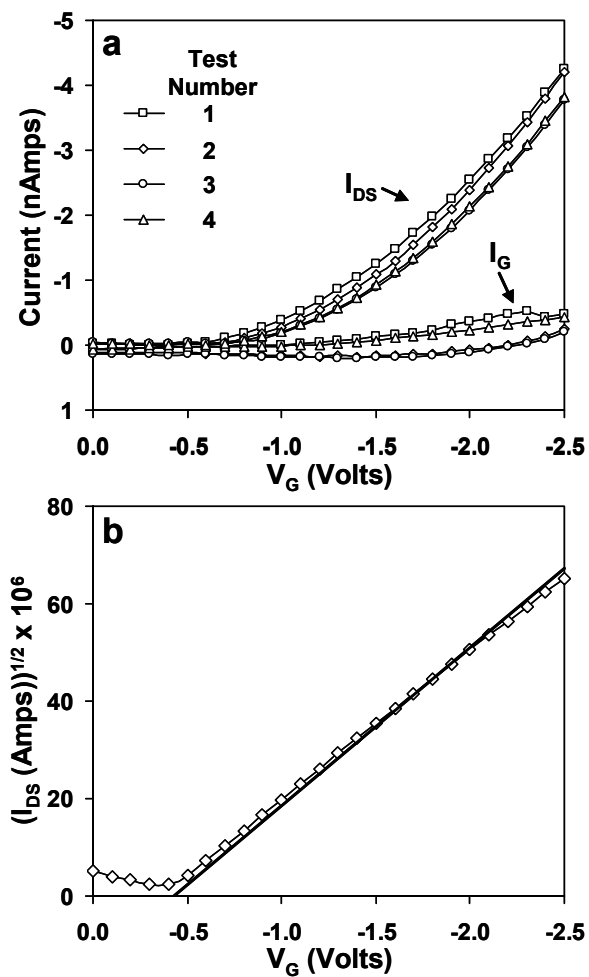
Figure B-6. The transfer characteristics in the saturated regime (V_{DS} = -5.5 V) for a device with P3HT as the active layer and 40 PAH/PAA bilayers (deposited at a pH of 6.0) as the dielectric layer. a) The drain and leakage current as a function of voltage applied between the gate and source electrode. b) The $I_{DS}^{1/2}$ – V_G characteristics for the results in (a).